Influence of Copper (Cu) and Tungsten (W) additions on the passivity and breakdown of Super Duplex Stainless Steels in chloride-containing environments

By Joshua Agbeseyi

Submitted to Swansea University, in fulfilment of the requirements for the degree of Master of Science by Research (MSc)

Swansea University – Bay Campus

M2A

Langley Alloys Ltd.

Submitted April 2022

Declarations

This work has not previously been accepted in substance for any degree and is not being concurrently submitted in candidature for any degree.

[redacted]

This thesis is the result of my own investigations, except where otherwise stated. Other sources are acknowledged by footnotes giving explicit references. A bibliography is appended.

[redacted]

I hereby give consent for my thesis, if accepted, to be available for photocopying and for inter-library loan, and for the title and summary to be made available to outside organisations.

[redacted]

The University's ethical procedures have been followed and, where appropriate, that ethical approval has been granted.

[redacted]

Acknowledgments

I would like to first and foremostly thank my family; mum, dad and brother included, for their ongoing and endless moral support and motivation in completing my degree of study.

Special thanks also to my primary and secondary supervisors, Prof. G. Williams and Dr. N. Wint, as well as lab technician Dr. C. Richards for all their academic, pastoral and technical guidance offered in completion of this thesis.

I extend appreciation to the M2A for making such practically driven research postgraduate courses available for undertaking, as well as the cohort of postgraduate students providing a supportive network in the field of academic research

Lastly, I also extend gratitude to Langley Alloys for collaborative sponsorship of the project.

Table of Contents

1. Abstract Summary

This thesis has been produced as a result of academic (Swansea University) and Industrial (Langley Alloys Ltd.) collaboration, facilitated through Swansea University's M2A organisation under the Masters by Research (MSc) scheme of study.

The scope of this investigation was set in the hopes of contributing to the current collective understanding and literature surrounding the localised electrochemical breakdown activity in Super Duplex Stainless Steels (SDSS). With specific consideration being given to highlighting the influence of Copper and Tungsten alloying additions on SDSS's observed passivation and breakdown tendencies, when immersed and anodically polarised in a range of acidic & alkaline chloride media. This would, ideally, give an idea into how said additions impact and dictate the consequential states of nobility in the dual-phasic microstructure and bulk-alloy.

In pursuit of these aims, it was the scope of this study to electrochemically investigate 3 different high Cr-content (25wt%) SDSS alloys of identical composition (excluding Cu- and W wt%) in various chloride-containing aqueous media. Consequently this would help ascertain their strengths/weaknesses in given conditions, with specific consideration to their addition-differences which would then be attributed to observed differences corrosion features with specific element additions.

The alloys investigated in this study were UNS-S3550 (Ferralium® 255) UNS-S3750 (SAF 2507) and UNS-S3760 (Zeron®100). Under external anodic-polarisation these alloys were tested in various deoxygenated electrolyte solutions of 0.6M $NaCl_{(aq)}$ at a maintained ambient temperature of 25°C, in both alkaline and acidic conditions ranging from pH 3 to 11. Adjustment of pH was achieved via drop-wise addition of NaOH and HCl. PP and SVET analysis was employed to help quantify, map and explain the bulk & localised ionic-transport behaviour (respectively), both under open-circuit and non-polarised conditions.

Findings from bulk anodic current characterisation using potentiodynamic polarisation were in good agreeance with observations made in a previous iteration of this study. That is to say it was found that in these conditions, anodic current increases typically associated with the phenomena of passive layer (PL) breakdown were mainly a result of transpassive dissolution kinetics, spotted with instances of localised pitting. Post-corrosion microscopy showed the anodic dissolution to unfold as a surface-wide, selective etching of constituent phases, typically attacking the less noble ferrite phase. This was later further supplemented with localised in-situ SVET scanning, showing the corrosive damage to evolve as an anodic “front”, steadily progressing across the active region of the corroding surface until stoppage of polarisation. Hysteresis loop data from potentiodynamic polarisation (PP) sweeps demonstrated a clear benefit of Cu-additions in mitigation of pitting damage in both acidic and alkaline chloride media. W-additions were also found to be beneficial for suppression of corrosion damage when compared to non-Cu/W containing grades (UNS-S3750).

2. Introduction: Corrosion of Super Duplex Stainless Steels

2.1. Historical Context – Duplex Stainless Steels

Duplex stainless steels (DSS) are defined microstructurally by their highly-dual phasic ferrite/austenite structure. DSSs are well known to possess highly desirable mechanical & electrochemical properties, particularly in the case of the even more specialised Super Duplex Stainless Steel (SDSS) grades, distinguished largely by its exceptional pitting corrosion properties (PREn ≥ 40).

The proportionally-equal, ferritic & austenitic dual phase microstructure was first referenced by Bain and Griffith in a 1927 study on ferritic/austenitic structures in Fe-Cr-Ni systems [1]. Subsequent to release of this study, DSS alloys were first commercially established in 1930, being well known for their greater castability and corrosion resistance at elevated temperatures. As such, in the early stages of their development DSSs were commonplace in creation of castings, valves, plates and forging across multiple industries[2]. Metallurgists continued to develop the alloys over the following years both compositionally (N, Mo, Ni-additions) and processing/treatments-wise, thereby, elevating its competitive position with the already-established and comparably strong austenitic grades (at the time of discovery). The addition of nitrogen for assistance in control of ductility for casting and weldability is a notable example of such developments. Early on in DSS history, a less-intentional development in the form of a melting error at the J. Holtzer Company (France) in 1933, lead to the production of a DSS grade (20%-Cr, 8%-Ni, 2.5%-Mo)[3] - much less sensitive to intergranular corrosion (IGC) in a number of corrosive media. This became a distinguishing feature for DSSs compared to austenitic grades, as their carbon-rich nature was known to often lead to formation of continuous Cr-carbide networks, ending in rapid corrosion via numerous Cr-depleted zones. This disadvantage of austenitic stainless steels in addition to the superior strength properties of DSSs lead to an increase in patent entries at the time, including a later issuing involving larger copper additions to assist in particularly aggressive media.

Nickel shortages became more pronounced during war times (1940s/50s) and as such, research and investment into comparatively low-nickel DSS grades was elevated[4]. Soon-after, the advantage of ferrite-austenite balanced structures over austenitic grades in chloride stress corrosion cracking (SCC) became more established and clear.

The years following saw a number of processing-related improvements, including the widely marketed and used French UR50 grade[5]. Produced using precisely-weighed alloying additions in a high-frequency induction furnace; under partial vacuum to ensure carbon removal, deoxidation and impede nitrogen ingress. Then came cast-alloy CD4-MCu (UNS J93370) in the late 1950s; initially known for its relatively poor toughness and ductility, but then was improved via reduction of Cr-content (to 22-23%) and introduction of quench-annealing treatment to enhance ductility. Subsequent to this DSSs saw a dormant period of popularity and development due to notoriety brought about by difficulty with manufacturing and fabrication (crack sensitivity).

In the late 1960s/ early-70s came the significant development of the implementation of the vacuum & argon decarburisation (VOD/AOD) methods (Gunnarson, 1963). Consequentially allowing for greater control of N- and Cr-% as well as the reduction of carbon/sulphur/oxygen content in steels and thus, restricting presence of deleterious carbides[6], [7]. UNS-S31500 was a notable example of said improvement, known for its enhanced resistance to SCC. This was owed to a more controlled compositional make-up allowing for optimised ferrite/austenite phase proportions, as well as a carbon content of no more than 0.03%. Such development in process methodology, coupled with the growing economic requirements from; (1) inflation of austenitic-grade prices from further nickel shortages[8] and (2) increased demand from booming off-shore oil industries needing more inert SSs, was hugely beneficial to further establishment of DSSs at this time. AOD/VOD processing methods are still used in SS production to this day, with all three SDSS alloys used in this study being produced using this method also. Importance of maximising Nitrogen content within specification limits largely became recognised in the 1970s, ushering another boom in development of DSSs with new-found establishment of production and welding metallurgy. This lead to development of highly-alloyed, large Cr-content grades, including one of the first "Super" DSS grades known as Ferralium 255 (UNS-S32550). A grade known for its excellent resistance to pitting corrosion, used in offshore industries for sulphuric-acid containing environments and as castings in products such as pumps and valves. SDSSs are a grade of stainless steel containing a minimum of 25wt% Chromium and possessing a dual-phase, equally-proportionate microstructure consisted of Austenite - γ (FCC) and alpha-Ferrite -α (BCC).

Improvement of the new-found Super Duplex SS grades continued into the 1980s, where greater specificity in proportion of alloying elements, as well as the implementation of tungsten as an addition, continued to provide greatly improved mechanical properties and thermal stability. This was however, at cost of greater overall propensity to precipitating deleterious phases, although correct processing & temperature control matched with correct solution annealing practices will typically mitigate this. Driven by the aim of reducing raw material costs in the mid-1980s, the Lean Duplex SS (LDSS) grade was developed with significantly lower nickel content, leading to more affordable costs of production, albeit with diminished pitting corrosion resistance[5]. The 80s concurrently saw the introduction of the even more pitting-resistant grade of Hyper Duplex SS (HDSS), possessing a PREn of up to 50. Despite this HDSS grades were not as largely circulated due to the scarce range of applications in requirement of such properties.

2.2. Mechanical Properties of Super-Duplex Stainless Steels (SDSS)

SDSSs possess superior corrosion resistance to standard stainless steels and even duplex stainless steels; particularly in environments with high propensity for localised pitting corrosion and stress corrosion cracking [9]. To achieve this duplex (dual-phase) microstructure, the correct proportions of austenite- and ferrite-stabilising elements must be added (i.e. Cr, Cu, Mo, N, Mn, Ni) alongside a carefully controlled cooling process [10]. This microstructure develops at a temp range of around 1000-1200°C; as the newly solidified ferritic mixture begins to precipitate austenite islands (ref. Fe-Cr-Ni equilibrium diagram in fig. 1 [11]).

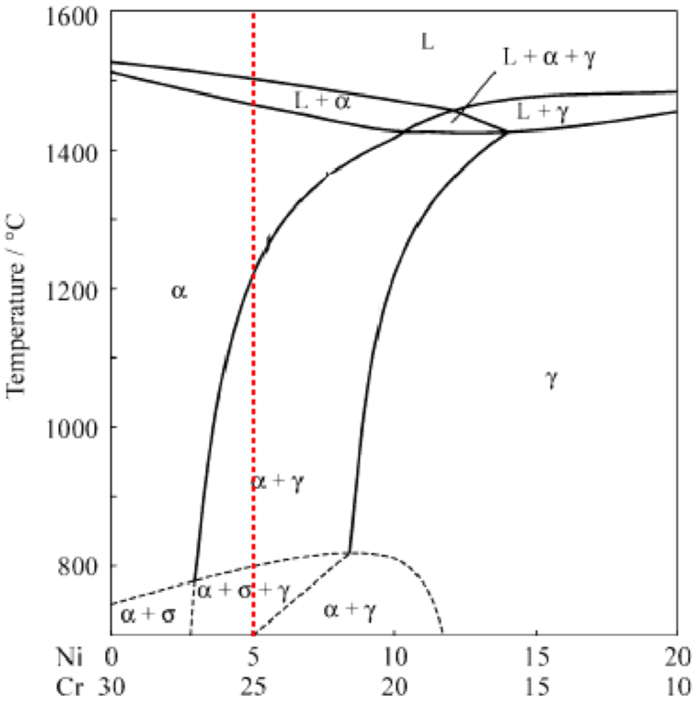

Figure 1: Fe-Cr-Ni system phase diagram (70% Fe). Red-dotted line shows microstructural development of SDSS grades. Adapted from previous study[11]

DSSs possess superior mechanical and corrosion properties in comparison with austenitic grades of SS in temperatures ranging from -50 to 250°C [10]. Outside of this range however, the susceptibility of the ferrite phase to embrittlement renders DSSs inferior to austenitic grades, specifically with regard to toughness and strength. The favourable mechanical properties of DSSs can be largely attributed to the morphology and distribution of their constituent phases. Tensile strength can be linked mostly to the strong yet brittle α-phase, which is typically observed to possess a slightly higher modulus of elasticity in comparison to austenite[12] at the expense of ductility. Tao et al found that when subjecting solution-annealed and quenched 2205 DSS to nanoindentation tests, ferrite exhibits a marginally higher elastic modulus (206.94GPa vs 199.84GPa), as well as lower nano-hardness (3.95GPa vs 4.1GPa) compared to Austenite. This being said, it was also found that ferrite possessed a lower yield strength and work-hardening exponent[12]. Generally speaking, the enhanced mechanical properties of DSSs compared to other grades are largely a result of finer grain sizes within the microstructure. This gives DSS alloys superior yield strength (Hall-Petch relationship) as well as improved toughness [10]. When quenched and annealed correctly, the strength of DSS is comparable to that of austenitic and ferritic grades; $\sigma\text{-}y_s$ (yield strength) is 2-3 times larger than in austenitic grades. Strength properties of SDSSs are further enhanced by the solid solution strengthening from substitutional constituent elements of chromium and molybdenum, as well as the interstitial element of nitrogen. Furthermore, chromium and molybdenum also act as ferrite stabilisers while nitrogen acts to stabilise austenite - due to its higher solubility within the phase [10]. This infers that additions of each alloying element further improve the respective strength and toughness/ductility properties of ferrite and austenite phases within the alloy.

Toughness of DSSs is dominated mainly by the γ-phase. This is generally understood to be as a result of γ's ability to impede the progression of cleavage fracture through the α-phase. DSSs also exhibit strong anisotropy of mechanical properties, particularly when cold-rolled, due to the resultant characteristically textured microstructures. For example, Hutchinson et al found a cold-rolled alloy with the composition of 22wt% Cr + 5wt% Ni + 3wt% Mo exhibited higher impact & fracture toughness performance in the transverse direction as opposed to the longitudinal, relative to its banded structure. This was as a result of its crystallographic texture, being: (100)[001] in the c-phase and {110}<112> in γ-phase[10].

Fatigue properties are generally superior in DSSs compared to austenitic SSs due to better strength. DSSs exhibit better fatigue performance with higher fatigue limits under load/ stress-controlled test conditions. This can be ascribed to the finer grain size of DSSs' dual-phase microstructure, which assists in impediment of fatigue cracks developed at grain boundaries, slip bands and inclusions[1]. Initiation of fatigue cracks differs slightly between cold and hot-rolled steels, specifically with regards to their observed cracking mechanisms. However generally speaking, literature supports the typical cause of fatigue cracks being the accumulation of strains around surface defects. M.W. Tofique for example looks into these mechanisms quite closely as part of an investigation into very-high cyclic-fatigue strength (VHCF) evaluation of DSSs[13]. T. Björk et al. studied the fatigue strength of welded DSS and SDSS alloys both with- and without post welding treatment, eventually finding that both sets of samples performed exceptionally under low-stress ratios[14]. Previous studies also indicate a dependency of tensile-fatigue performance on the yield strength of DSS. In instances where the max-stress applied per-cycle approaches that of the yield-strength of the alloy, the resultant plastic deformation is sufficient to allow formation of small fatigue cracks. Under immersion in corrosive media, relative fatigue strength of DSSs can be correlated to their respective resistance to various mechanisms of electrochemical attack. For example, the fatigue strength performance of DSSs in seawater solution and in air can be correlated as a function of resistance to pitting corrosion, namely, an alloy’s PREN value[15],[16].

2.2.i Secondary Phases

If correct measures are not taken during the cooling & solidification process of DSS alloys, a number of deleterious secondary/ intermetallic phases can develop within the microstructure. Once established, these precipitates extensively disrupt and degrade the corrosion and mechanical performance of the alloy, often leading to failure in service [17]. Avoiding formation of these detrimental precipitates is feasible so long as the correct cooling rates at specific compositions are used with reference to the CCT and TTT curves of DSSs (ref. fig 2). Among these phases are intermetallic elements such as sigma (σ), chi (χ), tau (τ), pi (π) and then precipitates such as nitrides (e.g. CrN), carbides ($M_{23}C_6$/ M_7C_3) and secondary austenite- (γ_2).

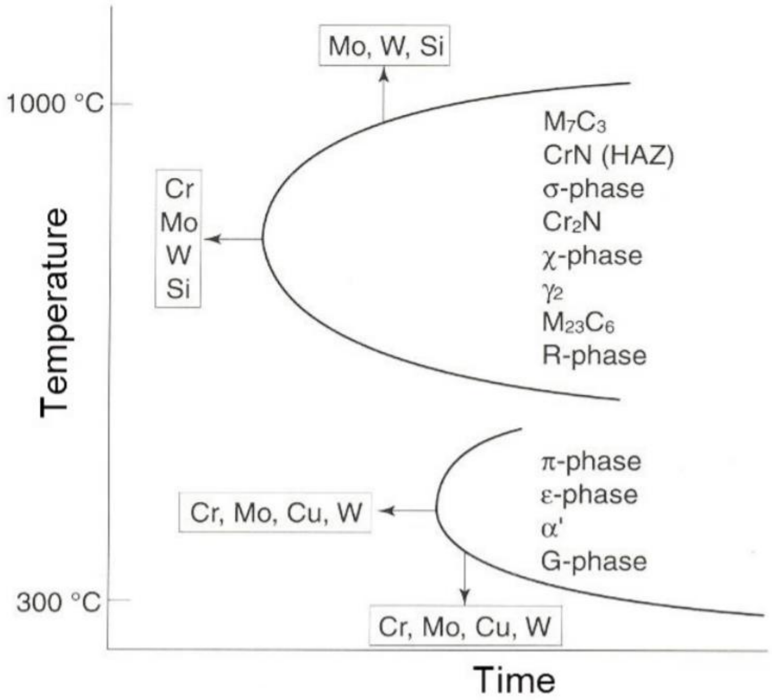

Figure 2: Secondary phases of DSSs and the effects of alloying elements on the shape and location of their Time-Temperature-Transformation curves [10],[18]

Amongst the range of secondary phases/ precipitates, the σ-phase can be deemed particularly important. This is due to the extent to which it can degrade the alloys’ mechanical toughness & corrosion properties, in addition to its potential range of stability in DSSs compared to the other phases. Such detriment typically comes about via the localised depletion of Cr & Mo, at σ-sites, from the eutectoid precipitation of the phase. The resultant depletion de-stabilised the passive film making the alloy more susceptible to corrosive attack[19].

σ is a tetragonal-crystalline intermetallic which forms in DSS preferentially at ferrite-austenite grain boundaries across high working temperatures (600-1000°C) and is rich in elements of Cr, Mo and Si [10][16]. As such, additions of Cr and Mo which work to improve an alloys' corrosion properties, can potentially also conversely deteriorate them – due to these elements stabilising σ. This bears true even more so for SDSSs, which considering their increased Cr and Mo proportions, are inherently more sensitive to σ formation and thus require faster cooling times. Cr and Mo additions increase the rate of precipitation as well as the volume fraction of the σ-phase, resulting in the displacement of the "C" curve on the TTT diagram towards shorter times. Mo particularly is known to extend the range of stability of σ-phase towards higher temperatures [10][20]. Figure 2 aptly shows the resultant effects different alloying additions have on the C-curve, with Mo in particular demonstrating the most benefit to detrimental phases despite its well-noted benefits to stabilisation of the passive film.

Charles et al [21] found that tungsten can also have a similar-effect as Mo when it comes to stabilising the σ-phase by way of increasing its precipitation rate, as well as expanding its C-curve on the TTT to higher temperatures. It was also observed that Cu seemed to have no effect on the precipitation kinetics of σ. σ-phase preferentially precipitates at either (1) triple grain-boundary junctions of γ/α in DSSs, (2) Cr-rich ferrite sites in ferritic SS or (3) at γ/α grain boundaries in austenitic SS. It is a product of the transformation of ferrite into secondary austenite and σ ($\alpha \rightarrow \gamma_2 + \sigma$) and once precipitated, grows within the ferrite phase [10]. Formation of σ in production is typically avoided by quenching of DSS alloys from high temperatures (1200°C), whilst avoiding its range of formation (1000-600°C). Doing so at a sufficient cooling rate suppresses precipitation due to σ's relatively slow transformation; as a result of its large tetragonal structure (32 atoms)[1].

2.3. Corrosion of Super Duplex Stainless Steels (SDSS)

Corrosion properties of alloys in industry are of particular interest when aiming to anticipate the behaviour/responses of products in particular service environments. In SS, propensity to corrosion is primarily dictated by chemical composition of the alloy [22],[23]. The ability for an alloy to resist chemical attack depends heavily on its tendency to produce a protective passive layer, preventing the ingress of aggressive species. The formation & stability of said passive layer is directly influenced by multiple factors, including chemical composition, alloy composition, pH, applied electrode potential and electrolyte composition. [24],[25]. The electrochemical characteristics, thermodynamics and kinetics of the passivation process have been extensively researched and presented in literature[26].

Passivation and breakdown, specifically in the context of corrosive aqueous electrolytes, is a somewhat complex process which we try to explain via correlation with current/potential behaviour of alloys. A large part of this complexity stems from the sheer variability of this measured behaviour, based on factors such as temperature, electrolyte composition, alloy properties, boundary conditions (metal/electrolyte/air) and electrodes. As a result of this, studies into corrosion resistance of alloys focused on observing and analysing passivation behaviour are typically done under prescribed conditions (pH, ion concentration, temperature). These studies often serve to evaluate the ability to passivate and remain passivated until the point of breakdown within service environments.

Inclusions in the form of oxides born from alloying additions - such as from chromium, sulphur and manganese, are often focal points of root-cause studies due to their tendency to cause localised breakdown. As such said studies commonly relate to localised pitting resistance examples again due to its correlation with point defects such as inclusions[27]–[29]. Electrochemical Impedance Spectroscopy (EIS) is one of the commonly used techniques to evaluate the characteristics of passive films, usually alongside surface chemistry analysis such as X-ray photoelectron spectroscopy (XPS), energy-dispersive spectroscopy (EDS) and Auger electron spectroscopy (AES). EIS quantifies electrical measurements of resistivity and capacitance changes in the oxide layer to anticipate propensity to breakdown or passivation[26].

In a study of passivation chemistry on SDSS, Cui [30] et al sought to investigate the passive film growth and dissolution kinetics of commercial SAF 2507 (UNS S32750) SDSS. Following preliminary potentiostatic polarisation to remove air-formed oxides, samples were polarised in a series of sodium chloride solutions. Solutions tested were composed of (a) modified sodium chloride sparged with N_2 (no oxygen), (b) acidic sodium chloride sparged as well as pH-adjusted using Acetic acid (CH_3COOH) and (c) regular sodium chloride containing oxygen (un-sparged). Polarisation was carried out within a potential range of $-0.8V_{SCE}$ to $1.3V_{SCE}$, at a scan rate of 0.5mV/s, then followed by potentiostatic polarisation immersion for 1 hr post-testing. Capacitance measurements for impedance were taken following 1 hr of polarised immersion at an anodic potential, during a sweep from anodic to cathodic potentials. A frequency range of 10mHz to 100kHz was employed during the sweep, with an step-rate 25mV/s using a 10mV AC amplitude signal at 7 points per decade.

Impedance measurements presented in the form of Bode and Nyquist plots showed consistent passivation kinetics across all 3 solutions. Bode resistivity measurements from low to middle frequencies were linear with moduli close to -1, then phase angles evolving between 60°C and 85°C, indicating a mainly capacitive film. Measured polarisation resistance plots showed a lack of oxygen to have minimal effect on film resistance, unlike with the presence of acidic media. In spite of this, capacitance measurements indicated an increase of the film's electric field strength (E_0) associated with increased oxygen in the passivated layer. EIS and XPS film composition analysis found that acidification of the ASW solution lead to a reduction in film thickness, as well as an increase in amount of oxidised Cr, Fe(II) and hydroxides in the passive film. It was also shown that during pre-passivation in acidic media, the protective layer forms as a thin film consisted mostly of Cr-hydroxides. Within the passive region however, the film develops a thicker depth with a higher oxide content.

With potentiodynamic polarisation, oxygen presence was shown to have distinct effect on the position of the cathodic curve portion, yet not the actual shape of the curve. Compared with that of the aerated solution, the cathodic sweep of SAF 2507 in deaerated conditions was shifted to lower current density densities (left of plot), but unchanged in general shape. This lead to conclusions of H_2O reduction contributing little to the overall cathodic reaction. In the acidic solution, lack of oxygen from sparging meant that H^+ ions instead of H_2O drove the $2H^+ + 2e \rightarrow H_2$ reaction. What's more, increased transpassive dissolution was present in acidic ASW, this was attributed to the breakdown of Cr(III) in the oxide layer.

Långberg, Örnek et al[26] pointedly investigated and evaluated the transpassive breakdown of solution-annealed UNS-S32750 SDSS samples immersed in 1M NaCl solution. In efforts to redefine what qualifies transpassivity, the study utilised EIS measurements as well as operando synchrotron X-ray analysis (XRF, XRR, GIXRD) to extensively show the onset- and development of transpassive breakdown.

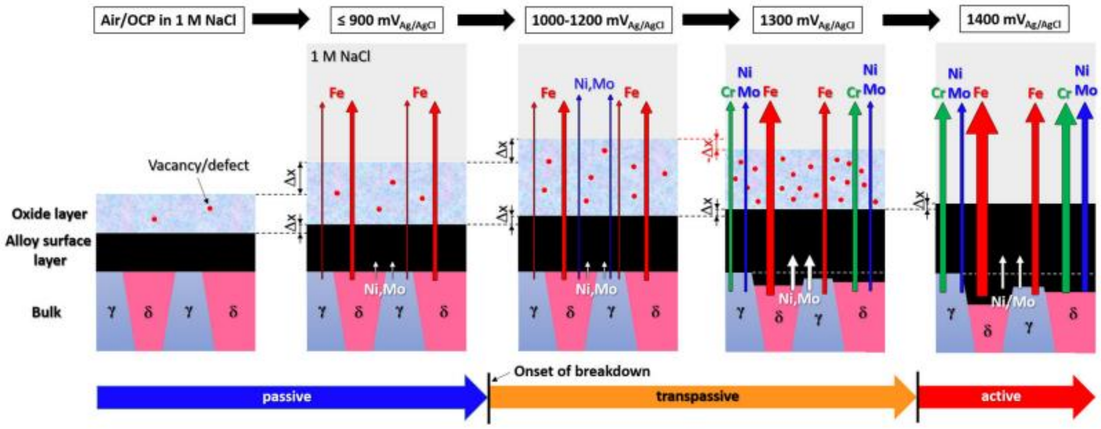

Figure 3: Summarised findings of dissolution mechanics during anodic potentiodynamic polarisation of UNS S32750 (SAF) SDSS in 1M NaCl. Arrow thickness is representative of dissolution magnitude associated with potential increase[26].

Operando synchrotron XRR was accurately used to observe thickness and density of the passive layer and alloy surface layer, all while working under the assumption of the 2-layer oxide film model. The passive layer is usually a few nanometres thick, increasing marginally as potentials rise through the passive range (900 mV/$_{Ag/AgCl}$ onwards). Subsequently, in the range of transition from passivity to transpassivity 1000-1200 mV/$_{Ag/AgCl}$, enhanced anodic dissolution of Fe leads to a decrease in passive layer density, despite continued increase in the layer thickness. XRR data coupled with electrochemical measurements infer this change in density to be responsible for the resultant increase in anodic dissolution, by way of introducing vacancy defects in the PL allowing further ingress of aggressive ions.

Data then showed onset of transpassive breakdown at 1000mV/$_{Ag/AgCl}$ with Fe being the main element of dissolution, along with continued progressive thickening of the passive layer up to 1200 mV/$_{Ag/AgCl}$. At 1200 mV/$_{Ag/AgCl}$ dissolution of both Ni and Mo could be detected with the possibility of also Cr. However at this point the passive film was still present. From 1300 mV/$_{Ag/AgCl}$ onwards, rapid dissolution of Cr is detected as well as for Fe, the rate of oxide dissolution was seen to exceed that of formation leading to the thinning of the passive layer. It is at this point at which both the degradation of thickness as well as density of the passive layer is first noted.

Consequentially, authors stipulate the transpassive breakdown i.e. transition of passive behaviour to transpassive behaviour, actually occurs over a definable potential range (~200mV in study). Moreover, it can be characterised by electrochemical changes occurring at lower potentials, accompanied by structural & compositional changes at higher potentials. It was noted however, the uncertainty of defining transpassivity solely by an increase in current density, due to the increasing potential-driven kinetics of the oxygen evolution reaction likely contributing to current density transients through this E-range also.

2.3.i Corrosion Resistance - PREn

With a Pitting Resistance Equivalency number (PRE$_N$) of ≥40, SDSSs have excellent resistance against pitting corrosion and stress corrosion cracking in aggressive chloride-containing environments. The PRE$_N$ is simply a measure of an alloy's pitting corrosion resistance based on the most beneficial alloying additions. There are multiple versions of the equation but the commonly used is expressed as:

$$\boldsymbol{PRE_N} = \%\boldsymbol{Cr} + \mathbf{3.3} \times \%\boldsymbol{Mo} + \mathbf{16} \times \%\boldsymbol{N}$$

And for instances where there is also Tungsten alloyed with the metal:

$$\boldsymbol{PRE_N} = \%\boldsymbol{Cr} + \mathbf{3.3} \times (\%\boldsymbol{Mo} + \mathbf{0.5}\% \times \boldsymbol{W}) + (\mathbf{16} \times \%\boldsymbol{N})$$

The PRE number is derived from empirical formula originally developed by Lorentz and Medawar in 1969 to approximate the relative corrosion performance of corrosion-resistant alloys (CRAs). It has since been revised and/or supplemented by various research & standardisation bodies such as NORSOK and ISO. Both these organisations have distinct standards for estimating chemical resistance of alloys under certain conditions, standards which do not always agree on the benefit of additions like tungsten, such as with NORSOK M-001 and ISO 21457. A notable example of unanimous revision was the addition of the subtext “N”, denoting the favourable contributions of nitrogen.

Although a good measure for anticipating general corrosion resistance, consideration must be given to constituent phases (i.e. for SS, ferrite and austenite) in order to better anticipate corrosion behaviour. Pragmatically speaking, an alloy’s corrosion properties are defined by its constituent phase with the lower PRE_N value, with optimal performance occurring when both phases possess similar PRE_N values. Difference in the proportion of alloying elements distributed (partitioned) between the two phases in DSSs naturally cause a difference in nobility and potential between the phases[31]. Meaning that when immersed in an active environment, γ and α phases react differently depending on a number of factors. Typically in DSSs, the BCC α-phase tends to form with a lower nobility and hence, often preferentially corrodes anodically via dissolution. The distinct corrosion properties of austenite and ferrite phases also serve to effectively hinder the propagation of micro-cracks in chloride-containing solution during environmentally assisted cracking (EAC). Engelberg et al for example noted how anodic activity at propagating crack-tips within ferritic phases of modern SSs is suppressed when confronted with phase-boundaries of austenite, which typically has a higher corrosion potential than its galvanic couple, ferrite[32].

2.4. Alloying Additions to Duplex Stainless Steels – Tungsten and Copper

There are a number of alloying additions that can be made to stainless steels (SS) in order to enhance their mechanical and corrosion properties for specific conditions across a range of environments and applications. Chromium, nickel, molybdenum, copper, manganese, silicon and nitrogen are all typical alloying additions made to SSs, serving as either stabilisers and/or strength & corrosion resistance enhancers. Chromium (Cr) can be considered to be the primary alloying component which grants SSs their superior corrosion properties, compared to other grades of steel. This is due to its contribution to the formation of the passive chromium-oxide film on the surface of the alloy, which acts as a protective barrier to chemical attack. It is typically alloyed in proportions ranging from 10wt%-30wt%, although to be classed as a stainless steel alloys need only have a minimum proportion of 10.5wt% Cr. Table 1 below briefly lays out the range of typical alloying additions for DSSs, their resultant impact on pitting & crevice corrosion resistance and also the practical limitations of addition for said elements in terms of weight percentage .

Table 1 – Typical DSS Alloying elements and phases, their resultant effects on corrosion resistance and the practical limitations of their addition (wt%) – adapted from Gunn's book[1]

Element	Impact on Alloy	Practical-limitation of addition
C	Causes precipitation of chromium carbides with accompanying chromium depleted zones	About 0.03% maximum
Si	Si stabilies passive film	About 2% maximum, due to its effect on structural stability and on nitrogen solubility
Mn	Mn-rich sulphides act as initiation sites for pitting. Mn may also destabilise the passivefilm.	About 2%. Higher levels may also increase the risk of intermetallic precipitation
Si	Sulphides, if not Cr-, Ti- or Ce-rich, tend to initiate pitting attack	About 0.003%, if maximum pitting resistance is required. For reason able machinability, upto 0.02% allowed
Cr	Cr Stabilises passive film	Between 25 and 28% maximum depending on the Mo-content. Higher Cr-content increases the risk of intermetallic precipitation.
Ni	Increased Ni, other elements constant, dilutes the y-phase with regard to N, which in turn decreases the PREn of the y-phase. If the alloy is very sensitive to precipitation of chromium nitrides, Ni can have a positive effect.	Ni should primarily be used to give the alloy the desired austenite content.
Mo	Mo stabilises the passive film, either directly or through enrichment beneath the film	About 4-5% maximum depending on the Cr-content. Mo enhances the risk of intermetallic precipitation.
N	N increases the PREn-number of the y--phase dramatically, not only by increasing the N-content of that phase, but also by increasing the Cr and Mo contents through their partitioning coefficients.	About 0.15% in Mo-free grades. About 0.3% in super duplex grades and some 0.4% in 25% Cr, high-Mo, high-Mn alloys.
Cu	Disputed for DSS; widely believed to be beneficial for enhancing surface insolubility of alloys against agrgresive ions. Otherwise marginal positive/negative effects	Approx. 2.5% - larger additions reduces hot-workability and increases unwanted hardenability
W	Likely same as Molybdenum's effects (synergistic). Also increases tendency for precipitation of intermetallics	Not Given

The non-uniform partitioning of these elements into the constituent phases of duplex alloys, is the reason for the differing corrosion properties of individual phases. N and Ni preferentially partition into γ while α is enriched in Cr and Mo. Besides the atomic & chemical properties, partitioning of these elements is heavily influenced by the post-working/processing cooling rates as well as the solution treatment conditions, namely temperature [23]. Cr and Mo are also incorporated into the composition of the oxide film in SDSS s and they produce the passivating inhibitors of chromium (III) (Cr_2O_3) and molybdate (MoO_4^{-2}). These preferentially adsorb to the surface of the steel, leading to the stabilisation and rebuilding of the passive layer by blocking ingress of aggressive species. Inhibitors are also understood to further reduce propensity to pitting by altering the pH and ion-content within developed pits, often forming insoluble compounds which block further anodic (dissolutive) reactions[1]. Hence the observed improvement in corrosion resistance with increasing additions [23]. The film produced is relatively thin, but possesses a low ionic permeability [33].

Contributions of Copper (Cu) and Tungsten (W) alloying additions to pitting and crevice corrosion properties have been researched and debated in the field of corrosion, particularly across standardisation committees responsible for certifications (see ISO and NORSOK examples).

2.4.i. Tungsten

Historically, tungsten has long-been understood to be highly beneficial as an alloying addition to the mechanical strength of SSs across a wide range of temperatures. Depending on the application it can be added in weight proportions ranging from up to 2% for stainless steels. This improved strength and hardenability develops due to increased stability of the strength-influencing ferrite phase, via the precipitation of fine carbides within the microstructure (i.e. solid-solution strengthening)[34]. Depending which elements it is alloyed with, W can offer even greater strength & hardness levels in steels by forming complex carbides which are distributed across the microstructure. Although it’s worth noting that this comes at the cost of reduced plasticity and impact-strength[35]. In industry, W is added to SS alloys in environments subject to high friction or heat, due to the added stability it gives at higher temperature ranges, hence the common usage of high-speed stainless steel grades (HSS) in tooling and excavation applications.

Notwithstanding this, Tungsten has not yet been universally recognised as a net-positive contributor to pitting corrosion resistance, as inferred by its absence from the standard NORSOK-001-spec PREn equation. One reason for this dispute is the dichotomy of its relationship with addition of molybdenum; where some researchers believe its addition, in contrast to Mb, to be detrimental to corrosion performance, whereas others believe W exhibits a strong positively synergistic effect with Mb when added. Despite this dispute, there appears to be consensus between academics on the presence of an optimal range of Tungsten alloying additions, outside of which, the effects become negligible or even detrimental[36].

This being said, there are multiple accounts from studies testifying to both the benefit and detriment of W to electrochemical properties. J.S. Kim[37] et al presented an instance of such benefit when looking into the influence of W and Ni additions on repassivation behaviour of rolled & treated SSs. The study found that in acidic solutions, SS specimens with W additions substituting for Mo displayed decreased passive current densities in the active region during potentiodynamic polarisation sweeps. Repassivation properties were also improved in the W-dominant alloys, due to W's enhancement of stabilising Mo-compounds in the passive film; namely Iron (II) Molybdate ($FeMoO_4$). Despite this however, an increased active current density was also observed in high-W alloys[37]. Ogawa et al. [38][39] found that Tungsten aided to retard the growth rate of the deleterious sigma-phase in DSSs at low temperatures, as well as improve the resistance to localised pitting corrosion. On the contrary however, in high-temperature conditions W was also observed to accelerate growth of χ/σ-phases. This detrimental effect of W was also somewhat corroborated by Nilson et al[40], who found W-rich weld metals to exhibit higher proportions of intermetallic phases than W-poor and W-free alloys. In the study, precipitation kinetics of deleterious phases in SDSSs and their relationship to chemical compositions were investigated. 3 rectangular SDSS plates of identical preparation, geometry and composition (Sandvik SAF2507 -UNS32750) were welded in horizontal-series using 3 filler metals. These filler metals were identical in base composition and distinguished only by their proportions of W and Cu, i.e. 1 without Cu/W, 1 with W only and the last with Cu & W.

After being subjected to isothermal aging treatments and water quenching, followed by optical microscopy and SEM-EDX/WDX analysis, results showed a fairly clear relationship between presence of W and prominence of χ, σ and γ_2 in microstructure.

Ogawa et al [41], in studying the effects of W on the toughness & pitting corrosion behaviour of HAZ's within modified DSSs, found and presented a distinct benefit of pitting corrosion resistance increase with addition of W to the base alloy. Base steels SUS329J4L, composed of 25%-Cr, 7%-Ni, 3%-Mo and 0.3%N were alloyed with W in varying amounts up to 4%, then formed into 100mm x 300mm x 9mm plates, followed by machining and finally TIG welding with matching filler at 17 kJ/cm. 24 hr critical pitting temperature immersion tests were run in 10% $FeCl_3(aq)$ solution, revealing that higher W-additions increased the pitting resistance of the base alloy. The HAZ's pitting resistance was also increased with greater % of W up to 2%, after which no added benefit was observed until 4.2%, where effects then became detrimental. Contrastingly, Charpy impact testing on the artificially-notched HAZ's of post-welded samples indicated a detrimental effect of W additions on impact toughness. Most likely attributable to increased presence of intermetallic compounds in the experimental temperature range (800-1050°C). It is worth noting however, that practically suitable values of toughness were achieved with 2%-W, in AT of -30°C and >80 J/cm^2 impact energy. Beyond this W %, detrimental effects on toughness were significantly worsened.

Haugan et al[36] were able to convey a distinctly positive benefit of W addition when subjecting 2 DSS alloys to a series of electrochemical experiments. The two base alloys, UNS-S32750 and -S39274, modified to contain low and high W proportions respectively, were tested in standard natural seawater conditions; 3.5 wt% NaCl at temperatures ranging from 20°C - 95°C. Alloys were subjected to anodic circular Potentiodynamic polarisation (CPP), open-circuit potential (OCP) and fixed anodic-potential temperature ramping testing methods. It was found that at 2.2wt%, W provided a significant increase in E_{Pit} and E_{Rep} values and benefitted pitting and crevice repassivation kinetics as well.

2.4.ii. Copper

Copper (Cu) is another key alloying element, particularly in Duplex Stainless Steels (DSS) used in environments containing hydrochloric and sulphuric acids. Copper has long been an treasured asset in the materials industry, thanks in no small part to its chemical nobility, formability, machinability and electrical conductivity. Numerous research studies [42]–[45] support one main attribute of copper's corrosion resistance in sulphuric media being its suppression of anodic dissolution; commonly explained to be achieved by enrichment of Cu-atoms at the surface, subsequently forming insoluble compounds around sulphur inclusions. This prevents further pit formation and growth, thus impeding further reaction (dissolution). Complimenting this effect, the enrichment of Cu-atoms at the surface of the metal during anodic dissolution are said to provide a secondary passivating layer. The comparatively higher nobility of copper-sulphide as opposed to iron-/nickel-sulphide, causes its preferential formation in addition to the original chromium-oxide passivating layer [44].

In one such study, Jeon, Kim et al [46] sought to observe the effects of Cu on passivity and corrosion resistance of Hyper-duplex Steels (27%-Cr, 7%-Ni), both in passive and active states. Subsequent data showed that Cu had a distinct benefit on active corrosion resistance of SS alloys immersed in sulfuric acid. Potentiodynamic testing conducted on samples in 2M H_2SO_4 solution showed I_{Corr} and I_c to be higher for Cu-rich samples immersed at 60°C. One of the attributed reasons for this was Cu's tendency to reduce the overpotential of the cathodic reaction, thereby promoting transition to passivity by facilitating formation of the passive film. Another was Cu's affinity for adsorption to oxygen, which would also aid to better passivate the alloy. In spite of this, the Cu-rich alloy was also observed to have an increased passive current density (I_p), indicating a reduction in corrosion resistance within the passive region. These preventative benefits of overpotential and dissolution-retardation can also be observed in Hong, Lee, Kim and Yoon's study [43] of low-Cu steels in sulphide environments. In it, it was likewise noted that in acidic media of 10 wt% H_2SO_4, the hydrogen evolution reaction (HER) overpotential was measured to be higher with increasing proportions of Cu, therefore, suppressing the cathodic reaction of hydrogen evolution. Overall, alloys in this study with higher amounts of Cu exhibited slower corrosion rates, partially attributed to accelerated redeposition of Cu^{2+} ions onto the alloy surface. This electroplating effect was observed to impede further dissolution of the alloy, indicated by the subsequently reduced current densities observed within said alloys in polarisation experiments.

Banas et al [45] investigated coppers influence on ferritic and duplex stainless steels polarised in sulfuric acid solution. Ferritic (Fe-18% Cr) and Duplex (24%Cr, 6%-Ni, 3%-Mo) SS samples were polarised in 1M H_2SO_4 and 1M H_2SO_4 + 1M NaCl solutions at 20°C. The results obtained pointed towards a correlative relationship between increased copper additions and decreased passivity in ferritic steels. This was explained to be due to the lower solubility of Cu in ferrite compared to austenite. Where copper additions provided solution strengthening to austenitic phases, contrastingly, ferritic phases saw increased growth of ε-phase and thus, were more susceptible to localised attack. In the duplex steel, there was an observed absence of ε-phase in ferritic phases despite the solubility of Cu being exceeded. Researchers believed this to be due to higher solubility of Cu in the austenite phase which is comparatively larger in duplex SS as opposed to the ferritic. in addition to this, it was noted Ni also aids to discourage growth of ε.

Contrastingly, mass-loss immersion tests performed by Kivisäkk et al[47] ,indicated no significant benefit of copper additions on iso-corrosion curves. With immersion tests of various SDSS samples in both hydrochloric and sulphuric acidic media; all varying in Cu wt% from 0.02 to 2.01%, it was concluded Cu provided little to no benefit depending on which solution tests were performed in. In hydrochloric acid, Cu was found to have negligible effects, whilst in diluted sulfuric acid (weight % up to 40) it was also observed to have either little or no detrimental effect. Further to this, the higher Cu wt%-alloys exhibited the lower corrosion limits. This sentiment was echoed in the study of De Lima et al[42] also, where through critical pitting temperature tests, it was established that Cu proportions of 3.1% in cast DSS diminished the pitting corrosion resistance, particularly in chloride media. Similarly, in 0.3M H_2SO_4 solution addition of Cu was also found to negatively affect the onset of passivation.

2.5 Corrosion Characterisation Techniques – Potentiodynamic Polarisation and SVET

Electrochemical characterisation techniques help to isolate, identify and analyse the symptoms and resultant impacts of corrosion phenomena. Development of these techniques is crucial for better anticipation of metal and alloy's performance in critical service environments. The reason for this is the complex and highly variable nature of corrosion and it's strong dependency with parameters which are rarely consistent in service, such as varying pressure, temperature, chemical composition & concentration, and alloying proportions.

Characterisation techniques are often oriented towards observing a particular mode of corrosion, either uniform (generic) or localised in nature. With generic forms being cases where dissolution occurs equally/uniformly across the surface, showing no visual separation of anodic and cathodic sites. Then localised cases showing the opposite; preferential attack in specific areas of the active area determined by electrochemical potential differences.

Leygraf and Graedel aptly conveyed the fundamental principles and deliberations concerning mechanisms of both indoor and outdoor atmospheric corrosion in their book[48]. In it, they discretise the process into distinct preliminary, intermediate and terminal/final stages. In line with the scope of this study, literature presented will focus more on localised corrosion characterisation as opposed to bulk/general techniques. Such techniques are succinctly presented and discussed below.

2.5.i. Potentiodynamic Polarisation (PP)

Potentiodynamic polarisation is an effective localised corrosion characterisation technique, used to assess the susceptibility of an alloy to breakdown in a specified electrolyte solution. In principle, PP involves imposing a chosen potential difference in DC across a working electrode (sample) through a defined range of potentials. This imposed potential is varied either positively (anodic-going) or negatively (cathodic-going) and the resultant observed current density from doing so is used to interpret electrochemical behaviour of the alloy i.e.

breakdown, passivation, transpassivity etc[49]. Cyclic Potentiodynamic polarisation is a common variant of the PP Testing method, used specifically for analysing an alloys resistance to localised pitting corrosion. It involves polarising the applied potential across the working electrode, either anodically or cathodically, until the current density output reaches a pre-specified value, at which point the scan polarity is then reversed and continued until the starting potential is reached. Cyclic polarisation experiments are often set-up and executed according to the ASTM G61 or F2129 standard, with regular polarisation scans being covered in ASTM G59[50].

Potentiostats measure current and control the potential difference between a series of electrodes connected in an electrochemical cell. These electrodes are typically set up as a standard 3-electrode cell; (1) Working, (2) Reference and (3) Counter/ Auxiliary, with each serving a specific purpose in the cell setup. Depending on the type of electrochemical experimentation being undertaken, electrodes will be ideal conductors either made of an inert element (e.g. gold, platinum, rhodium) or a reactive element (e.g. copper, zinc, silver)[50].

The working electrode (WE) is the one at which current & potential is measured, often making it the target specimen in experiments. Usually made of an inert metal, its surface hosts the electrochemical reactions of the cell setup. The reference electrode (RE) measures the potential of the working electrode i.e. as a reference point. As such it is required to have a near constant potential when no current is present, in order to provide accurate readings for the WE when potential is applied to the cell. Such consistent potential values are usually maintained through an inert REDOX reaction. Conventional electrodes used as references in electro-chem experiments include Silver/Silver Chloride (Ag/AgCl) and Saturated Calomel Electrode (SCE).

Lastly, the Counter/Auxiliary electrode (CE/AE) provides an end point for current to flow from/ to with respect to the WE, thereby completing the circuit of the cell. In order not to disrupt/ influence experimental results, it too is usually made of an inert conductor such as platinum (Pt) or graphite[49], [50].

2.5.ii. Scanning Vibrating Electrode Technique (SVET)

The scanning vibrating electrode technique (SVET), is a non-invasive, non-destructive electrochemical analysis technique[51]. In corrosion studies, SVET utilises a vibrating micro-electrode tip to sense ionic current variations (i.e. corrosion) through the electric field of electrolyte solution. This tip is vibrated via an oscillating piezo-electric unit and when used near the surface of a corroding specimen, it can detect local anodic and cathodic interactions with relatively high resolution[52]. These interactions are presented as a series of positive (anodic) and negative (cathodic) current density quantities distributed across the entire scan area (map). Thus, giving good indication of the distribution of oxidation and reduction reactions across a given scan area. When multiple scans are performed in succession, their resultant maps provide a progressive account of corrosion evolution across the entire surface[51]. It is for this reason that SVET exhibits a distinct advantage over bulk-characterisation techniques such as Potentiodynamic polarisation. With PP, measured electrochemical interactions are only presented as a general current density, giving no indication of the proportion of anodic/cathodic REDOX reactions at a given time in sweeps.

The process of measurement using the SVET begins with a conductive sample immersed in electrolyte solution. The conductivity of the electrolyte, in addition to local REDOX activity at the sample surface, results in development of an equipotential gradient at the surface i.e. an electric field (depicted in fig. 4B). A conductive microelectrode probe head is brought into close proximity with the surface (around 50 to 200µm), then axially-vibrated perpendicular to the sample's surface (fig. 5) via a piezo-actuator unit. It is this vibration that eventually enables the modulation of the resultant signal, which is later demodulated into the desired DC current density value[51], [53].

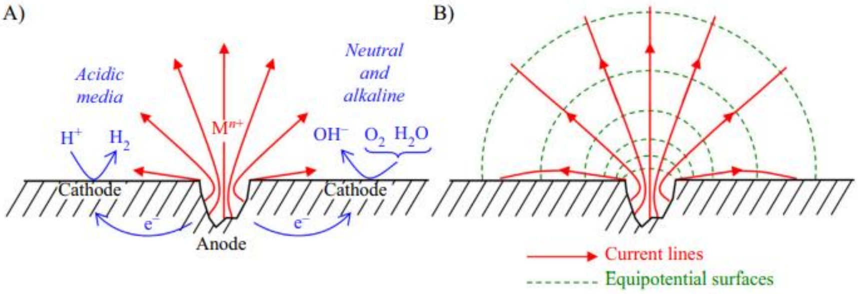

Figure 4: Diagram showing electrochemical corrosion cell ion movement and electrode formation in acidic, neutral and alkaline media (a), as well as current lines between anode and cathode (b)[51].

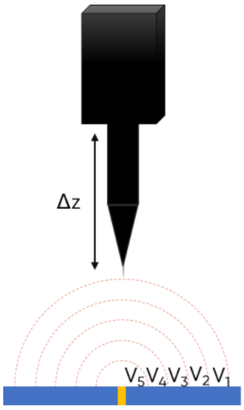

Figure 5: Schematic of electric field distribution at metal surface under SVET probe at a oscillation distance of $_{\Delta}$z

The probe head picks up the potential difference (∂V) at various points in the solution (x,y,z) across its vibration span ∂r (usually around 10-40µm in length) and equipotential region. Voltage measurements are determined by the electrometer, which alongside the z-axis sin-wave amplitude signal (obtained via the lock-in amplifier), allows for calculation of the local potential gradient in solution (∇Φ) given by the equation:

$$\nabla\Phi = \frac{\partial \mathrm{Vx}}{\partial \mathrm{rx}}\boldsymbol{i} + \frac{\partial \mathrm{Vy}}{\partial \mathrm{ry}}\boldsymbol{j} + \frac{\partial \mathrm{Vz}}{\partial \mathrm{rz}}\boldsymbol{k}$$

Terms ***i, k*** and ***j*** are standard x, y, and z directional unit vectors, respectively[51]. These gradient values can then be used to calculate the electric field strength (E), calculated via:

$$\mathrm{E} = -\nabla\Phi$$

Subsequent to this measurement, solution conductivity (k) between the vibration span can be calculated using the obtained amplitude signal and solution resistivity (ρ)[53]. From this point, the E and k measurements can simply be multiplied using Ohm's law to give the local current density value, ***i*** [52].

$$i = k.E$$

Considering most SVETs make solely omnidirectional field measurements, usually perpendicular to the sample surface, it follows naturally that the current density flow perpendicular to the sample surface is:

$$i_z = -k\,\frac{\partial \mathrm{Vz}}{\partial \mathrm{rz}}$$

The bulk-signal picked up by the probe head is high impedance, hence the need for the electrometer to measure the signal response alongside distinction using the LIA. Offsetting the measured 'noise' signal with the LIA's generated sin wave signal (demodulation) results in the desired DC current density measurement[51]. Thus demonstrating the SVET's capability for producing high signal-to-noise data ratio [52], [54].

Feurtes et al [55] used SVET analysis as a tool for investigating corrosion resistance of TIG-welded SAF-2507 SDSS and standard 316 SS joints. In the study, the initiation and propagation of corrosion activity as well as the dissolution of oxides was electrochemically mapped and represented using SVET current density maps. This was done in the hopes of evaluating efficacy of various post-weld cleaning methods, including; (1) brushing, (2) brushing & polishing and (3) brushing & pickling paste application. SVET maps proved useful for comparison with in-situ depiction of the dissolution process as well as for correlation with discoloration, thickness and composition of tested oxides. It was found brushing & pickling was the most effective method for improving post-weld corrosion resistance. Credited to its association with alloys displaying higher critical pitting temperatures (CPT), as well as decreased anodic activity on the surface.

In another such study, Williams and McMurray [56] characterised 2 aerospace-standard steam-turbine blade steels, FV566 (11wt%-Cr) and FV520B (13.5wt%-Cr), with respect to chloride-induced pitting corrosion using anodic-PP and SVET analysis. Polarisation scans were effective for determining E_b (pitting potential) of samples as a function of $[Cl^-]$ and T, whilst SVET scans aptly mapped and conveyed stable pitting kinetics as a function of $[Cl^-]$ on a non-polarised surface.

Samples were subjected to anodic-going polarisation with a starting potential of $0.8V_{vs\ SCE}$, at a rate of 0.5mV/s until reaching a terminal anodic current density value of $100mA.cm^{-2}$, as part of a standard 3-electrode setup with SCE as reference and Pt-gauze as counter electrodes. Scans were conducted within a water bath-immersed (temperature-controlled), gas-tight electrochemical cell in deaerated aqueous NaCl solution, with chloride concentrations $[Cl^-]$ ranging from $5\times10^{-4}mol.dm^{-3}$ to $5mol.dm^{-3}$ at a pH of 6.3 – 6.7. SVET scans were performed with a probe vibrator assembly consisted of a 125µm-diameter Pt-wire sealed within a glass sheath (probe), axially-manipulated by 3 orthogonal linear bearings driven by stepper motors. A probe vibrational frequency of 140Hz was used with a peak-to-peak vibration amplitude (A_{pp}) of 30µm ±5, at a scan height of 100µm above the immersed sample surface. Obtained voltage signals were detected by a lock-in amplifier and subjected to digital averaging (typically 10 successive measurements), for enhancement of signal-to-noise ratio. Once immersed, SVET scans commenced immediately across an isolated $10x10mm^2$ area with a 1-hour scan interval across 24 hrs, producing V_{pp} values later converted to j_z in order to produce current density development maps.

Results demonstrated both the 11wt% and 13.5wt%-Cr alloys' E_b exhibited a definable semi-logarithmic dependence on $[Cl^-]$ and T, across a range of temperatures (25-100°C) and ion concentrations ($[Cl^-]$ of 5×10^{-4} to 5 $mol.dm^{-3}$) within a near-neutral pH. This dependency was demonstrated with acquired PP results linearly plotted via the equation $E_b=A+B\times Log_{10}[Cl^-]$. Where A and B are constants attained by least-squares linear regression, A shows a linear dependence on increasing T whilst B remains temperature-independent.

SVET current density maps established a threshold for stable pitting within the 11wt% Cr when immersed in aerated electrolyte under no external polarisation. It was found within 1 hour of immersion at 20°C in electrolyte of $[Cl^-] \geq 1$ $mol.dm^{-3}$, pitting would occur. Whereas under similar conditions, the 13.5wt% Cr specimens exhibited no pitting corrosion artefacts when immersed for up to 4 days, even at the highest chloride concentration (5 $mol.dm^{-3}$). Initiated pits within the 11wt% Cr specimens were observed to steadily increase measured anodic current over the 24-hr test duration, implying no instances of repassivation, neither reversible nor non-reversible. Furthermore, pit number density was seen to increase from 1 to 4 per cm^2, correlating to an increase of $[Cl^-]$ from 1 to 5 $mol.dm^{-3}$.

2.6 Aims and Objectives for this study

This thesis is centred around a number of aims regarding the characterisation of SDSS alloys' corrosion performance in chloride media. Chloride-containing media represents a large proportion of service environments utilising corrosion resistant metals in industry, particularly in petrochemical and maritime applications. As such, it is within the aims of this study to:

1 – Generally, contribute to the understanding of the initiation, propagation and passivation stages of localised corrosion in chloride media, primarily through the use of the electrochemical techniques described in preceding sections of this chapter.

2 – Provide distinction and validation to the proposed benefits/detriments of Copper and Tungsten alloying additions in commercial SDSS alloys. Considering the lack of studies with direct comparisons thus far, doing so would subsequently validate their advertised attributes.

3 – Provide a basis for recommendation of further work that would supplement and clarify the conclusions made from this study, previous iterations to it and the wider field of wet-corrosion academia.

3. Experimental Methodology

3.1. SDSS Sample Production

The three alloys investigated in this study were provided in wholly by Langley Alloys Ltd, a producer and distributor of specialist metal alloys currently based in Newcastle, UK. Ferralium 255 (UNS-S3550), Zeron 100 (UNS-S3760) and SAF 2507(UNS-S3750) SDSS alloys were all provided in both medallion and cylindrical form (rods), with their relative compositions and dimensions listed below in table 2. All materials provided for this study were supplied with corresponding data-sheets certifying the relevant industry standards the alloys were manufactured, treated and supplied to. Including verification of post-processing mechanical, microstructural and chemical examinations.

Samples were melted via electric-arc furnace melting (EAF), followed by refinement with Argon-Oxygen Decarborisation (AOD) and then subsequently formed to cylindrical form by hot rolling. Following the hot-rolling process, the prospective-rods were peeled to achieve final dimensions as well as eliminate surface defects and acquire a more homogenous surface quality. Once formed, rods were then solution annealed at a temperature of 1060°C, followed by water-quench cooling. Post production, all alloys were certified to be free of microstructural defects and deleterious phases/precipitates by the relevant quality-assurance authorities, as per ASTM E562.

3.1.i Justification of Comparison and Denotations

As all three alloys are highly compositionally-similar and have been produced according to the same specifications i.e. processing, metallography and dimensions, It is the assumption of this study that any reproducible difference in electrochemical behaviour observed in experimentation, comes as a result of the compositional difference between the alloys' Copper (Cu) and Tungsten (W) additions highlighted below.

Table 2 – Relative compositions (Wt%) of study's SDSS alloys (UNS-S3760), (UNS-S3550) and (UNS-S750), along with industrial tradenames and chosen denotations

Ferralium®255 (UNS-S3550) - FER(Cu+)

	Cr	Ni	Mo	Cu	C	Mn	N	Si	P	S	Fe
Min	24.5	5.5	3.1	1.5		0.8	0.2				
Max	26.5	6.5	3.8	2	0.025	1.2	0.25	0.7	0.025	0.005	Bal

SAF 2507 (UNS-S3750) - SAF

	Cr	Ni	Mo	Cu	C	Mn	N	Si	P	S	Fe
Min	24	6	3				0.24				
Max	26	8	5	0.5	0.3	1.2	0.32	0.8	0.035	0.02	Bal

Zeron®100 (UNS-S3760) - ZER(W+)

	Cr	Ni	Mo	Cu	W	Mn	N	Si	P	S	Fe
Min	24	6	3	0.5	0.5		0.2	0.1			
Max	26	8	4	1	1	1	0.3	0.8	0.025	0.005	Bal

Throughout the rest of this thesis, rather than referring to the full trade-names and UNS numbers, subject alloys will be denoted by abbreviations indicating their key additions i.e. Copper surplus, Tungsten surplus and neither Copper nor Tungsten.

As such, Ferralium 255 having the highest copper addition shall be denoted as FER(Cu+), Zeron 100 will be ZER(W+) for higher tungsten addition and SAF 2507 will simply be SAF, as a result of having neither copper/tungsten additions. This denotation shall be used for both medallion and rod specimens henceforth.

3.2. PP Testing Sample Prep – Medallions and Rods

Medallion samples were drilled and fitted with a 3.25mm bare copper wire. Then silver-soldered and cleaned for establishment of electrical connection. This connection was subsequently insulated using RS-Pro self-amalgamating tape, leaving round 1-inch of bare wire for electrode connection. After wire insulation, medallion samples were cold-mounted in 2 part epoxy resin and left to cure overnight in air/temperature controlled fume cupboards.

For surface preparation, samples were all iteratively wet-grinded with silicon carbide (Si-C) paper in increasing European grit-grades from P50 to P2500. Each grade/iteration of grinding consisted of cleaning the samples with de-ionised water (DI) and ethanol.

For isolation of the active test area (for PP and SVET testing), 3M extruded 5490 PTFE tape was used to mask the general testing area, roughly 6cm^2 in size. The final test area (10mm x 10mm) was then achieved via application of G371 Lacomit varnish followed by air curing in a fume cupboard. This making method was preferred due to previous test sweeps (with samples masked only using PTFE) repeatedly exhibiting crevice-effects when reviewed post-sweep. Which thus compromised integrity of results/observations made from said sweeps due to lack of distinction between pitting and crevice current/potential behaviour.

NB: Whilst the implementation of Lacomit varnish for isolating the active area eliminated a large degree of crevice-effect conflation, it remained the case in a number of medallion-PP sweeps that crevice effects were still scantly present. In response to this, SDSS specimens were later provided in the form of rolled rods for partial immersion into electrolyte, in hopes to altogether eliminate the need for masking and hence, the opportunity for crevice formation. Medallion PP sweeps were also compared to subsequently acquired rod sweeps, in an effort to comparatively validate the observed sweep artifacts and retain credence of the data by crafting error margins.

Rod specimens were prepared metallographically similarly to medallion specimens. Progressive wet-grinding with SiC paper in grits ranging from P50 to P2500 was used to prep the surface, followed by thorough cleaning/degreasing with DI water and ethanol. As for establishing an electrical connection for the 3-electrode setup, rods were affixed with conductive brass jubilee clips connected to the Potentiostat via plier (crocodile) clips. Isolation of the active area for testing was done simply by partial immersion, 20mm, into the test solution, then held in place by desktop lab stands with insulated grips. Once the test solution was ready, rod samples were set up in a configuration similar to that of the medallion setup, depicted in fig 7 below.

3.3. PP electrolyte preparation and electrode configuration

Sodium chloride electrolyte solutions were prepared, consisted of 3.5% NaCl (0.6M) in a pH range of 3-11ph. Each solution was pH-adjusted via drop-wise addition of reagent-grade hydrochloric acid (HCL) and sodium hydroxide (NaOH). For medallions, 300-400 ml of solution was used for each electrolyte (depending on volumetric size of mounted sample). Whereas for rods, solution volume was kept to roughly 350ml. Once prepared, to remove oxygen from the electrolyte all test solutions were deoxygenated with nitrogen gas (N_2) via a tube inlet placed into the electrolyte for a minimum of 25 minutes. Immediately after, the sparge tube was raised to a level just above the solution to insulate the above airspace from oxygen ingress, as well as avoid flow corrosion effects from bubbles in the electrolyte during testing.

All preparations and experiments were conducted in an ambiently-controlled lab environment set at 25°C. A standard calomel electrode was used as the reference electrode alongside a platinum-gauze acting as a counter/auxiliary electrode. The configuration of the 3-electrode setup for OCP and PP testing of this studies' medallion & rod specimens is shown in figures 6 and 7 respectively below:

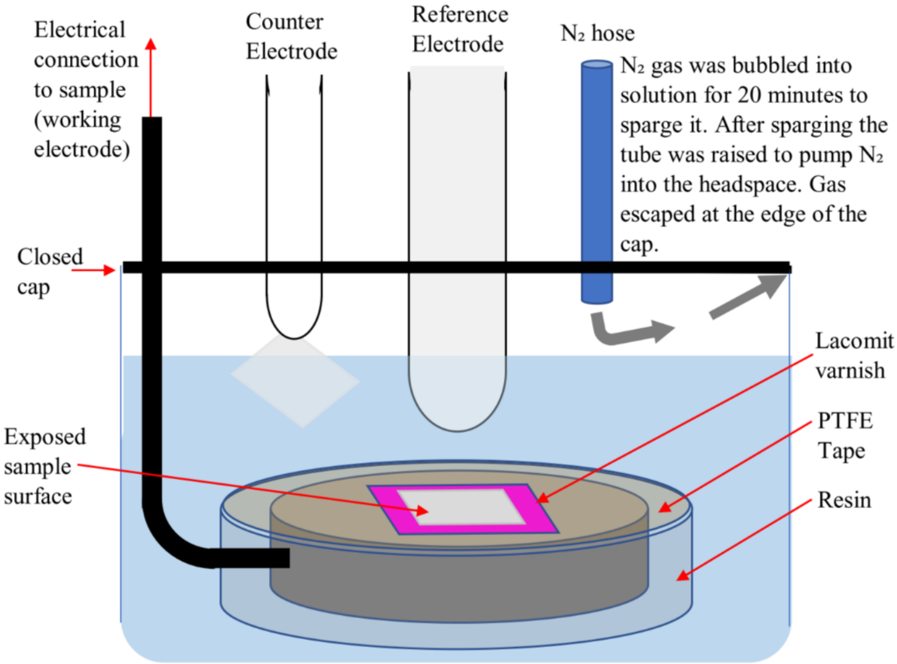

Figure 6: 3-electrode sample setup for Potentiodynamic Polarisation Tests (Medallions)[57]

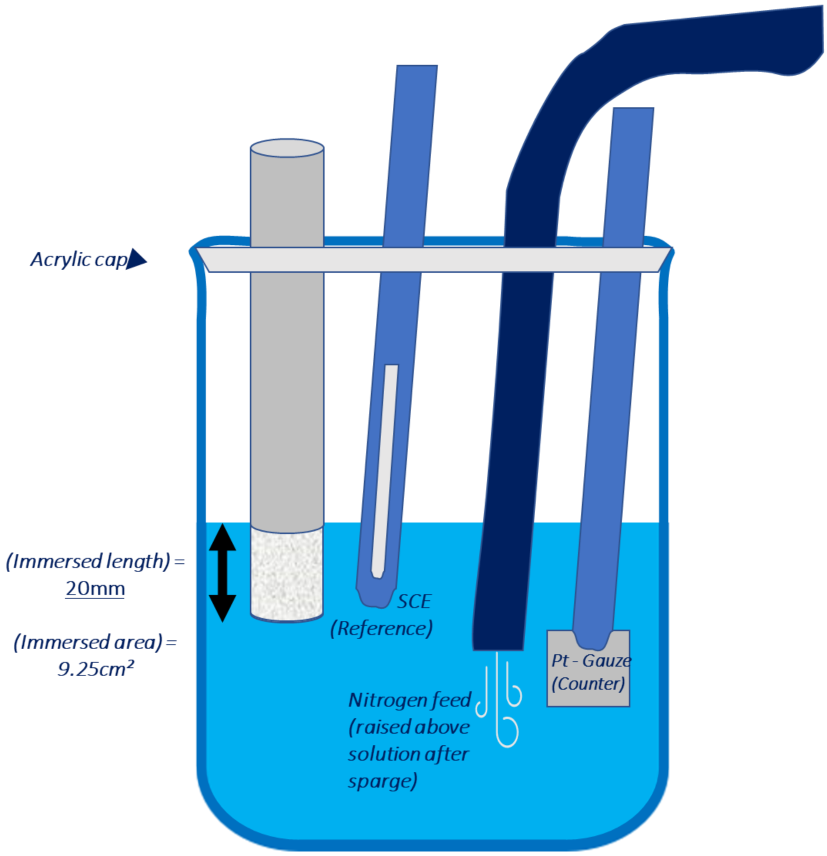

Figure 7: Diagram of 3-electrode sample setup for Potentiodynamic Polarisation Tests (Rods)

Polarisation experiments were conducted with a Solartron SI 1287 analytical Potentiostat in DC setup. Open circuit potential (OCP) and PP experiments were configured and facilitated using Scribner's CorrWare application, then later processed and presented using CorrView. Prior to starting anodic polarisation, each specimen was immersed and tested in prepared solution for 30 minutes under open-circuit conditions (OCP). This is done to determine the potential between the WE (sample) and RE (SCE), under no external circuit load /E, whose positioning was as close to each other as possible to minimise voltage-drop in solution. Once each sample's OCP had been recorded, the software setup was then switched to polarisation mode.

Scan parameters for polarisation were set as follows; starting potential was selected as 0.3V below E recorded between WE and RE in preceding OCP measurement, with a scan rate of 1 mV/s. Scans were set to reverse polarity (i.e. anodic to cathodic sweep direction) once a current density of $0.005A.cm^{-1}$ was reached. These limits were taken as a follow-on from a previous iteration of this study completed by J. Bonfield for the sake of continuity between results[57]. Once samples had repassivated, i.e. after sweeps intersected their initial plots upon reversal, scans were promptly stopped and presented as E vs Log(I) plots.

Specimens were tested a minimum of 2 times each to ensure observed behaviour/features were reproducible and thus, accurately representative of alloy's performance characteristics.

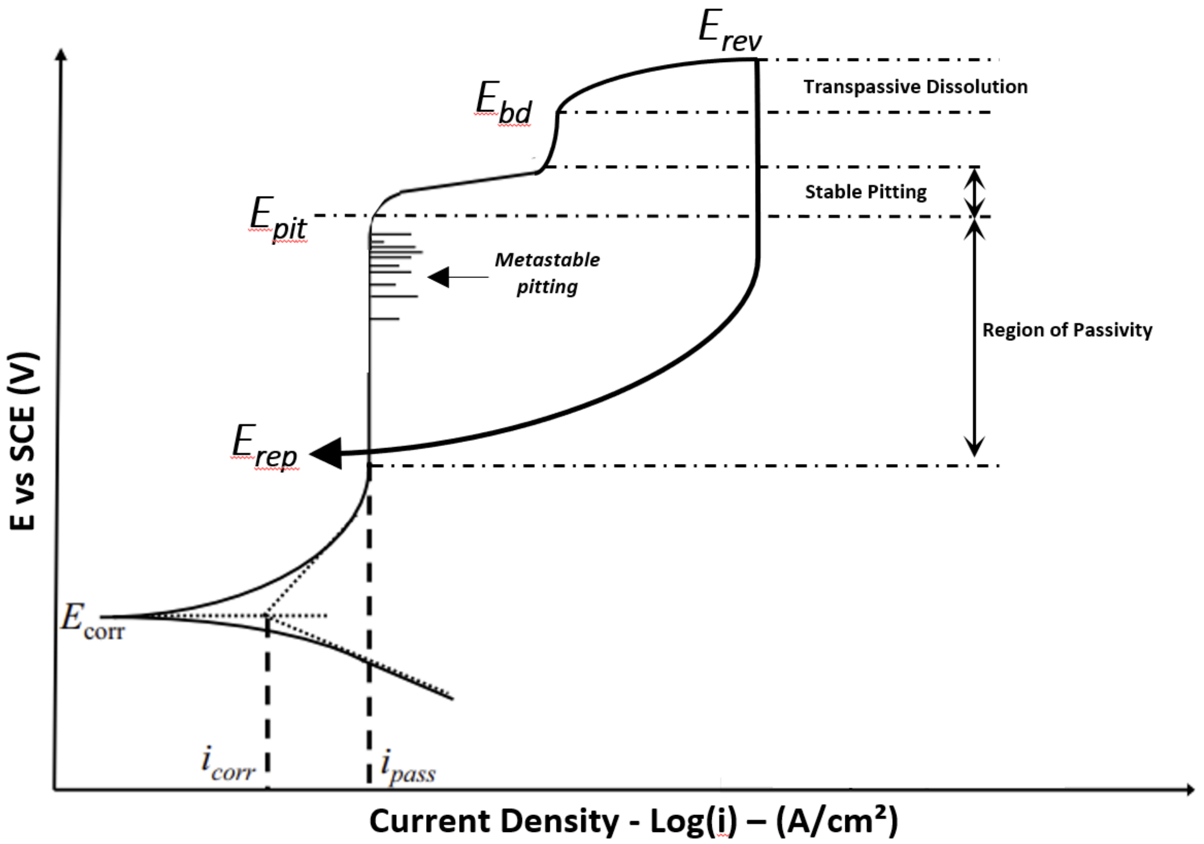

Figure 8: Schematic plot showing the characteristic shape of an anodic-going potentiodynamic polarisation plot with key events. Adapted for SDSSs from Nature-Scientific Data Article [58]

Figure 8 depicts the appearance of a hypothetically characteristic anodic-going potentiodynamic polarisation curve, specifically for metals with a high-degree of resistance to pitting corrosion immersed in NaCl solutions, as is the case with the subject alloys investigated in this study.

As SDSS are designed to be highly resistant to pitting corrosion compared to standard SS grades (i.e. high PREn), their polarisation scans can have additional artifacts correlating to various mechanisms across the stages of passive, active and transpassive behaviour.

Starting at E_{corr}, anodic and cathodic electrode reactions are in equilibrium. Following this, as the overpotential is increased the curve enters a period of active behaviour, indicated by the disproportionate increase in current density. However upon reaching the potential corresponding to i_{pass}, the current density stabilises and no longer increases with increasing overpotential. This is the point at which the protective oxide film is generated and signifies the onset of passive behaviour (active-passive transition). As the scan continues and the alloy reaches potentials closer to that of E_{pit}, the passive film begins to lose stability and metastable pits start to form – indicated by transients in current density displayed above. These pits often quickly subside due to the strongly-regenerative nature of SDSS passive films. However once E_{pit} is reached, the passive film is further destabilised by the overpotential and stable pitting begins to occur; indicated by a constant further sharp increase in current density. Although once again due to the high pitting-resistance of SDSSs, pitting is passivated briefly before reaching the value E_{bd}, at which point the once-passive metal exhibits transpassive behaviour.

Once E_{rev} is reached, the scan direction is reversed and current density rapidly decreases (transpassive dissolution slows down), due to the applied potential dropping back to values where passive layer elements are more stable and hence, combat further dissolution. Once the plot intersects with the initial scan line (i.e. near E_{rep} on plot), the alloy is considered to have repassivated, indicated by a significantly lower current density.

The plot above suitably represents the parameters of interest to be discussed later in the results section. Namely, the E_{pit}, E_{bd}, E_{rev} and E_{rep} values.

3.4. SVET

In-situ scanning vibrating electrode measurements on anodically polarised SDSS specimens were carried out using an SVET instrument of in-house construction whose design, mode of operation and calibration are described in detail elsewhere [1]. The instrument consisted of a probe comprising a 125 μm diameter platinum wire sealed in a glass sheath and this became the active portion of the probe tip. The probe was rastered over the surface of interest by means of a computer-controlled arrangement of stepper motors, allowing control of scan dimensions and probe-to-specimen distance. In this work, the SVET peak-to-peak voltage signal was converted to values of current density along the axis of probe vibration (j_z), by galvanostatically checking the calibration using a two-compartment cell as described previously [[56], [59]].

For SVET analysis of galvanostatically polarised SDSS specimens, the samples were prepared in a manner similar to that described previously for potentiodynamic polarisation experiments. Copper wire was connected to drilled specimens which were then cold mounted in two-part epoxy resin so that one of the circular faces of the medallion was exposed. This face was abraded using silicon carbide paper and polished using an aqueous slurry of 5 μm polishing alumina, washed with aqueous surfactant and rinsed with distilled water followed by ethanol. Test samples were then prepared by covering the surface with 90 μm thick extruded PTFE 5490 tape (3M Ltd), such that only a 5 × 5 mm square area was exposed to electrolyte. SDSS samples were completely immersed in an electrolyte bath containing aqueous 3.5 w% (0.6 mol L^{-1}) sodium chloride at pH 6.5. The electrolyte bath was left unstirred and in contact with room air at a nominal temperature of 20°C. The SVET probe was held vertically and scanned at a fixed height (100 μm) above the metal surface. For the experiments described here a constant anodic current density of 10 mA cm^{-2} was applied to the specimen by means of an in-house micro-galvanostat, employing a Pt gauze counter electrode. SVET scans were carried out immediately following the start of polarisation and at 8 min intervals thereafter for periods of up to 4 hours. A schematic diagram of the experimental set-up allowing in-situ SVET analysis under sustained anodic polarisation is shown in Figure 9 below.

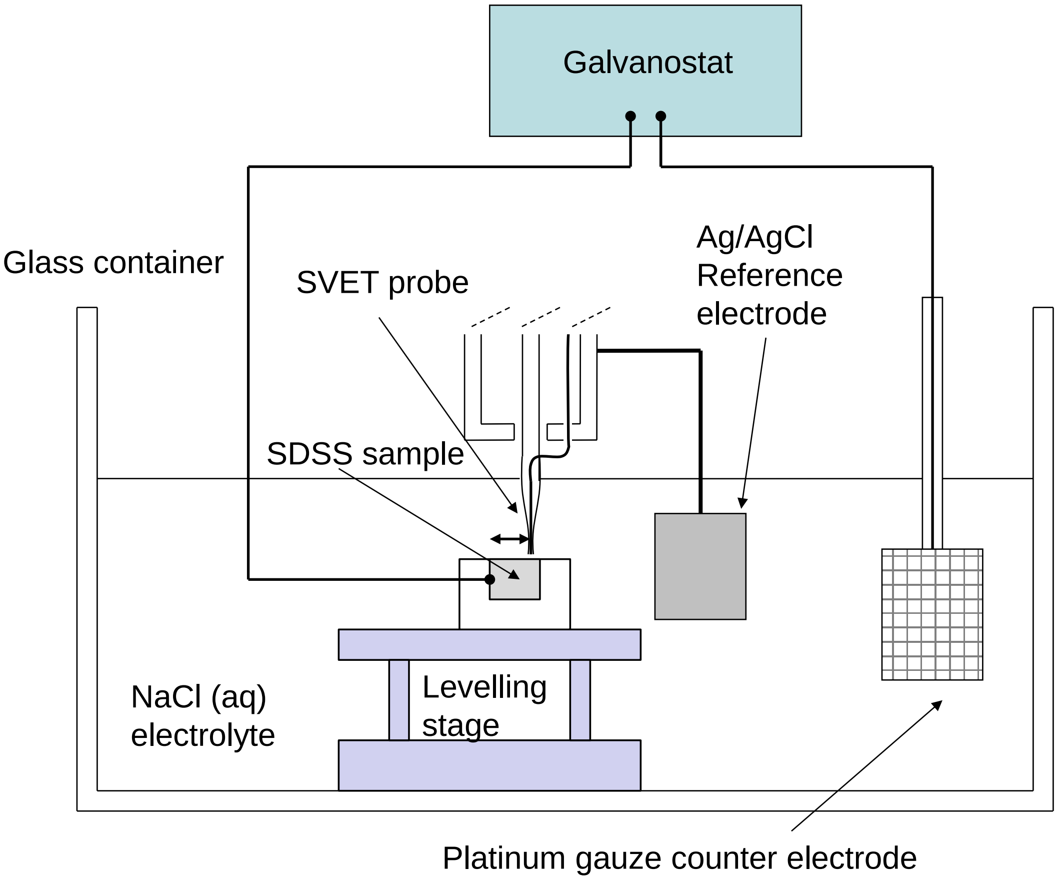

Figure 9: Schematic diagram showing the experimental set-up for SVET mapping of current density distributions over anodically polarised SDSS specimens immersed in corrosive test solution under galvanostatic control.

Important Note*: While it was within the initial scope and intention of this study to utilise the analytical method of SKPFM to evaluate local nobility-variances of the three alloys, regrettably lockdown measures hampered the ability to make use of facilities. It is my hope that further extensions of this work will make use of the data from this paper and the SKPFM technique to draw more substantial conclusions of alloy performance based on nobility readings as described in the "Further Work" section.*

3.5. Pourbaix Diagram for SDSS

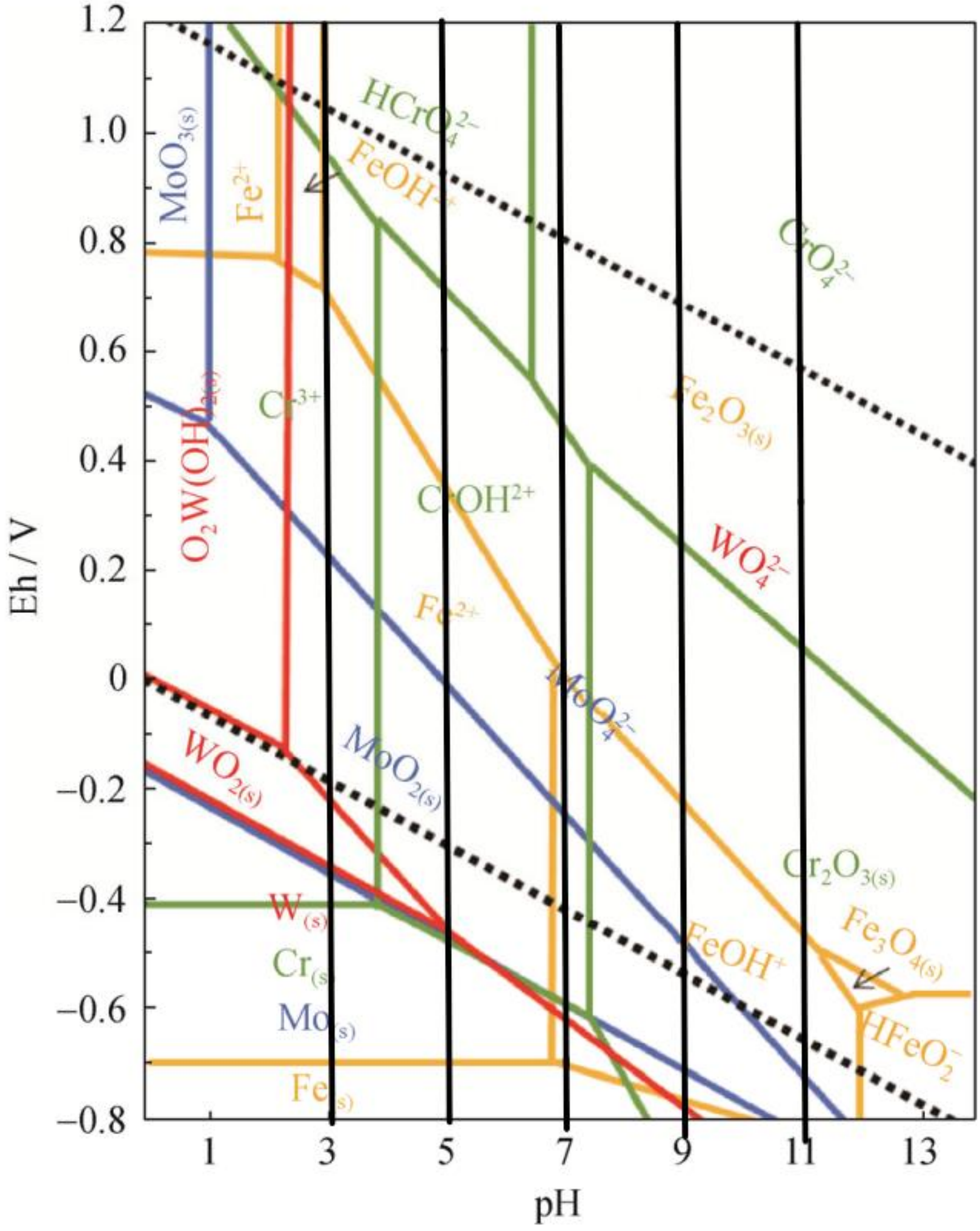

Figure 10: Pourbaix diagram for compounds formed in a 70wt%-Fe SDSS alloy as well as region of water stability (dotted) at 20°C – adapted from [60]

Figure 10 shows the thermodynamic stability of compounds formed by a SDSS system at various potentials and pHs. Throughout this study this figure will be referenced in an attempt to relate observed alloy corrosion behaviour with thermodynamic changes in stable elements represented by the various regions displayed in the diagram.

4. Results and Discussion

4.1. Optical Microscopy

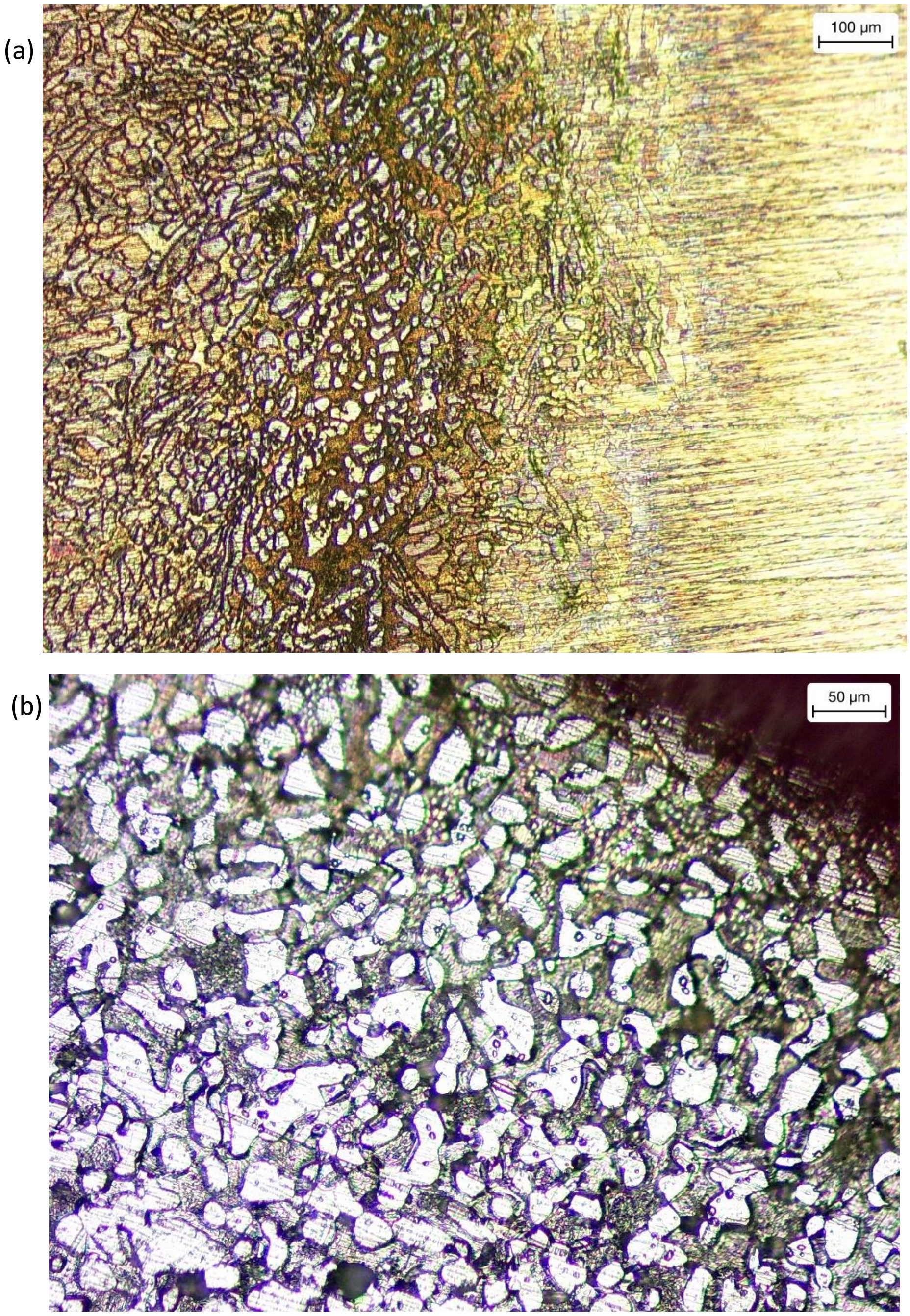

Figure 11: (a) 10x magnification optical micrograph scan of post-corroded ZER(W+) sample anodically polarised in 0.6M NaCl at a pH of 5 and (b) 20x mag micrograph of post-corroded FER(Cu+) specimen anodically polarised at a pH of 9

NB: *There was intention to obtain multiple micrographs across a number of pHs for each alloy, but as with SKPFM measurements, time & access restrictions imposed by the covid pandemic made acquisition unfeasible.*

4.1. Anodic-Potentiodynamic Polarisation in Aqueous Chloride Solution

Anodic polarisation sweeps were performed for each alloy in deoxygenated 0.6M NaCl(aq) (3.5wt %) solutions as a standard 3-electrode setup, with varying pH levels ranging from 3 to 11. These data plots are presented firstly as multi-pH/same alloy sweep compilations for each alloy in figures 12-14, then as multi-alloy/same-pH compilations in figures 15 to 19 and tables 3-7 respectively. Sweeps with extended reverse current density limits (0.1 A.m^{-2} compared to 0.05) for alloys FER(Cu+) and ZER(W+) are presented both individually and comparatively (FER vs ZER at 0.1A.m^{-2}) in figures 20-22. Summary plots of key corrosion-indicating parameters are shown in figures 23-25.

4.1.i PP - Multi-pH, same-alloy anodic sweep compilations

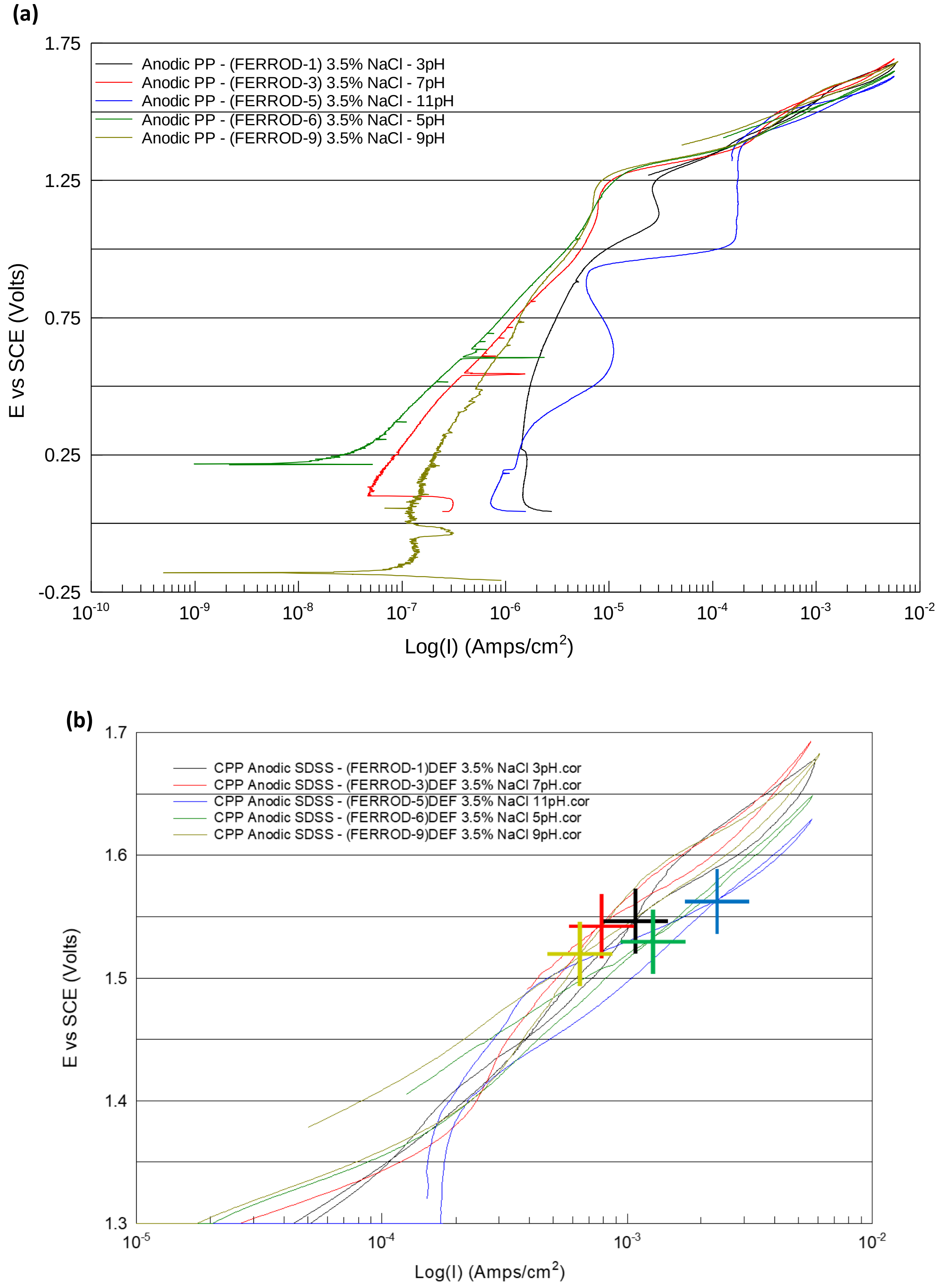

Figure 12 : (a) Anodic polarisation sweep compilation for alloy Ferralium 255 (FER(Cu+)) in NaCl(aq) at pH-3, pH-5, pH-7, pH-9 and pH-11 with (b) corresponding hysteresis loop compilation marked with repassivation points (+)

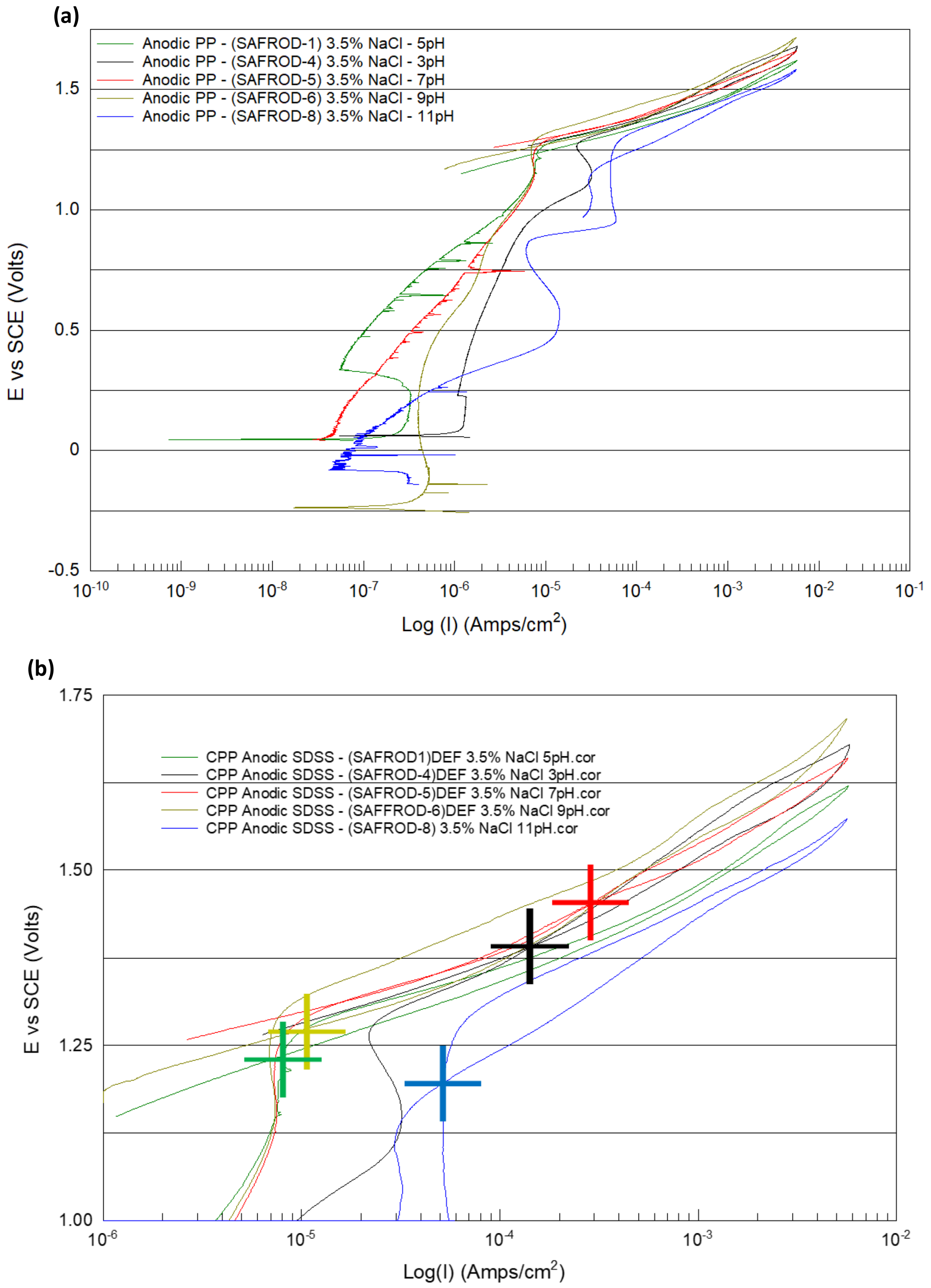

Figure 13: (a) Anodic polarisation sweep compilation for alloy SAF 2507 (SAF) in NaCl(aq) at pH-3, pH-5, pH-7, pH-9 and pH-11 with (b) corresponding hysteresis loop compilation marked with repassivation points (+)

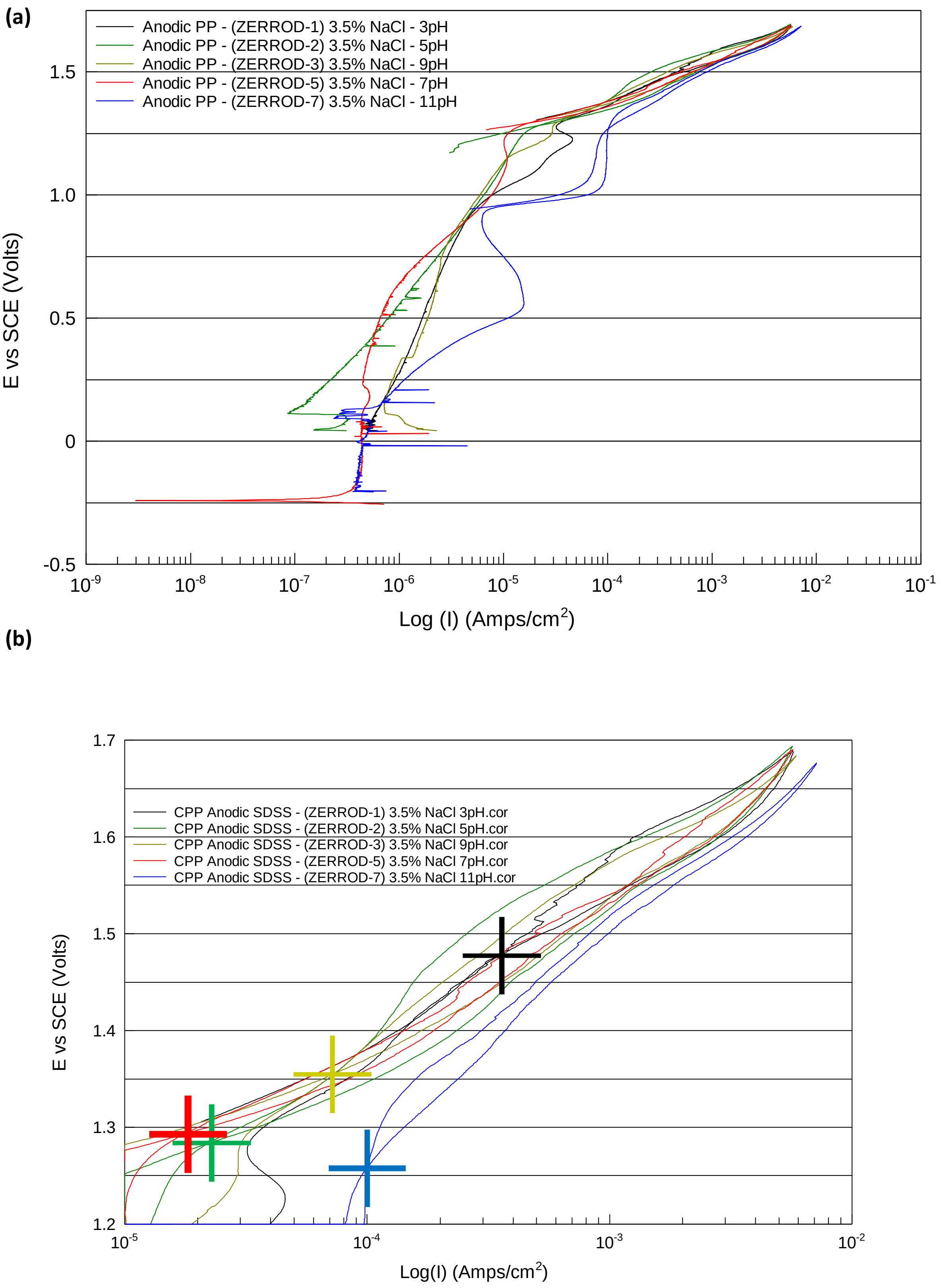

Figure 14: (a) Anodic polarisation sweep compilation for alloy Zeron 100 (ZER(W+)) in NaCl(aq) at pH-3, pH-5, pH-7, pH-9 and pH-11 with (b) corresponding hysteresis loop compilation marked with repassivation points (+)

4.1.ii PP - Same-pH, multi-alloy anodic sweep compilations

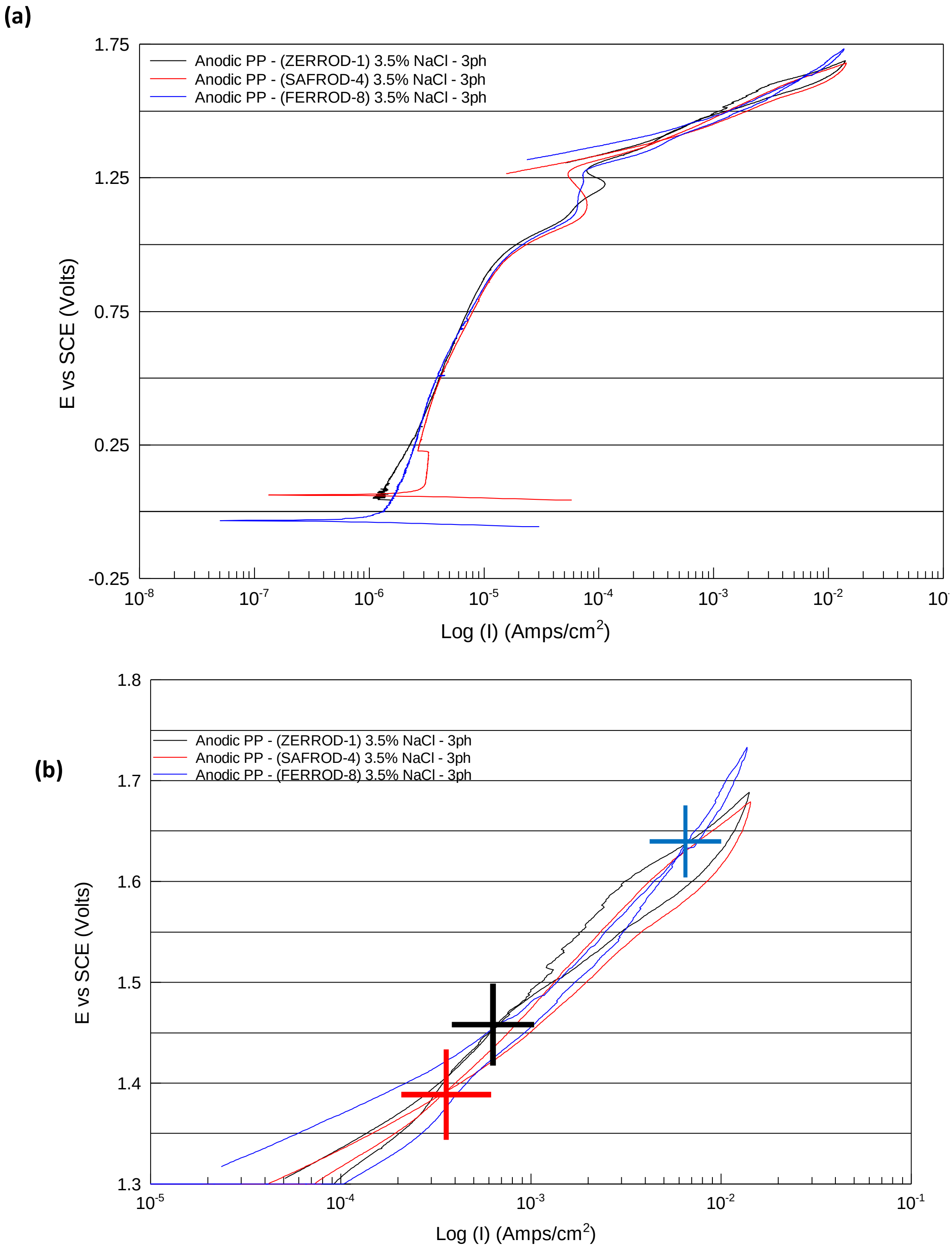

Figure 15: (a) Anodic polarisation sweep compilation for alloys ZER(W+), SAF and FER(Cu+) in NaCl(aq) at pH-3 with (b) enhanced view of associated hysteresis loops

Table 3: Table of key corrosion parameters measured for data presented in figure 15

Specimen	Solution pH	OCP (V vs SCE)	Breakdown Potential (E_{bd}/V vs SCE)	Repassivation Potential (E_{Rep}/V vs SCE)	Protective Potential Range (E_{Rep} – OCP) (V)	Reverse Potential (E_{Rev}/V vs SCE)
ZER(W+)	3	0.4337	1.2791	1.4767	1.043	1.6883
SAF	3	0.4388	1.2721	1.3909	0.9521	1.6791
FER(Cu+)	3	0.357	1.2708	1.6244	1.2674	1.7323

In acidic conditions of pH 3, all three alloys exhibited similar behaviour with a few distinctions in passive/transpassive transition. FER(Cu+), SAF and ZER(W+) all exhibited relatively stable passive regions with little signs of disruption or early pit-nucleation. FER (Cu+) showed rapid transition from the anodic peak (E_{corr}) into the passive region, whilst SAF exhibited a brief transient in anodic activity prior to primary passivation. As a result of the scan start-point being above that of the E_{corr} for ZER(W+), it could not be concluded whether or not it underwent primary passivation. All three alloys also showed a progressive increase in current density with higher potentials along the passive region, this can most likely be attributed to oxygen evolution being thermodynamically feasible at this potential range[60].

All three alloys yet again showed similar transpassive sweep-dynamics, with their breakdown potentials (E_{bd}) being in the range of 0.921 – 0.937$V_{vs\ SCE}$. Post -breakdown, FER(Cu+) showed signs of brief yet rapid repassivation as its plot stabilises (i.e. straightens up) before subsequently reaching the pitting breakdown potential (E_{pit}) at 1.27 $V_{vs\ SCE}$. SAF and ZER(W+) also showed signs of brief repassivation but inevitably reached the same breakdown point (1.27V) before being able to meanigfully repassivate. Upon reversal of the scanning direction, FER(Cu+) was the first to rapidly repassivate at 1.62$V_{vs\ SCE}$ showing little signs of pitting activity, soon followed by SAF and ZER(W+) at potentials of 1.39 and 1.48$V_{vs\ SCE}$ respectively. This is indicated in fig 15(a) by the coloured crosses which correspond to the colours indicated on sweep legend.

With regards to pitting, both shape and size of the hysteresis loops for all three alloys differ at 3pH, with ZER(W+) having the largest and widest loop followed by SAF and finally, FER(Cu+) with the smallest and narrowest. FER(Cu+)'s minimal hysteresis loop coupled with its lower OCP and high repassivation potential of 1.62$V_{vs\ SCE}$ indicates its superior repassivation performance in Cl-containing media at low pH compared to W-containing and non-W/low Cu-containing alloys. This could be explained by the well noted tendency of copper-containing stainless steels to be especially resistant to pitting in chloride-containing environments[42], [44].

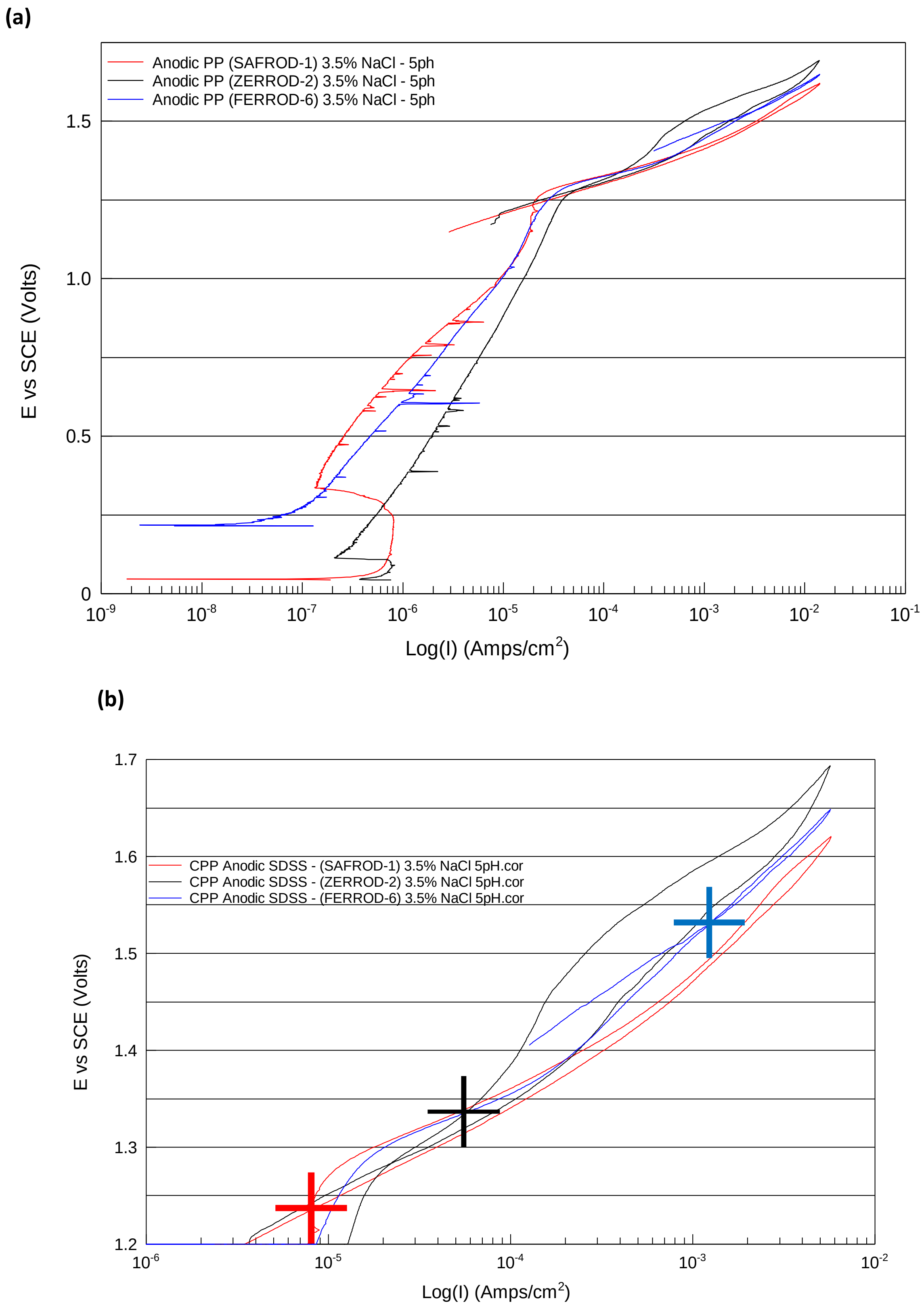

Figure 16: (a) Anodic polarisation sweep compilation for alloys ZER(W+), SAF and FER(Cu+) in NaCl(aq) at pH-5 with (b) enhanced view of associated hysteresis loops

Table 4: Table of key corrosion parameters measured for data presented in figure 16

Specimen	Solution pH	OCP (V vs SCE)	Breakdown Potential (E_{bd}/V vs SCE)	Repassivation Potential (E_{Rep}/V vs SCE)	Protective Potential Range (E_{Rep} – OCP) (V)	Reverse Potential (E_{Rev}/V vs SCE)
ZER(W+)	5	0.1981	1.2541	1.2842	1.0861	1.6936
SAF	5	0.2618	1.2523	1.2346	0.9728	1.6204
FER(Cu+)	5	0.2324	1.2485	1.5334	1.301	1.6486

At pH 5 distinctions in passive behaviour between the three alloys became more pronounced through earlier phases of the sweep. ZER(W+) and SAF showed similar OCPs at 0.23V and 0.26$V_{vs\ SCE}$ respectively, contrasted with FER(Cu+)'s notably higher OCP of 0.19$V_{vs\ SCE}$ – indicating slightly better stability of ZER and SAF alloys in 5pH chloride solution. Subsequently, SAF appeared to show a significant yet brief spike/transient of anodic activity before reaching passive potentials of ~0.33$V_{vs\ SCE}$, likewise to ZER(W+); showing a lesser degree of primary passivation up to 0.125$V_{vs\ SCE}$. This would indicate SAF had more difficulty with primary passivation as opposed to ZER(W+) at this pH, which passivated within 1/3 of the potential range used by SAF. FER(Cu+)'s plot had no sign of defined primary passivation at the start, although it is entirely plausible its curve was cut off due to insufficiently high sweep-starting potential.

Nevertheless all three alloys exhibited well-defined regions of passivity across similar ranges of potential (~ 0.25 – 1.25 $V_{vs\ SCE}$). In spite of this, there are a number of artifacts which inferred difference in alloys' stabilities within the passive region. Initially, all three alloys showed different passive current densities (i_p), which has been stated to indicate different rates of corrosion[61], with higher i-densities correlating to faster rates. Contrary to its apparent difficulty with initial passivation, SAF showed the lowest i_p, quickly followed by FER(Cu+) and lastly ZER(W+). In spite of this, transient current-spikes in the passive regions of all three alloys told a different story of stability. All three alloys appeared to show increased frequency & severity of transients around ~0.6V, SAF and FER(Cu+) both displayed their large transients around this point, whereas ZER(W+) did not display spiking to the same degree. With similar sentiment to its difficulty in initial passivation, SAF showed a large degree of current transients specifically in more noble potentials of the passive region, 0.57V to 0.87$V_{vs\ SCE}$. This was also the case for FER(Cu+), although it also showed earlier signs of transients at less noble potentials as low as 0.3V, up to 0.69$V_{vs\ SCE}$. As for ZER(W+), despite displaying the highest apparent corrosion rate through its higher passive current densities, it also exhibits the least amount of current transients in a less-noble and narrower potential range of 0.38V to 0.62V. Interestingly, unlike ZER(W+), both SAF and FER(Cu+) alloys show on average more sever instances of transient metastable pitting, most notably at potentials of 0.64V and 0.6 $V_{vs\ SCE}$ respectively. This could be explained when referring to the pourbaix diagram indicating the thermodynamic stability of the compound Tungstate (WO_4^{2-}) at this range (ref. fig 10). It could be the case that tungstate in the PL of ZER(W+) acts to impede the evolution of oxygen reaction, thus suppressing the anodic current observed in the passive region. However, to validate this idea in-situ compositional analysis would be needed to determine the specific reactions and resultant compounds in this situation.

Approaching the breakdown point SAF displayed a brief attempt to repassivate at 1.15$V_{vs\ SCE}$, which was not observed in the FER(Cu+) and ZER(W+) specimens. Aside from this feature, all three alloys displayed similar breakdown dynamics, with all three having breakdown/pitting potentials (E_{bd}/E_{pit}) of around 1.25 $V_{vs\ SCE}$. As with results acquired at a pH of 3, FER(Cu+) again displayed the smallest and narrowest hysteresis loop in a chloride environment at 5pH, evidenced by its rapid repassivation at a potential of 1.53$V_{vs\ SCE}$ and thus, indicative of less pitting corrosion damage. This idea is corroborated by general consensus of copper's usefulness for increasing pitting corrosion resistance in chloride-containing environments via formation of insoluble oxides in the passive layer[62]. SAF and ZER(W+) both possessed larger hysteresis loops albeit with different geometries, ZER(W+) displayed a significantly-thicker hysteresis loop in comparison to SAF's slender loop, indicating a greater degree of dissolution severity in the former. ZER(W+) and SAF repassivated at 1.28V and 1.23 $V_{vs\ SCE}$ respectively. This occurred at much lower potentials than their reverse potentials and closer to their original breakdown points, unlike FER(Cu+) which repassivated at a potential much higher than that of its initial E_{bd}/E_{pit}.

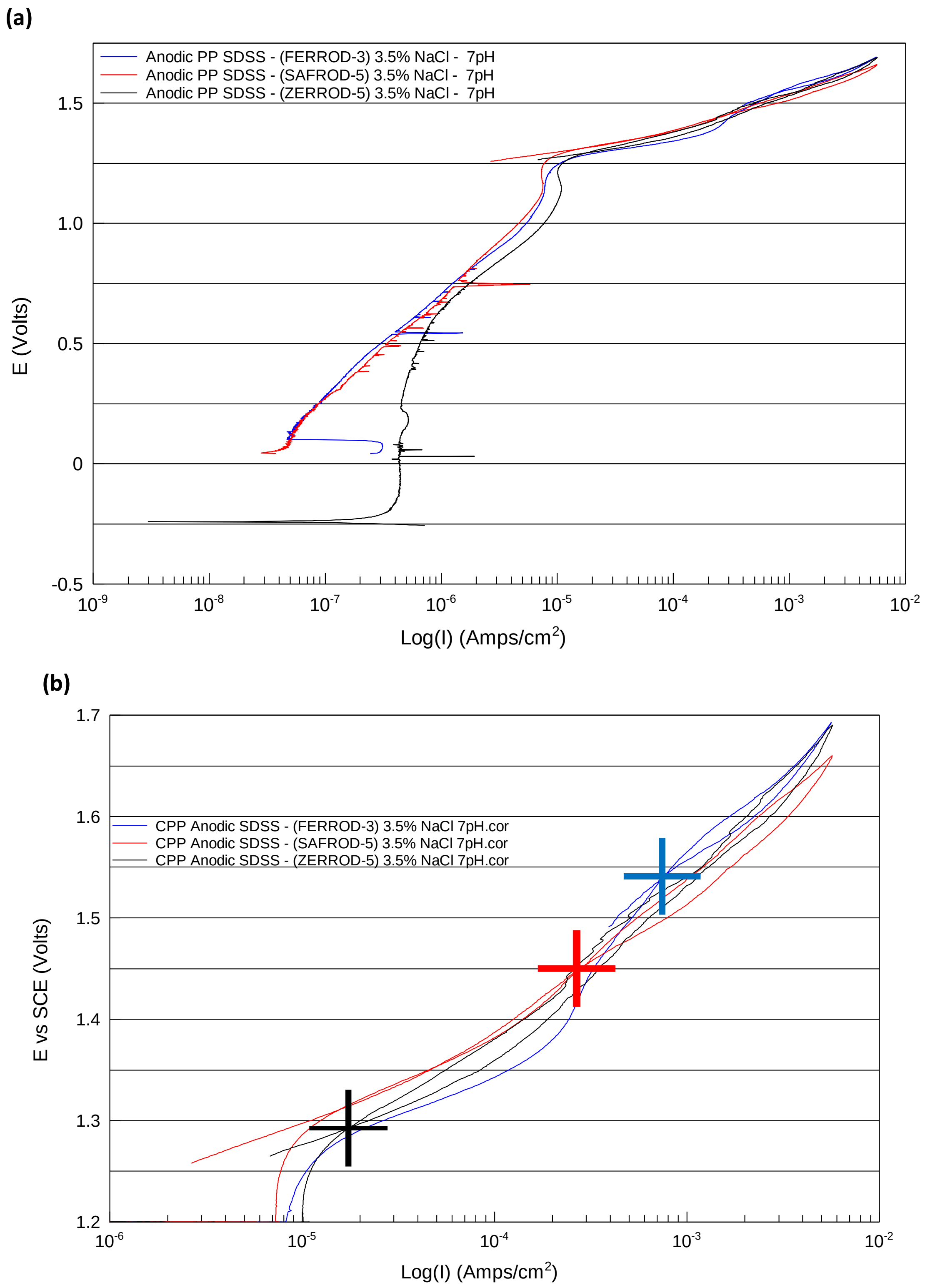

Figure 17: (a) Anodic polarisation sweep compilation for alloys ZER(W+), SAF and FER(Cu+) in NaCl(aq) at pH-7 with (b) enhanced view of associated hysteresis loops

Table 5: Table of key corrosion parameters measured for data presented in figure 17

Specimen	Solution pH	OCP (V vs SCE)	Breakdown Potential (E_{bd}/V vs SCE)	Repassivation Potential (E_{Rep}/V vs SCE)	Protective Potential Range (E_{Rep} – OCP) (V)	Reverse Potential (E_{Rev}/V vs SCE)
ZER(W+)	7	0.1428	1.2326	1.2949	1.1521	1.69
SAF	7	0.13914	1.2454	1.4536	1.31446	1.6602
FER(Cu+)	7	0.1101	1.2467	1.5431	1.433	1.6927

In neutral conditions (7pH), following intermediate potentials of around $0.6V_{vs\ SCE}$, alloys showed high degrees of characteristic conformance in breakdown and repassivation behaviour[57], [63], [64]. ZER(W+) presented a comparatively greater range of passivity at 7pH of about 0.19V, albeit at the expense of a less-noble OCP of $0.24V_{vs\ SCE}$. Although partially obscured, SAF and FER(Cu+) both possessed OCPs in the more noble direction of potentials at approximately 0.04V, with FER(Cu+)'s taken just prior to the anodic peak of primary passivation and SAF's at the end of what appears to be PP.

Compared to previous sweeps at 3- and 5 pH, for SAF and FER(Cu+) particularly, the slope of the region of passivity was noticeably flatter (less steep), indicating a more active passive current density. More notably, ZER(W+) appeared to be the only alloy at pH-7 to show a clear transition from passive to transpassive behaviour (~$0.55V_{vs\ SCE}$). SAF and FER(Cu+) on the other hand, displayed a consistent slope of activity following PP up until the point of breakdown. It is difficult to postulate what particularly causes this difference in behaviour without chemical/in-situ analysis of the alloys in these conditions. However as with the reasoning of the current transients at 5pH this could be due to presence of tungstate, which in these conditions could be reduced at cathodic sites to form the protective-compound tungsten oxide (WO_3), this reaction would likely be observed as $WO_4^{2-} + 2H_2O \text{ -> } WO_2 + 4OH$. Alternatively, previous study has stated the tendency of tungstate to also act as a oxidising agent to released iron ions (Fe^{2+}) at anodic sites within high E-ranges to form passive iron tungstate (Fe_2WO_6) complexes[65]. In either such case, W would pose a significant benefit to passivity of SDSS immersed in neutral/acidic chloride media within this potential range compared to that of non W- and Cu-containing alloys.

Whilst ZER(W+) exhibited stronger passive tendencies at the earlier potentials, it does so with the highest current density (i_{pass}) among the three. This is up until a potential of about 0.6$V_{\text{vs SCE}}$, at which point it's sweep became concurrent with that of SAF and FER(Cu+)'s, indicating the onset of the oxygen evolution reaction (ref pourbaix fig 10). As with data obtained at a pH of 5, alloys again possess a number of current transients most significantly at intermediate potentials of the passive range ~ 0.4 to 0.81$V_{\text{vs SCE}}$. SAF appears to be most afflicted with transients repeatedly occurring in this potential range, followed by FER(Cu+) with less frequent & significant (low-*i*) transients. Lastly, as before ZER(W+) displayed current transients of lesser frequency and severity. SAF and FER(Cu+) both undergo single occasions of large current transients at 0.74V and 0.54$V_{\text{vs SCE}}$ respectively.

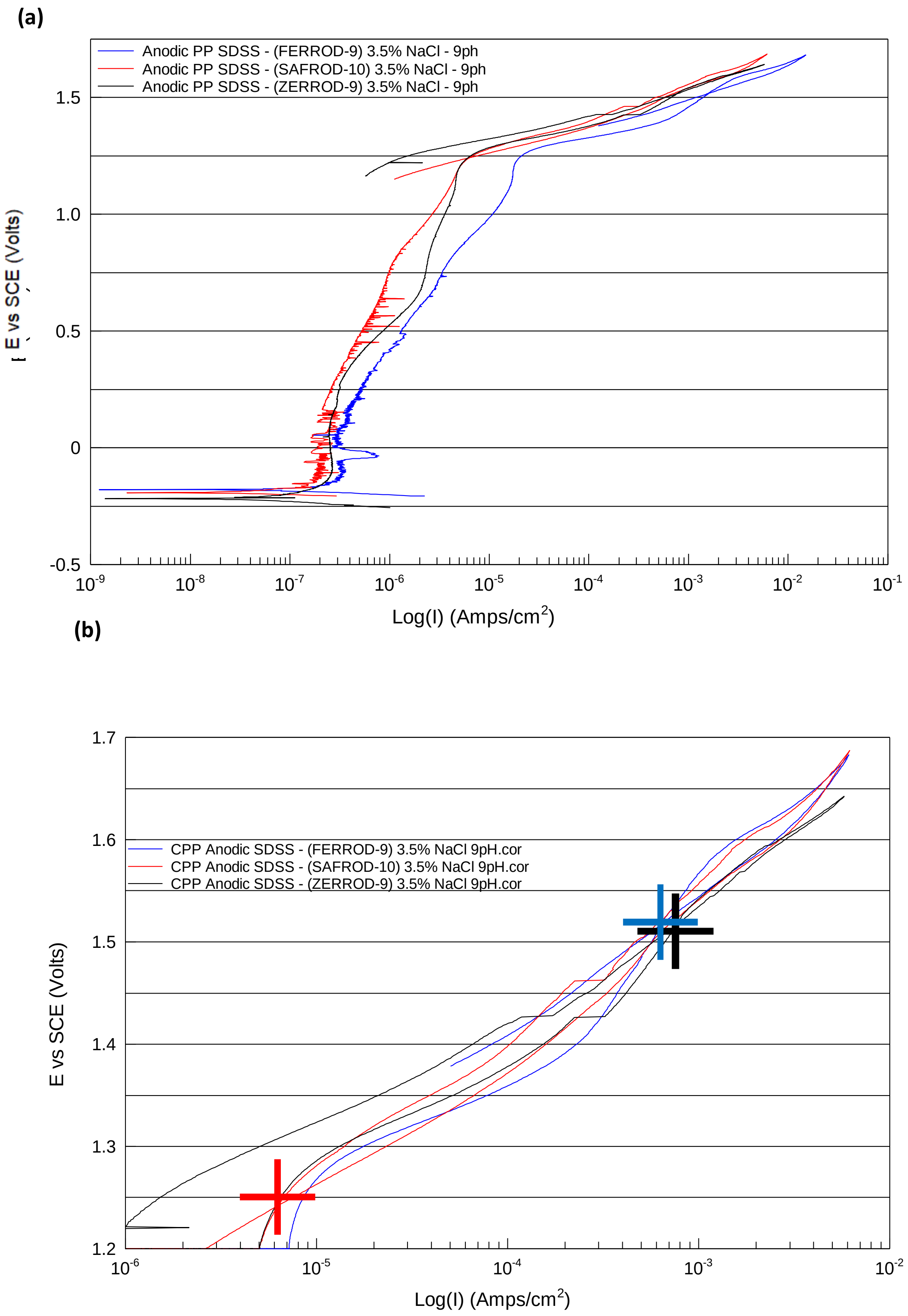

Figure 18: (a) Anodic polarisation sweep compilation for alloys ZER(W+), SAF and FER(Cu+) in NaCl(aq) at pH-9 with (b) enhanced view of associated hysteresis loops

Table 6: Table of key corrosion parameters measured for data presented in figure 18

Specimen	Solution pH	OCP (V vs SCE)	Breakdown Potential (E_{bd}/V vs SCE)	Repassivation Potential (E_{Rep}/V vs SCE)	Protective Potential Range (E_{Rep} – OCP) (V)	Reverse Potential (E_{Rev}/V vs SCE)
ZER(W+)	9	-0.2171	1.2271	1.5158	1.7329	1.642
SAF	9	-0.1924	1.2181	1.2445	1.4369	1.6873
FER(Cu+)	9	-0.1791	1.2218	1.5187	1.6978	1.6822

In this alkaline solution (pH 9), FER(Cu+), SAF and ZER(W+)'s OCP's were well defined with minimal difference between the three alloys at -0.18, -0.19 and -0.22$V_{vs\ SCE}$ respectively, slightly less-noble potentials in comparison with acidic pH's.

Instability in the preliminary stage of the passive region was evident particularly for FER(Cu+) and SAF alloys. Both displayed signs of ongoing activity/noise following prompt passivation after the OCP, extending all the way past the middle of the region of passivity (~ -0.15V to 0.7$V_{vs\ SCE}$). FER(Cu+) appeared to undergo some metastable pitting at -0.03$V_{vs\ SCE}$ but quickly repassivated, whilst SAF showed no distinct signs of metastable pitting until later potentials around 0.45V to 0.64$V_{vs\ SCE}$. ZER(W+) on the other hand, displayed no signs of metastable pitting or noise within the region of passivity up until the breakdown potential (E_{bd}/E_{pit}).

In comparison to the passive regions observed in acidic (pH 3/5) and neutral (pH 7) chloride media, alkaline conditions of pH-9 appeared to impair stability of the passive film, particularly at higher potentials. This is indicated by the non-linear/discontinuous nature of all three alloy's passive regions when compared to lower-pH sweeps. With exception of the early-stage artefacts present on SAF and FER(Cu+)'s sweeps, all three alloys appear to show relatively consistent passive layer conditions after the OCP up until around 0.25$V_{vs\ SCE}$. After which, current densities visibly increase with increasing potential. This could potentially be explained by referring to the pourbaix diagram presented from a previous study in figure 10 [60]. The plot shows that for potentials reaching 0.25$V_{vs\ SHE}$ (~0.5$V_{vs\ SCE}$) in 9pH chloride media, the Cr^{6+} species chromate (CrO_4^{2-}) becomes more thermodynamically stable than the protective/stabilising chromium oxide (III) (Cr_2O_3) element. Such a change in PL chemical formulation would explain a marked decrease in film stability, due to the facilitation of ion ingress consequential with the formation of soluble Cr^{6+} species[26].

With regards to breakdown, SAF and ZER(W+) reached their breakdown points at the same potential around 1.2$V_{vs\ SCE}$, likewise to FER(Cu+), albeit at a notably higher current density (i_{bd}). As with previous breakdown potentials presented, these values are in agreeance with previously reported potentials in similar studies. Interestingly, unlike with previous sweep compilations, hysteresis data obtained in 9-pH conditions showed ZER(W+) underwent the least amount of pitting damage as opposed to FER(Cu+). This is evidenced by ZER(W+)'s narrow and short-ranged hysteresis region compared to the noticeably thicker and much wider hysteresis loops of FER(Cu+) and SAF respectively. Both FER(Cu+) and ZER(W+) then repassivated shortly after the reverse potential at 1.51$V_{vs\ SCE}$, followed by SAF at a much lower 1.24$V_{vs\ SCE}$. This may infer that whilst W and Cu additions appear to increase the passive current density of SDSS's in alkaline chloride media, they also serve to inhibit pitting corrosion damage at more noble potentials compared to normal SDSSs, hence the difference in repassivation potentials observed.

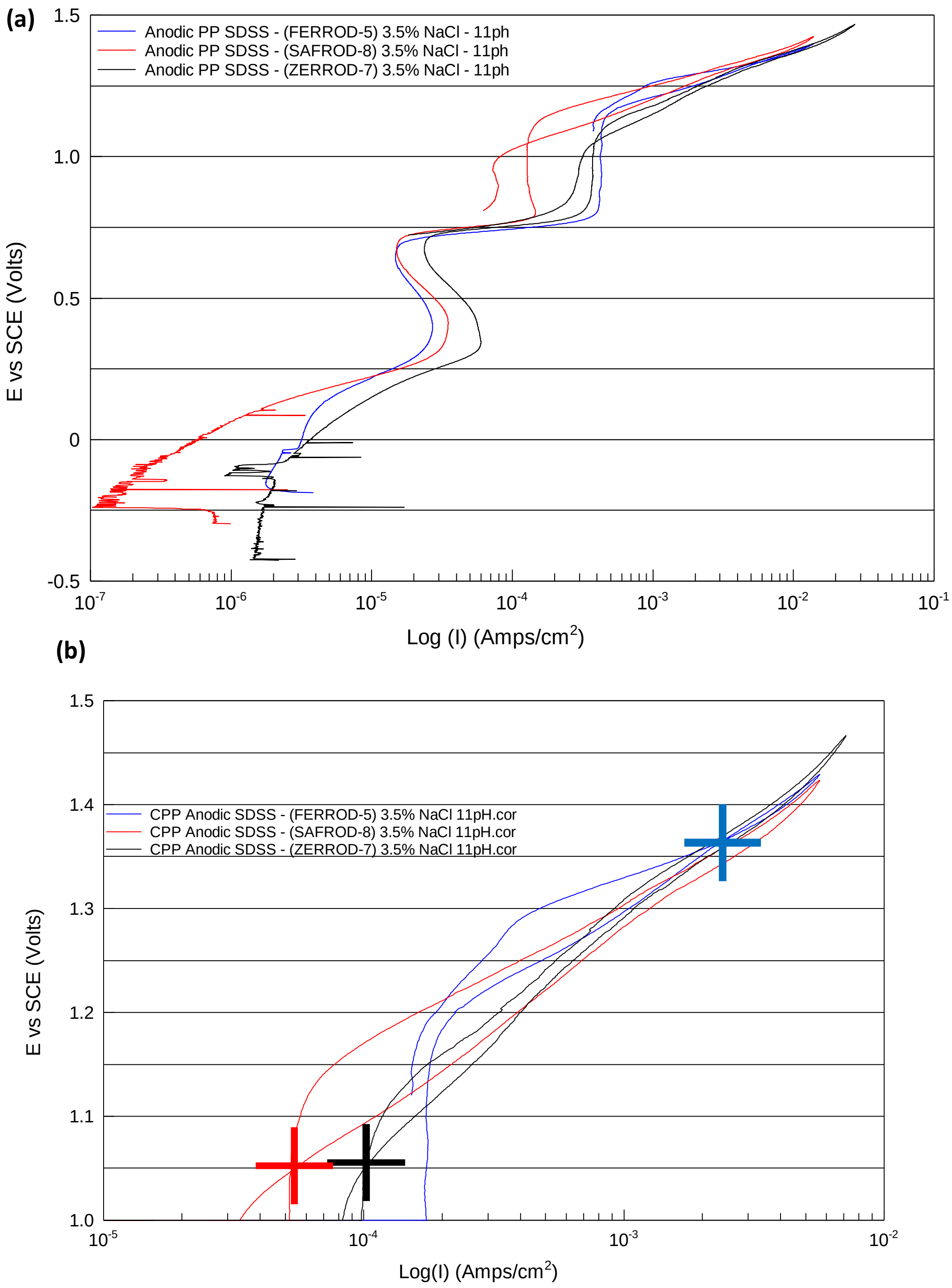

Figure 19: (a) Anodic polarisation sweep compilation for alloys ZER(W+), SAF and FER(Cu+) in NaCl(aq) at pH-11 with (b) enhanced view of associated hysteresis loops

Table 7: Table of key corrosion parameters measured for data presented in figure 19

Specimen	Solution pH	OCP (V vs SCE)	Breakdown Potential (E_{bd}/V vs SCE)	Repassivation Potential (E_{Rep}/V vs SCE)	Protective Potential Range (E_{Rep} – OCP) (V)	Reverse Potential (E_{Rev}/V vs SCE)
ZER(W+)	11	-0.1389	1.1032	1.0505	1.1894	1.4666
SAF	11	-0.0374	1.1325	1.0476	1.085	1.4238
FER(Cu+)	11	-0.1781	1.3699	1.5653	1.7434	1.6292

Electrochemical behaviour of the SDSS alloys in chloride media at a pH of 11 was charaterised mainly by transpassive dissolution dominating the region of passivity. Alloy sweeps started with scattered OCP's, with FER(Cu+) being the most noble at -0.15$V_{vs\ SCE}$ and ZER(W+) the most anodic on the other end at -0.42$V_{vs\ SCE}$. This being said, scanning parameters for sweeps at 11pH are likely to have missed the brief period of primary passivation subsequent to E_{corr}, possibly due to software error with 11pH sweeps being performed shortly after testing in acidic conditions. In the early stages of the passive region, ZER(W+) showed the most stable passive behaviour with a relatively vertical scan, allbeit with occasional current transients, up until around 0$V_{vs\ SCE}$. At more noble potentials, FER(Cu+) also showed a notable effort to remain passive between potentials of -0.12V to 0.1$V_{vs\ SCE}$, despite undergoing it's own instance of current transients at -0.01$V_{vs\ SCE}$. Whilst it showed a less well-defined region of passivity, prior to potentials up to ~ 0.12$V_{vs\ SCE}$ SAF displayed significantly lower passive current densities (i_{pass}). Coupled with the observation of it's lower i_{pass} at a pH of 9 also, such results could indicate a lower corrosion rate for W and Cu-free specimens in highly alkaline chloride conditions.

The brief regions of passivity shown by all alloys was quickly followed by the onset of what can most likely be identified as transpassive breakdown, evidenced by the significant increase in current density experienced by all three alloys post-0.1$V_{vs\ SCE}$. As with the set of results at 9pH, this can at least partially be attributed to the absence of the PL-stabilising Chromium Oxide (III)/($Cr_2O_{3(s)}$) ellement, thermodynamically replaced with chromate (CrO_4^{2-}). This leads to weakening of the passive layer and hence increases the observed corrosion current density. All three specimens then promptly repassivated reaching potentials of around 0.3V and appear to continue repassivation until a second concurrent current-transient occurred at 0.7$V_{vs\ SCE}$. This spike in current is far steeper than the first seen at lower potentials, with added consideration of its occurrence at the upper-limit of the region of water stability on the Pourbaix diagram, it's likely this feature of the sweep was facilitated by the evolution of oxygen reaction.

At ~0.8$V_{vs\ SCE}$ alloys promptly repassivated and exhibited brief yet distinct periods of strongly passive behaviour up until the pitting potential of ~1.1$V_{vs\ SCE}$. As observed at the start of the 11pH scan, SAF yet again showed the lowest current density at the point of pitting breakdown (i_{pit}) – 0.05mA followed by ZER(W+) with 0.10mA and lastly FER(Cu+) with 0.18mA. SAF and ZER(W+) breakdown at similar pitting potentials of 1.07V and 1.06$V_{vs\ SCE}$ respectively, whilst FER(Cu+) saw the onset of pitting at a more noble potential of 1.18V. In accordance with trends highlighted in previous sweeps with exception of the 9-pH data set, FER(Cu+) again displayed the smallest hysteresis loop indicating superior pitting resistance in high-pH conditions. In contrast, SAF appears to show the greatest degree of pitting (largest hysteresis loop) followed by ZER(W+). Unsurprisingly, FER(Cu+)'s small hysteresis loop was coupled with a comparatively highly-noble repassivation potential of 1.36$V_{vs\ SCE}$, followed by SAF and ZER(W+) simultaneously at around 1.04V.

4.1.iii PP – Effect of higher reverse current density limit (i_{rev}) comparison – FER(Cu+) / ZER(W+)

In addition to the anodic polarisation scan presented thus far, FER(Cu+) and ZER(W+) alloys were also subjected to polarisation scans with larger reverse potentials (E_{rev}) imposed. This was done to ascertain whether dissolution behaviour following transpassive breakdown would develop differently at more active potentials between the two Cu- and W-alloyed specimens. The results are presented below in figures 20 to 22.

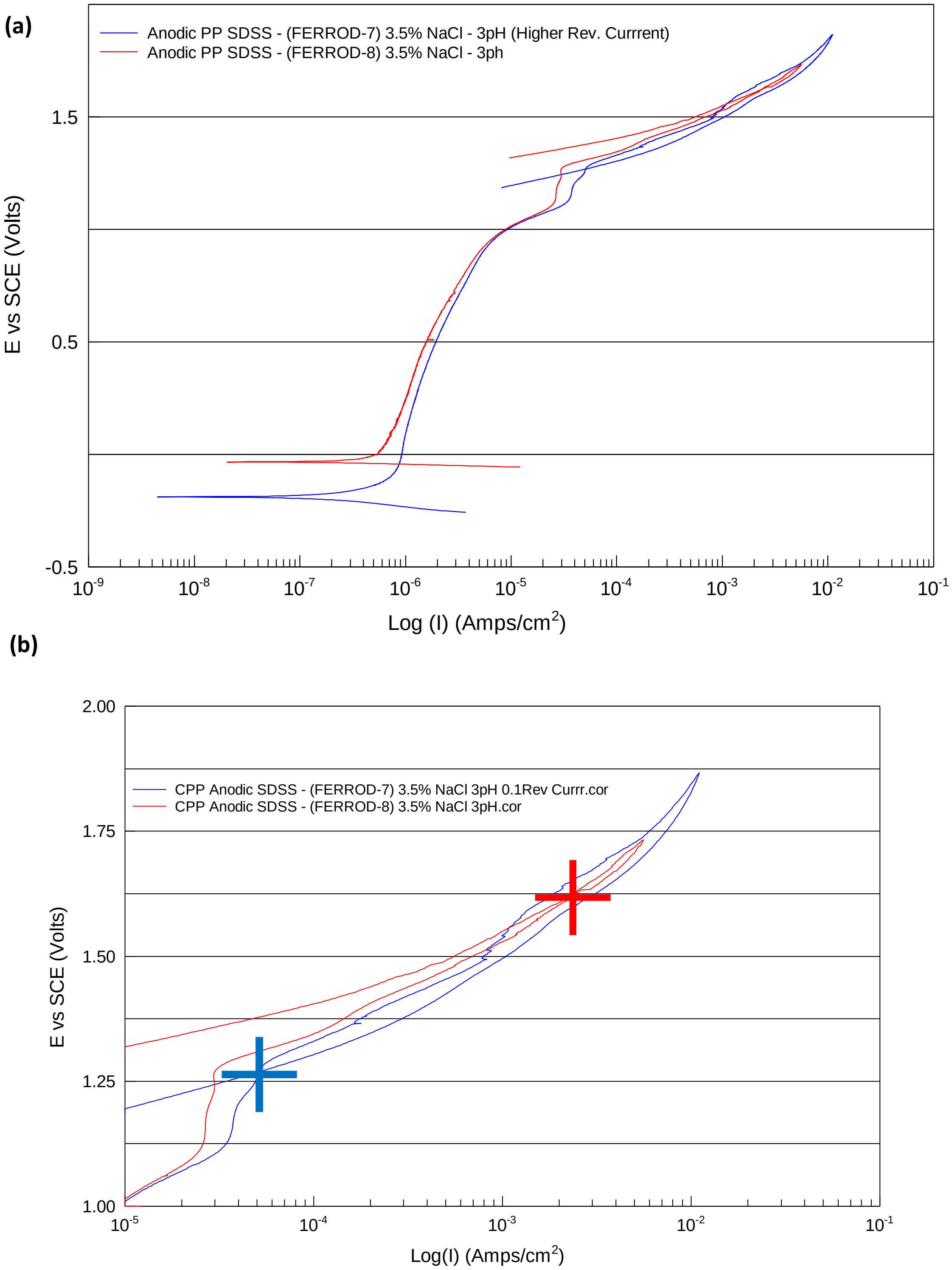

Figure 20: (a) Anodic potentiodynamic polarisation sweep for FER(Cu+) with an i_{rev} of 0.05 vs 0.1 A.cm^{-2}, with (b) enhanced view of associated hysteresis loops - tested in deoxygenated 0.6M NaCl at a pH of 3

Both curves showed well-defined regions of active, passive and transpassive behaviour generally. Distinctions in performance between the two samples was revealed upon the reversal of scan direction/polarity. It was apparent that increasing the reverse current density limit from 0.05 to 0.1 A.cm^{-2} resulted in a much lower repassivation potential of 1.2V$_{vs\ SCE}$, compared to a more noble 1.62V for FER(Cu+) (*low* i_{rev}). FER(Cu+) (*high* i_{rev}) developed a more extensive hysteresis loop than with a lower reverse current. Considering the visibly greater degree of pitting on its surface post-testing, it can be inferred that higher i_{rev} leads to sustained dissolution activity in acidic species, likely due to more severe/ penetrative pitting impeding repassivation efforts upon scan reversal. As expected, higher reverse current density limits imposed on polarisation scans did not affect any pre-breakdown features or events within sweeps.

(a)

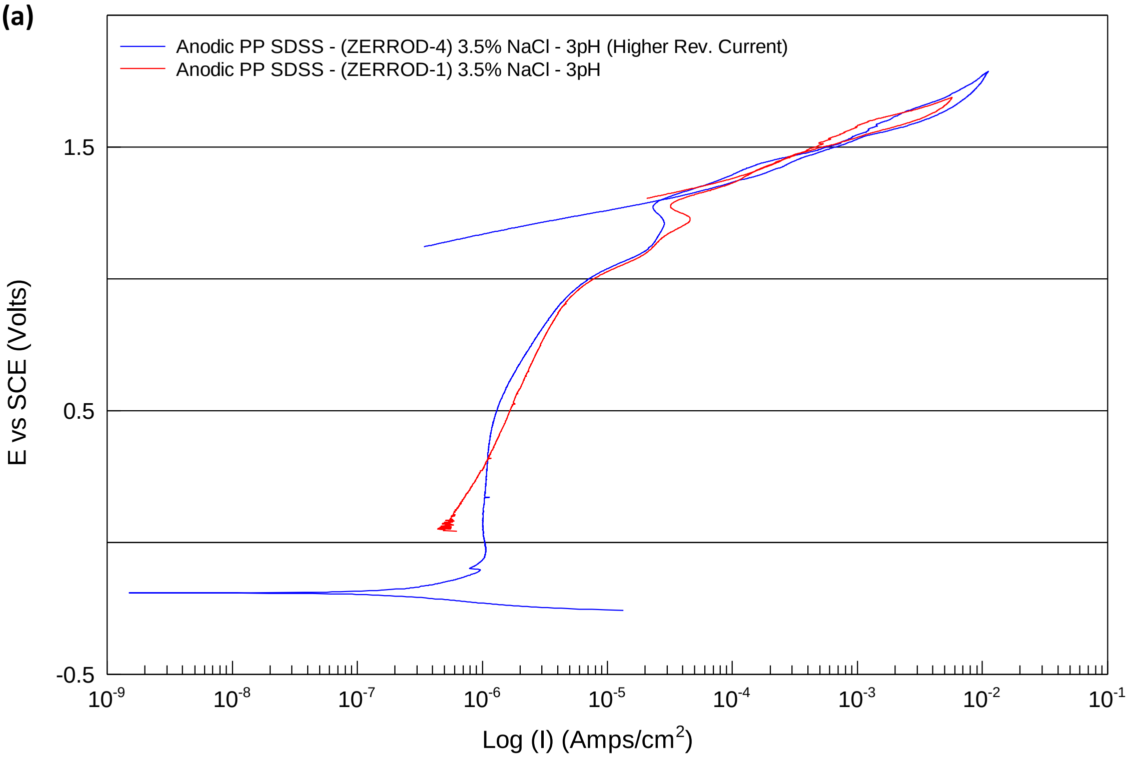

(b)

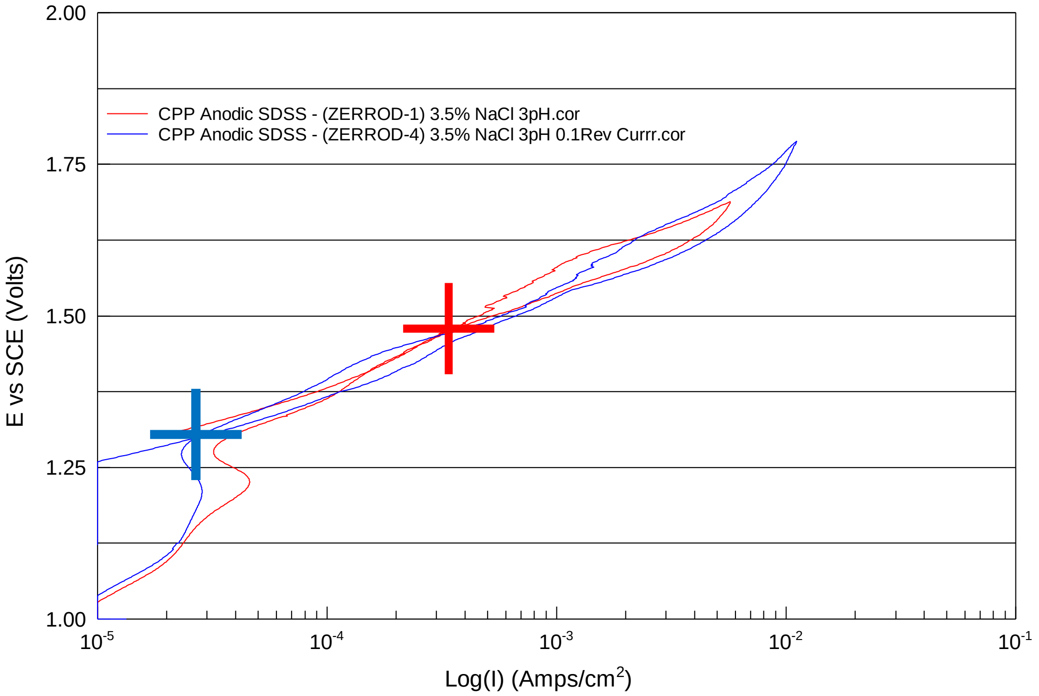

Figure 21: (a) Anodic potentiodynamic polarisation data for ZER (W+) with an i_{rev} of 0.05 vs 0.1 A.cm^{-2} with (b) enhanced view of associated hysteresis loops - tested in deoxygenated 0.6M NaCl at a pH of 3

Similar to FER(Cu+)'s comparison, ZER(W+)'s higher reverse limit sweep also showed good conformity to the regular scan and characteristic potentiodynamic features. This included the passive, transpassive and breakdown regions, all showing potential values as-anticipated for the alloy in these conditions compared to preceding sweeps. As was the case with FER(Cu+), sweep features prior to pitting breakdown potentials were unaffected by an increased reverse current density limit. In addition to this, ZER(W+) with the higher i_{rev} also showed a larger degree of hysteresis (wider loop), as well as a notably lower repassivation potential of 1.3V against 1.4$V_{vs\ SCE}$ of ZER(W+) with a lower i_{rev}. This yet again demonstrates the impact of a higher current density on passivity, with higher current densities being indicative of greater levels/faster rates of ion transportation, representative of corrosion REDOX reactions (oxidation/dissolution). To determine whether this inhibited repassivation stems from deep/severe pitting damage vs altered passivation kinetics of PL element formation, more direct in-situ chemical analysis is required.

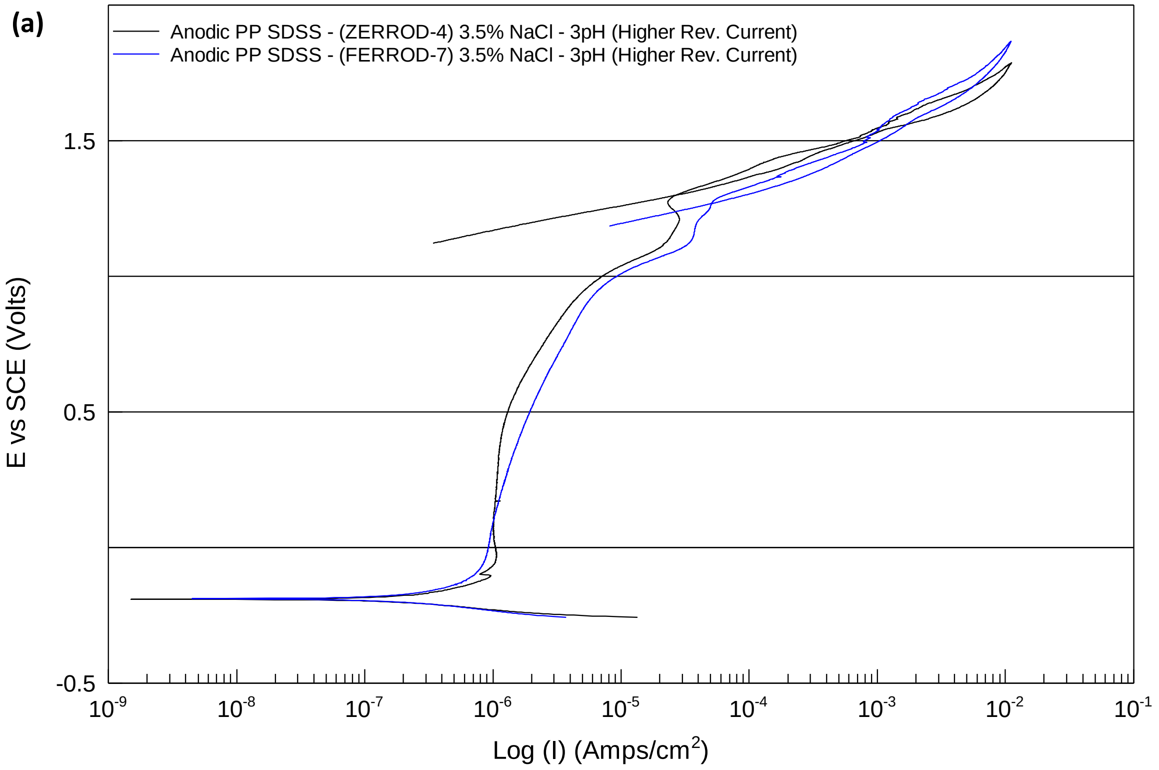

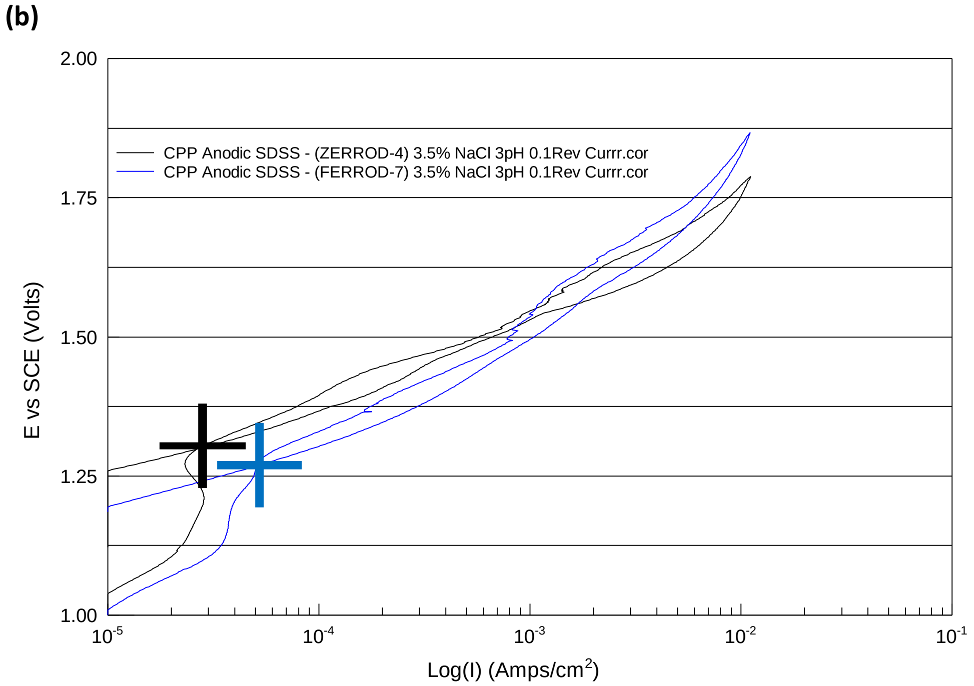

Figure 22: (a) Anodic potentiodynamic polarisation data for FER(Cu+) & ZER(W+) with an i_{rev} 0.1 A.cm^{-2}, with (b) enhanced view of associated hysteresis loops - tested in deoxygenated 0.6M NaCl at a pH of 3

FER(Cu+) displayed a marginally lower repassivation potential of 1.27V compared to ZER(W+) at 1.3$V_{vs\ SCE}$. Additionally, pitting current densities displayed by FER(Cu+) were marginally higher than ZER(W+) up until ~1.5$V_{vs\ SCE}$ where it was overtaken by ZER(W+), as presented in sweep comparison above. ZER(W+)'s hysteresis loop subtly infers a larger degree of pitting with its slightly wider geometry, it also reaches the i_{rev} limit of 0.1A.cm^{-2} at a lower (less noble) corresponding potential of 1.78V, compared to ZER(W+)'s 1.87$V_{vs\ SCE}$, a margin of 90mV. This implies a greater degree of bulk charge-transfer across the active area, which in a N_2-deoxygenated electrolyte, corresponds to higher anodic dissolution/ water reduction (O_2-evolution) activity. Whilst not entirely conclusive, these instances point towards a greater capability of larger Cu-wt.% specimens in mitigating the effects of pitting corrosion at higher current densities in acidic chloride media, compared to alloys with higher W-wt.%.

4.2 PP Summary Plots - Dependency of Passivation and Breakdown behaviour on alloy type and pH

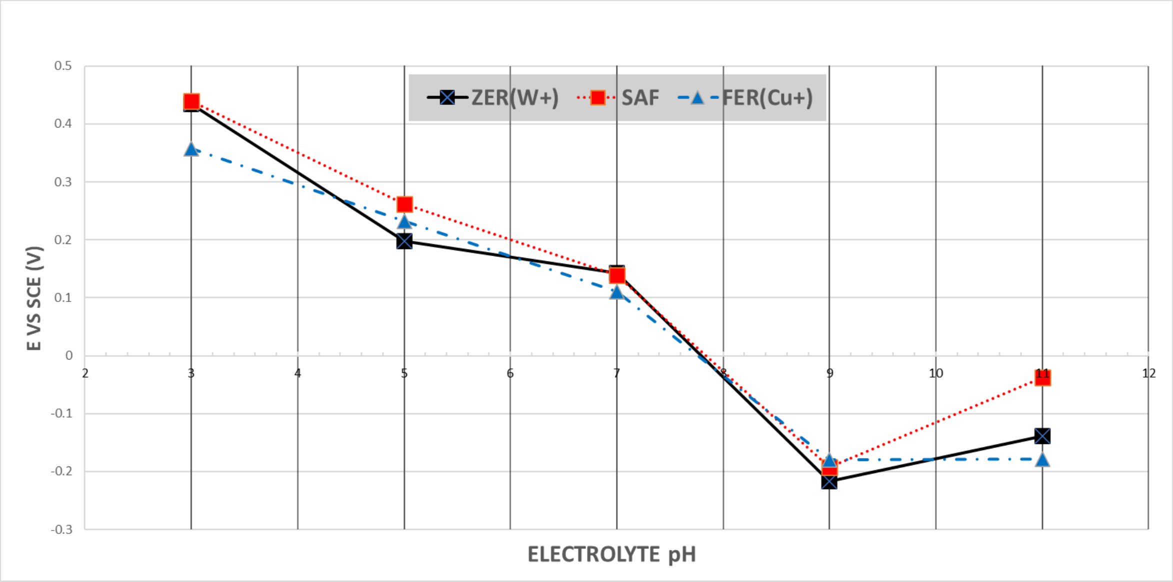

Figure 23: Dependency of OCP on pH for FER(Cu+), SAF and ZER(W+) alloys tested in deoxygenated 0.6M NaCl at a pH of 3, 5, 7, 9 and 11

In figure 23 the dependency of the SDSS alloys' OCP measurements immersed in a series of acidic and alkaline chloride-containing media is presented. Data stongly suggests that the open-circuit potential of all three alloys showed a negative, almost-linear dependency on pH across acidic, neutral and limited alkaline conditions[66]. OCP data obtained between alloys at pHs of 9 and 11 however indicate the OCP becomes more noble in highly-alkaline conditions.* The most noble OCP's of FER(Cu+), SAF and ZER(W+) measured as 0.357, 0.439 and 0.434$V_{\text{vs SCE}}$ respectively at 3pH, compared to the negative and least noble measurements at 9pH of -0.179, -0.192 and -0.217$V_{\text{vs SCE}}$. Regarding OCP as one measure of alloy's passivity, no significant relationship could be established between the compositional differences of the alloys and obsereved OCP data in neither acidic or alkaline NaCl media.

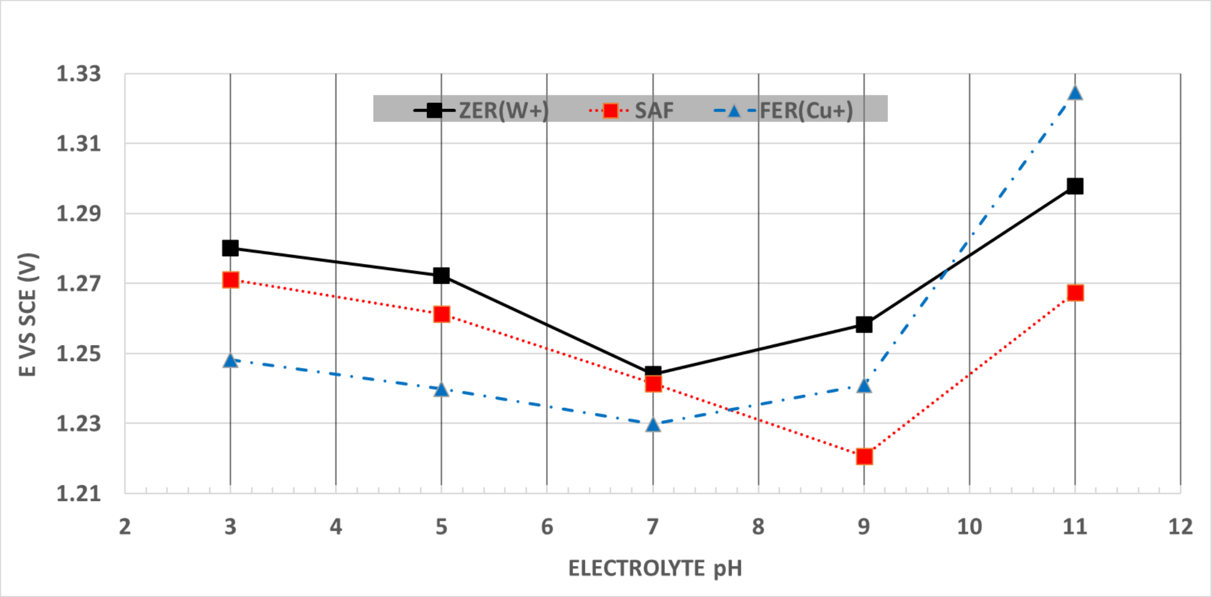

Figure 24: Dependency of Pitting potential (E_{pit}) on pH for FER(Cu+), SAF and ZER(W+) alloys tested in deoxygenated 0.6M NaCl at a pH of 3, 5, 7, 9 and 11

Figure 24 displays the variation of observed pitting potential (E_{pit}) across acidic to alkaline media of all three alloys. FER(Cu+), SAF and ZER(W+) all adhered well to characteristic potentiodynamic pitting breakdown behaviour described in previous literature. As such, all three alloys also exhibited similar trends in depency of E_{pit} with pH. As with OCP data, E_{pit} is most noble in stongly-acidic media of 3pH, but then steadiliy declines to lower potentials approaching neutral conditions. Amongst these conditions (3- 7pH), it was clear FER(Cu+) exhibited notably less-noble pitting potentials on average, indicating a slightly greater propensity to pitting breakdown. At 3pH, SAF and ZER(W+) had E_{pit} values of 1.271V and 1.28$V_{vs\ SCE}$ respectively, compared to FER(Cu+)'s 0.96$V_{vs\ SCE}$ (~0.31V difference), although this gap proceeds to reduce to ~0.01V at 7pH; with FER(Cu+)'s E_{pit} averaging at 1.23V against SAF and ZER(W+)'s E_{pit} of 1.241V and 1.244$V_{vs\ SCE}$. This observation is somewhat contrasted by FER(Cu+)'s superior resultant hysteresis geometry presented across nearly all pHs, where it's comparatively narrow and thin loops point to a lower degree of sustained pitting damage compared to SAF and ZER(W+) alloys. This being said, FER(Cu+)'s more active E_{pit} values alongside its smaller hysteresis loops may indicate Cu's benefit to PL integrity stems from repassivation kinetics/ pit penetration resistance, as opposed to prevention of onset of localised breakdown.

W-alloyed specimens displayed comparatively nobler E_{pit} values across most pHs, save for 11pH (ref. plot in fig 24 above), displaying the same trend of acidic-to-neutral E_{pit} decline (3-7pH) followed by an upturn in alkaline conditions. Although at pH of 11, ZER(W+)'s E_{pit} is overtaken in nobility by FER(Cu+). This in addition to ZER(W+)'s characteristically narrower hysteresis loop geometry, when compared to SAF, indicates a marked benefit of W-additions to enhancing PL stability and preventing pitting corrosion in SDSSs. Especially when compared to Cu-containing alloys acidic chloride media of pH 3 & 5 and standard SDSS alloys in alkaline media of pH 9. This being said, to confidently conclude this further PL chemical analysis and electrochemical impedance spectroscopy (EIS) would be required, possibly as future work to supplement this study.

Large W- and Cu-wt% alloys both indicated enhanced PL integrity at the point of breakdown when compared to SAF, but in slightly different conditions. In alkaline media (9 and 11 pH) both FER(Cu+) and ZER(W+) displayed nobler E_{pit} values, contrastingly in acidic and neutral media FER(Cu+) is outperformed by SAF and ZER(W+). These instances lead to suggestion that W-additions increase resistance to onset of localised breakdown in SDSSs within both acidic and alkaline chloride-containing media, as opposed to Cu-additions' enhancement in exclusively alkaline pHs (9 and 11).

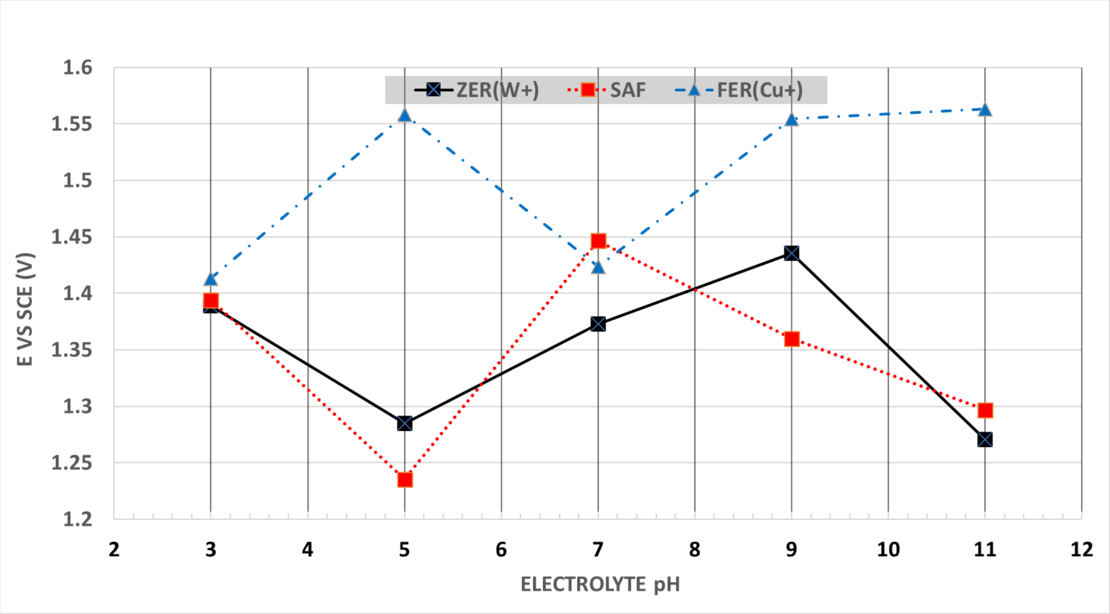

Figure 25: Dependency of repassivation potential (E_{rep}) on pH for FER(Cu+), SAF and ZER(W+) alloys tested in deoxygenated 0.6M NaCl at a pH of 3, 5, 7, 9 and 11

Alloy performance in repassivation potential comparison was generally less concurrent than with previous plots, most notably with FER(Cu+)'s E_{rep} data. Aside from data taken at pHs of 3 and 7, where all 3 alloys showed relatively similar E_{rep} values, FER(Cu+) was shown to repassivate at significantly nobler potentials compared to SAF and ZER(W+). This was especially the case at alkaline pHs of 9 and 11, as well as at the acidic pH of 5, with FER(Cu+)'s E_{rep} sitting at +0.26V, +0.12V and +0.25V higher than SAF or ZER(W+)'s respectively in chloride media. FER(Cu+)'s nobler E_{rep} values and it's narrower hysteresis loop geometry strongly inferred it's effectiveness in mitigation of pitting damage/penetration. This may be a result of the thermodynamically favourable formation of insoluble Cu-compounds in the PL, instigated by larger Cu-proportions in these conditions. This being said, as with previous and forthcoming chemical/passive-layer related conclusions drawn, validation using localised in-situ chemical analysis techniques during the breakdown/repassivation process is needed for a more substantive claim.

SAF and ZER(W+) exhibited similar behaviour trends across acidic, neutral and alkaline conditions. Both had repassivation potential-drops in nobility moving from a pH of 3 to 5, followed by a subsequent climb in E_{rep} at a neutral pH of 7. ZER(W+)'s E_{rep} then follows suit with FER(Cu+)'s and increases in nobility at 9pH where it then drops, whereas SAF sees a drop of E_{rep} nobility from 7 to 9 pH, but then follows suit with ZER(W+)'s drop from 9 to 11pH.

In spite of a noticeable advantage displayed in pitting damage mitigation, namely when comparing it's hysteresis geometry to SAF's (low wt%-Cu and 0 wt%-W), ZER(W+) appeared to show no significant influence in resultant repassivation potentials. Consequentially, no added benefit to repassivation of SDSSs in acidic or alkaline NaCl-containing media could be attributed directly to greater W-additions. Cu on the other hand however, displayed a clear advantage to alloys in chloride media of 5, 9 and 11 pH respectively.

4.3 SVET - In-situ analysis of transpassive SDSS behaviour

Previous in-situ studies of corrosion morphology development of the three different types of SDSS investigated in this study were carried out by time-lapse optical microscopy of anodically polarised specimens held in 3.5 wt% NaCl (aq) [57]. In the case of each SDSS, the transpassive behaviour was characterised by a selective etch of the exposed surface, typified by the images shown in Figure 26 for a SAF surface held at a potential of +1.25 $_{\text{Vs SCE}}$ in and photographed at low magnification using an optical microscope at regular time intervals over a 10 min duration when immersed in 3.5 wt% NaCl (aq) at pH 6. It can be seen from Figure 26, that the visual evidence of grain darkening and selective phase dissolution initiates around the periphery of the exposed circular area and with time affects the entirety of the surface. This previous visual investigation, however, did not yield any information on the magnitude of the anodic currents emerging from the corroding surface, nor demonstrate if the regions affected by anodic dissolution retained their activity throughout the time of polarisation.

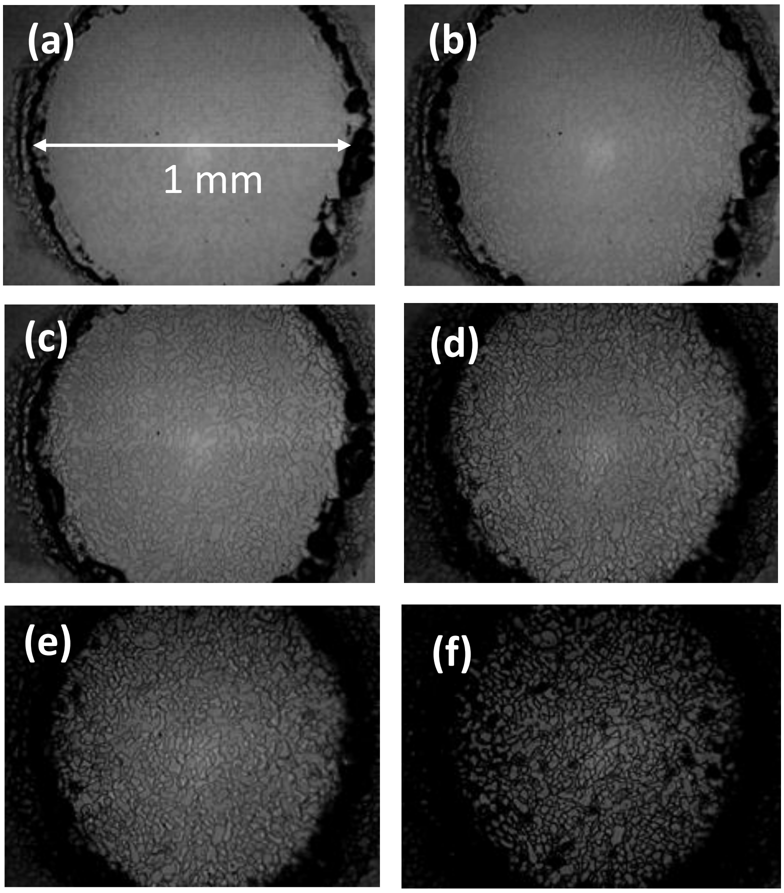

Figure 26: Time-lapse microscopy sequence showing the development of corrosion morphology over a 1 mm diameter circular area of exposed SAF (UNS32750) surface under

immersion in 3.5% NaCl (aq) electrolyte at pH 6, when polarised at a potential of +1.25 $V_{vs\ SCE}$. Time key: (a) 0 min, (b) 1 min, (c) 3 min, (d) 5 min, (e) 8 min, (f) 12 min after the start of polarisation. Adapted from reference [57]

In order to obtain more information on the trans-passive behaviour of SAF, FER(Cu+) and ZER(W+) SDSS types, an in-situ SVET analysis of their time-dependent localised corrosion behaviour under anodic polarisation was carried out. Using an approach previously adopted for the investigation of pure Mg under anodic polarisation [67], [68], SVET mappings of current density distributions over 25 mm^2 areas of exposed SDSS surface were carried out as described in Section 3. The anodic polarisation was carried out under galvanostatic control at an applied current density of 10 mA/cm^2 using the SDSS specimen as a working electrode, with a Pt gauze electrode, immersed in the same electrolyte bath used as a counter electrode. SVET scans were recorded initially under open circuit conditions and subsequently at 8 min intervals after the start of anodic polarisation over a total duration of 4h immersion. The results obtained for a SAF specimen prior to and immediately after the start of anodic polarisation are given in Figure 27, where (a) shows a colour-coded current density (j_z) image map obtained under freely corroding conditions while (b) shows the distribution of j_z values 8 min after the application of an externally imposed anodic current density of 10 mA/cm^2.

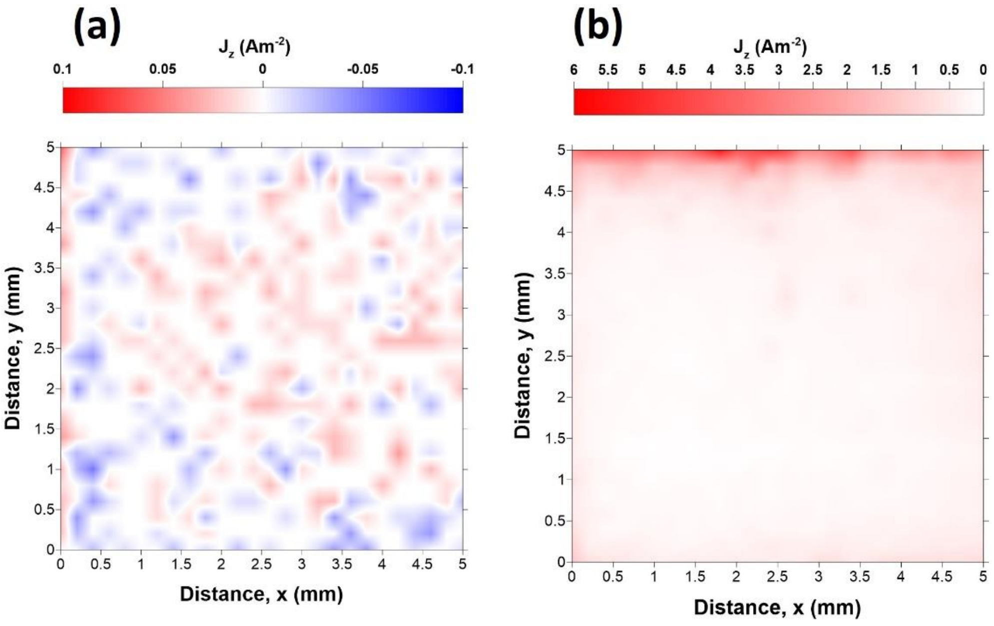

Figure 27: SVET-derived current density (j_z) distribution maps obtained for a SAF surface immersed in a 3.5wt% NaCl (aq) solution with a pH of 5 at, (a) under freely corroding conditions (i.e. at OCP) and (b) 8 min after starting galvanostatic polarization at +10 mA cm^{-2}.

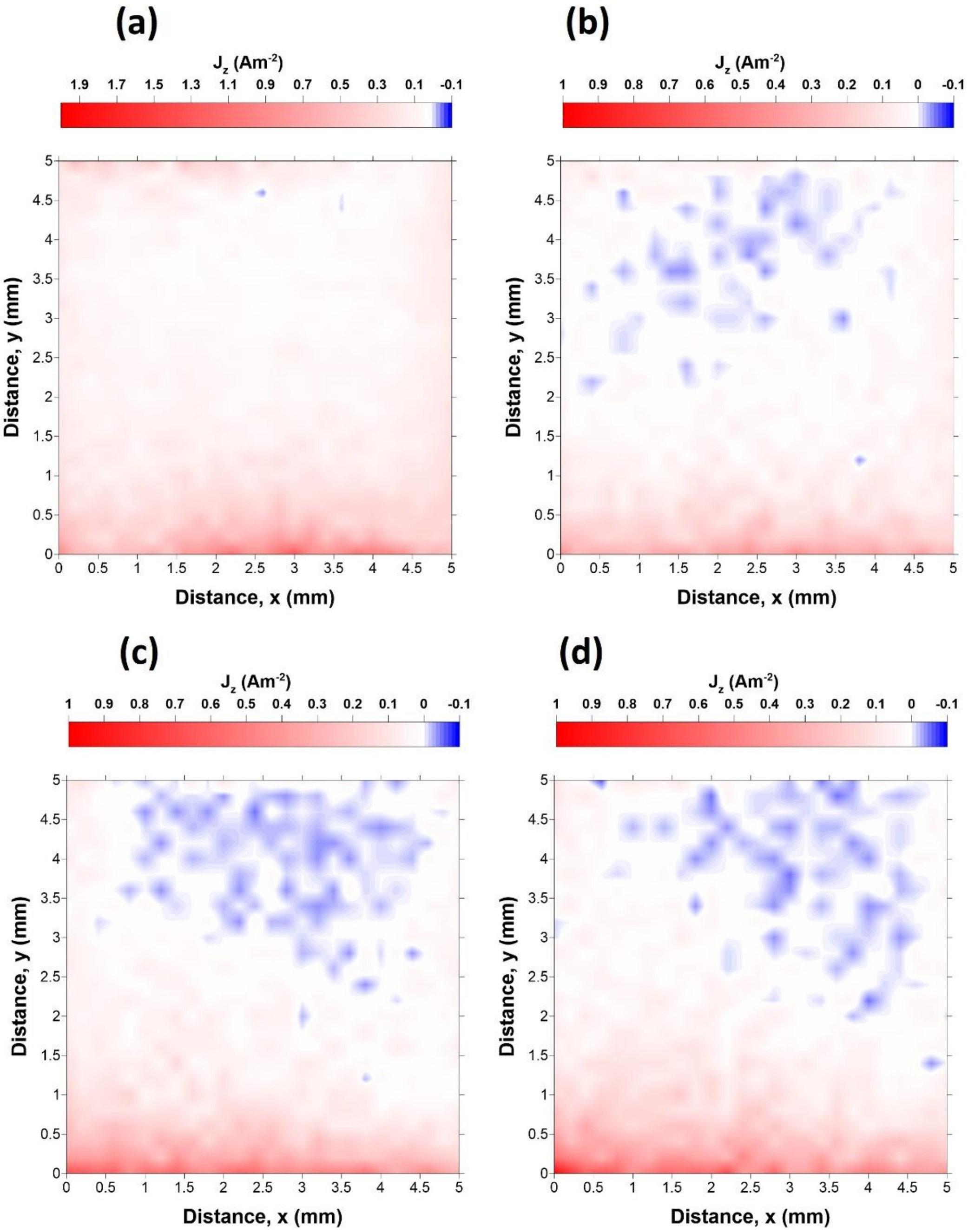

Figure 28: SVET-derived current density (j_z) distribution maps obtained for a SAF surface immersed in a 3.5 wt% NaCl (aq) solution with a pH of 5 at (a) 1h, (b) 2h, (c) 3h and (d) 4 h after starting galvanostatic polarization at +10 mA cm^{-2}.

Fig 27 (a) confirms that the specimen is passive in the absence of applied current, where the measure of j_z values in the range -0.05 to +0.05 A m^{-2} are indicative of the values obtained when scanning over an inert surface (e.g. a glass slide). Once an anodic current is imposed, most of the exposed surface is shown as a weak anode where j_z values of up to +1 A m^{-2} are measured, although a 0.5 mm wide strip close to the upper edge of the specimen showed significantly higher values of up to +5 A m^{-2}. At longer times, the j_z patterns change and more significant anodic activity develops in the bottom half of the scanned area as shown in the sequence of maps given in Figure 28 which are obtained at hourly intervals during the 4 h experiment. At these protracted holding times, the maximum measured anodic j_z values have decrease to ca +1 A m^{-2}, but the exposed area affected by anodic dissolution appears to expand from the bottom edge of the scan area with each hourly scan, eventually affecting most of the lower half of the scan area after 4h. However, at no point during the 4 h experiment did the SVET analysis detect highly focal intense anodic events, such as those associated with the pitting corrosion of stainless steels [56]. As such it can be concluded that regions of SAF SDSS undergoing selective etching under anodic polarisation were characterised by jz values of ca +5 A.m^{-2}, dropping to significantly lower values of ca +1 A.m^{-2} with time, although occupying a markedly larger area of the exposed surface.

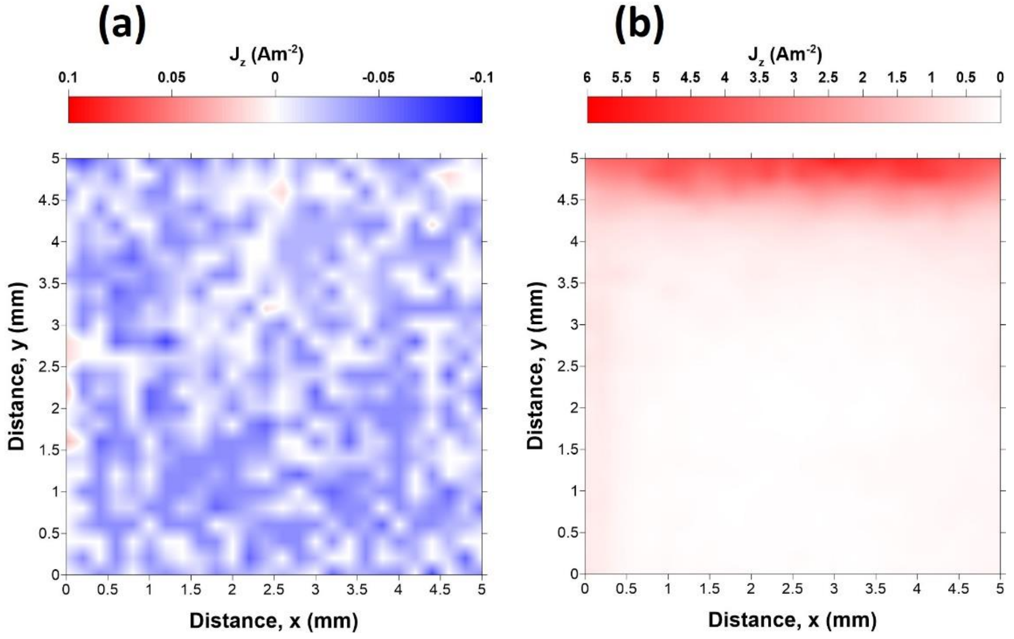

Figure 29: SVET-derived current density (j_z) distribution maps obtained for a FER(Cu+) (UNS32550) surface immersed in a 3.5 wt% NaCl (aq) solution, (a) under freely corroding conditions (i.e. at OCP) and (b) 8 min after starting galvanostatic polarization at +10 mA cm^{-2}.

The same type of experiment was also carried out using a FER(Cu+) specimen to ascertain whether the different copper content would produce a variation in the observed j_z distributions determined by SVET mapping. The results obtained prior to and immediately following the application of an applied galvanostatic current density of +10 mA/cm^2 are shown in Figure 29, confirming that the initial behaviour remains very similar to that observed for the SAF sample (ref Figure 27).

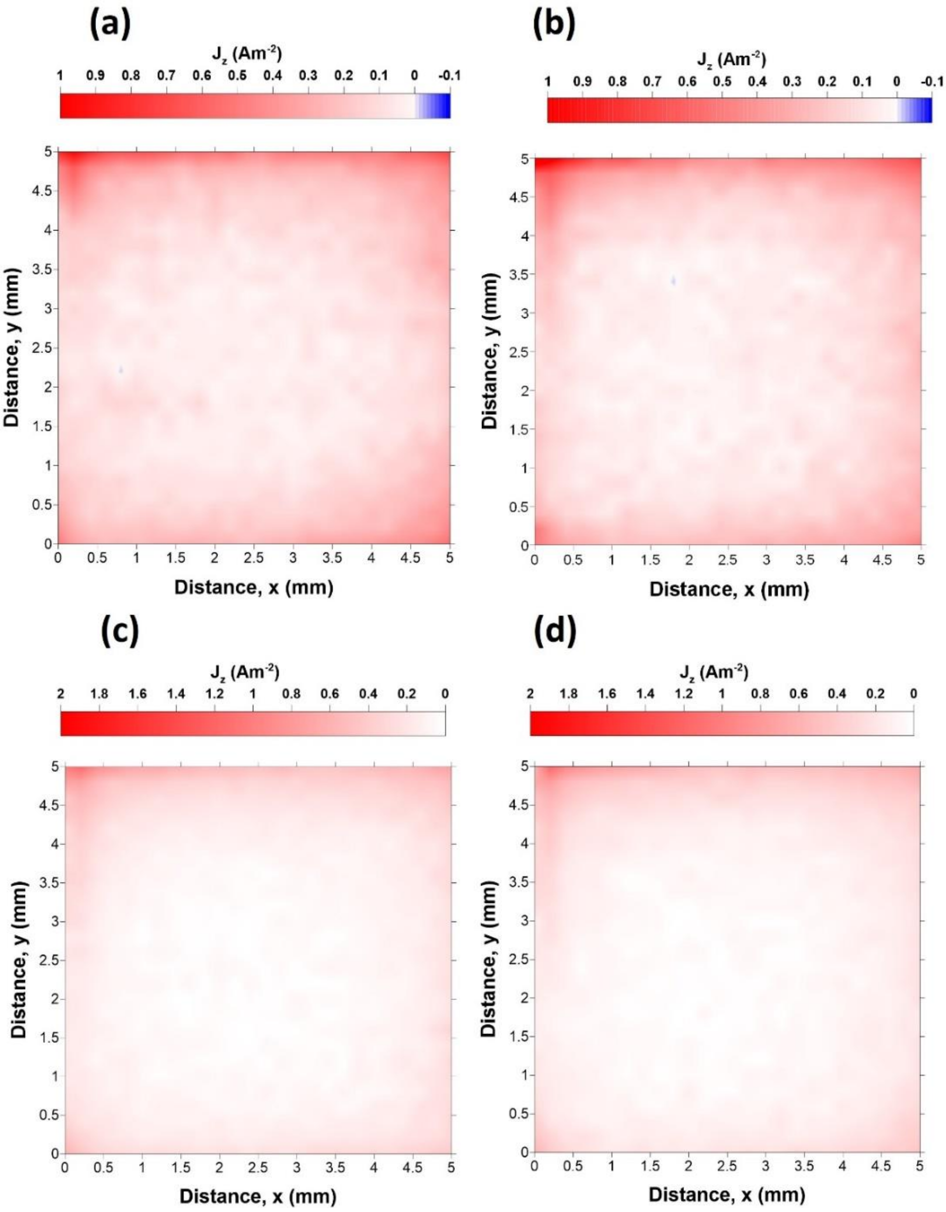

Figure 30: SVET-derived current density (j_z) distribution maps obtained for a FER(Cu+) (UNS32550) surface immersed in a 3.5 wt% NaCl (aq) solution (a) 1h, (b) 2h, (c) 3h and (d) 4 h after starting galvanostatic polarization at +10 mA cm^{-2}.

At longer holding times (see Figure 30), the areas of most intense anodic activity, marked by j_z values of ca 1 A.m^{-2} become confined to the outer edges of the scan area and do not appear to grow inwards with time. As such, the findings agree with visual observations made using time-lapse microscopy [57], where activity initiates in the vicinity of the physical boundary used to isolate a known working area of specimen. However, in this work a significantly larger working area (25 mm^2 compared to 0.8 mm^2) is used and as such the evolution of anodic j_z values associated with selective phase dissolution to regions within the centre of the scan area is not detected over the 4 h duration of the experiment. A 3rd experiment using a ZER(W+) specimen also showed similar results over an initial 30 min duration, but had to be halted due to a faulty connection to the SVET probe. Time constraints meant that this experiment could not be repeated.

5. Conclusions

5.1. Anodic PP

- Regarding OCP as one measure of alloy's passivity, no significant relationship could be established between the compositional differences of the alloys and obsereved OCP data in neither acidic or alkaline NaCl media.
- W- and Cu- alloyed specimens displayed comparatively nobler E_{bd} values across most pHs, save for 11pH (ref. plot (a) in fig 24 above), displaying the same trend of acidic-to-neutral E_{bd} decline (3-7pH) followed by an upturn in alkaline conditions. Although at pH of 11, ZER(W+)'s E_{bd} is overtaken in nobility by FER(Cu+)'s. This in addition to ZER(W+)'s characteristically narrower hysteresis loop geometry, when compared to SAF, indicates a marked benefit of W-additions to enhancing PL stability and preventing localised corrosion in SDSSs. Especially when compared to Cu-containing alloys in acidic chloride media of pH 3-5 and standard SDSS alloys in alkaline media of pH 9. This being said to confidently conclude this postulation, further PL chemical analysis and electrochemical impedance spectroscopy (EIS) would be required, possibly as future work to supplement this study.
- FER(Cu+)'s more noble E_{bd} values alongside it's smaller hysteresis loops may indicate Cu's benefit to PL integrity stems from repassivation kinetics/ pit penetration impedence, as opposed to prevention of onset of localised breakdown. This is supported in existing literature surrounding the kinectics of PL element diffusion mechanics within copper-alloyed stainless steels.
- FER(Cu+)'s nobler E_{rep} values and it's narrower hysteresis loop geometry strongly inferred it's effectiveness in mitigation of pitting damage/penetration. This may be a result of the thermodynamically favourable formation of insoluble Cu-compounds in the PL, instigated by larger Cu-proportions in these conditions. This being said, as with previous chemical/passive-layer related conclusions drawn, validation using localised in-situ chemical analysis techniques during the breakdown/repassivation process is needed for a more substantive conclusion.

5.2. SVET

- Results of in-situ SVET analysis of relevant SDSS specimens showed that trans-passive behaviour consisted of a weakly anodic surface with regions of the most intense anodic dissolution always confined to the edges of the scan area. For the SAF specimen, there seemed to be evidence of a growth in the area occupied by selective anodic dissolution with time over a duration of 4h. However, for the Ferralium specimen (FER(Cu+)), there was very little change of the j_z distribution maps with time and the most intense areas of anodic dissolution were always constrained to the extremities of the scan area. In both cases the maximum measured anodic jz values decreased rapidly from +5 A m^{-2} measured immediately at the start of anodic polarisation to constant values of ca + 1 A m^{-2} after 1h and for the duration of the 4h experiments.

6. Recommendations for Future Work

Drawing from the findings and conclusions from this work, there are a number of recommendations for future work which can be made. For one; using the SKPFM technique on SDSS test surfaces to produce pre- and post-corrosion volta-potential maps, similar to that of the galvanostatic scans discussed in the SVET results section. Doing so could potentially reveal the development of localised nobility changes during corrosion and further clarify the roles of ferrite and austenite phases in transpassive dissolution/local pitting. Furthermore, the SKPFM may be used to evaluate nobility gradients at grain boundaries, as well as for further characterisation of nobility gradients at the boundary of the active areas. This may help understand the observed edge-effects which seemed to concentrate anodic dissolution at the test boundaries within the course of this study.

Further in-situ optical analysis of corroding SDSS specimens would also better help correlate SDSS alloy performance to observed phenomena presented in the PP and SVET. Similar to previous work with time-lapse microscopy[57], such work would help distinguish the dominant mechanisms of dissolution in each alloy postulated in the results section of this thesis.

Finally, it may be of particular interest to study the effects of alternative media on observed corrosion performance and mechanisms of SDSS alloys. Particularly with regard to Hydrogen embrittlement, considering the increasing prominence of green energy applications making use of the element.

7. References

[1] R. N. Gunn, *Duplex stainless steels microstructure, properties and applications*. Abington Publishing, 1997. [Online]. Available: https://books.google.co.uk/books?hl=en&lr=&id=HayjAgAAQBAJ&oi=fnd&pg=PP1&dq=Duplex+stainless+steels+and+localized+corrosion+resistance+P+Combrade,+JP+Audouard+-+Duplex+Stainless+Steels%2791.,+1991&ots=5JwlqtVTi_&sig=2wvsC6EWmBSfn5ETLZWltnkM2YI&redir_esc=y

[2] J. Olsson and M. Liljas, “60 Years of Duplex Stainless Steel Applications,” Avesta, Dec. 1994. Accessed: Feb. 08, 2023. [Online]. Available: https://www.osti.gov/biblio/80126

[3] I. Weibull, “Duplex Stainless Steels and Their Application, particularly in Centrifugal Separators. Part A* History & Development,” 1987. doi: https://doi.org/10.1016/0261-3069(87)90058-6.

[4] R. M. Davison, “Welding of duplex stainless steels,” in *Engineering, Pulping and Environmental Conference 2007, TAPPI*, 2007, vol. 3, pp. 2144–2163. doi: 10.4028/www.scientific.net/kem.69-70.217.

[5] Dr. S. D. Kahar, “Duplex Stainless Steels-An overview,” *Int J Eng Res Appl*, vol. 07, no. 04, pp. 27–36, Apr. 2017, doi: 10.9790/9622-0704042736.

[6] D. Zhang, A. Liu, B. Yin, and P. Wen, “Additive manufacturing of duplex stainless steels - A critical review,” *Journal of Manufacturing Processes*, vol. 73. Elsevier Ltd, pp. 496–517, Jan. 01, 2022. doi: 10.1016/j.jmapro.2021.11.036.

[7] V. Hosseini, “Super duplex stainless steels : Microstructure and properties of physically simulated base and weld metal,” 2018. [Online]. Available: http://urn.kb.se/resolve?urn=urn:nbn:se:hv:diva-12850

[8] G. Gedge, “Use of Duplex Stainless Steel Plate for Durable Bridge Construction,” in *IABSE Symposium, Weimar 2007: Improving Infrastructure Worldwide*, 2007, vol. 93, pp. 84–85. doi: 10.2749/222137807796119771.

[9] S. H. Bhadeshia and S. R. Honeycombe, *Steel: Microstructure and Properties (4th Edition)*. 2017.

[10] J. O. Nilsson, “Super duplex stainless steels,” *Materials Science and Technology (United Kingdom)*, vol. 8, no. 8, pp. 685–700, 1992, doi: 10.1179/mst.1992.8.8.685.

[11] G. S. Reis, A. M. Jorge Jr., and O. Balancin, “Influence of the microstructure of duplex stainless steels on their failure characteristics during hot deformation,” *Materials Research*, vol. 3, no. 2, pp. 31–35, 2000, doi: 10.1590/S1516-14392000000200006.

[12] P. Tao, J. ming Gong, Y. fei Wang, Y. Jiang, Y. Li, and W. wei Cen, “Characterization on stress-strain behavior of ferrite and austenite in a 2205 duplex stainless steel based on nanoindentation and finite element method,” *Results Phys*, vol. 11, no. June, pp. 377–384, 2018, doi: 10.1016/j.rinp.2018.06.023.

[13] M. W. Tofique and Karlstads universitet. Institutionen för ingenjörsvetenskap och fysik., *Very high cycle fatigue of duplex stainless steels and stress intensity calculations*. Faculty of Health, Science and Technology, Materials Engineering, Karlstads universitet, 2014.

[14] T. Björk, H. Mettänen, A. Ahola, M. Lindgren, and J. Terva, “Fatigue strength assessment of duplex and super-duplex stainless steels by 4R method,” *Welding in the World*, vol. 62, no. 6, pp. 1285–1300, Nov. 2018, doi: 10.1007/s40194-018-0657-8.

[15] Z. Szklarska-Smialowska, *Pitting and Crevice Corrosion - 13 Effect of Alloying Elements on Stainless Steels and Ni-based Alloys*. NACE International, 1968.

[16] D. M. Fellicia, Sutarsis, B. A. Kurniawan, D. Wulanari, A. Purniawan, and A. T. Wibisono, “Study of Sigma Phase in Duplex SAF 2507,” *IOP Conf Ser Mater Sci Eng*, vol. 202, no. 1, 2017, doi: 10.1088/1757-899X/202/1/012039.

[17] F. Iacoviello and L. D. Agostino, “Integranular corrosion susceptibility analysis in austeno-ferritic (duplex) stainless steels,” *Procedia Structural Integrity*, vol. 3, pp. 276–282, 2017, doi: 10.1016/j.prostr.2017.04.036.

[18] M. Drahansky *et al.*, “Phase Transformations in Duplex Stainless Steel: An Assessment by In Situ X-Ray Diffraction,” *Intech*, vol. i, no. tourism, p. 13, 2016, doi: http://dx.doi.org/10.5772/57353.

[19] T. Berguiga and Z. Boumerzoug, “Effect of Sigma-phase Precipitation on Mechanical Behaviour and Pitting Corrosion of Duplex Stainless Steel,” *Acta Metallurgica Slovaca*, vol. 25, no. 1, pp. 4–17, Jun. 2021, doi: 10.36547/ams.25.1.1.

[20] D. S. S. Conference *et al.*, “Duplex stainless steels ’91 : 28-30 octobre 1991 Beaune, Bourgogne, France. Vol. 2 Vol. 2,” 1992.

[21] S. Atamert and J. E. King, “Sigma-phase formation and its prevention in duplex stainless steels,” *J Mater Sci Lett*, vol. 12, no. 14, pp. 1144–1147, 1993, doi: 10.1007/BF00420548.

[22] Z. Shi, G. Song, and A. Atrens, “The corrosion performance of anodised magnesium alloys,” *Corros Sci*, vol. 48, no. 11, pp. 3531–3546, 2006, doi: 10.1016/j.corsci.2006.02.008.

[23] C. R. Lauritsen, “Pitting Corrosion of Super Duplex Stainless Steel- Effect of Isothermal Heat Treatment,” *NTNU*, no. June, p. 146, 2016.

[24] R. A. Perren *et al.*, “Corrosion resistance of super duplex stainless steels in chloride ion containing environments: Investigations by means of a new microelectrochemical method. I. Precipitation-free states,” *Corros Sci*, vol. 43, no. 4, pp. 707–726, 2001, doi: 10.1016/S0010-938X(00)00087-1.

[25] E. C. Souza, S. M. Rossitti, and J. M. D. A. Rollo, “Influence of chloride ion concentration and temperature on the electrochemical properties of passive films formed on a superduplex stainless steel,” *Mater Charact*, 2010, doi: 10.1016/j.matchar.2009.12.004.

[26] M. Långberg *et al.*, “Redefining passivity breakdown of super duplex stainless steel by electrochemical operando synchrotron near surface X-ray analyses,” *Npj Mater Degrad*, vol. 3, no. 1, Dec. 2019, doi: 10.1038/s41529-019-0084-3.

[27] H. Parangusan, J. Bhadra, and N. Al-Thani, “A review of passivity breakdown on metal surfaces: influence of chloride- and sulfide-ion concentrations, temperature, and pH,” *Emergent Mater*, vol. 4, 2021, doi: 10.1007/s42247-021-00194-6/Published.

[28] J. Pan, “Studying the Passivity and Breakdown of Duplex Stainless Steels at Micrometer and Nanometer Scales – The Influence of Microstructure,” *Frontiers in Materials*, vol. 7. Frontiers Media S.A., May 15, 2020. doi: 10.3389/fmats.2020.00133.

[29] M. Nishimoto, I. Muto, Y. Sugawara, and N. Hara, “Passivity of (Mn,Cr)S inclusions in type 304 stainless steel: The role of Cr and the critical concentration for preventing inclusion dissolution in NaCl solution,” *Corros Sci*, vol. 176, Nov. 2020, doi: 10.1016/j.corsci.2020.109060.

[30] Z. Cui *et al.*, “Passivation behaviour and surface chemistry of 2507 super duplex stainless steel in artificial seawater: Influence of dissolved oxygen and pH,” *Corros Sci*, vol. 150, pp. 218–234, Apr. 2019, doi: 10.1016/j.corsci.2019.02.002.

[31] L. Weber and P. J. Uggowitzer, “Partitioning of chromium and molybdenum in super duplex stainless steels with respect to nitrogen and nickel content,” Zurich, Jan. 1998.

[32] P. Reccagni, L. H. Guilherme, Q. Lu, M. F. Gittos, and D. L. Engelberg, “Reduction of austenite-ferrite galvanic activity in the heat-affected zone of a Gleeble-simulated grade 2205 duplex stainless steel weld,” *Corros Sci*, vol. 161, Dec. 2019, doi: 10.1016/j.corsci.2019.108198.

[33] C. Örnek, C. Leygraf, and J. Pan, “On the Volta potential measured by SKPFM–fundamental and practical aspects with relevance to corrosion science,” *Corrosion Engineering Science and Technology*, vol. 54, no. 3, pp. 185–198, 2019, doi: 10.1080/1478422X.2019.1583436.

[34] E. Salama, M. M. Eissa, and A. S. Tageldin, “Distinct properties of tungsten austenitic stainless alloy as a potential nuclear engineering material,” *Nuclear Engineering and Technology*, vol. 51, no. 3, pp. 784–791, Jun. 2019, doi: 10.1016/j.net.2018.12.021.

[35] S. Jung *et al.*, “Effects of tungsten and molybdenum on high-temperature tensile properties of five heat-resistant austenitic stainless steels,” *Materials Science and Engineering A*, vol. 656, pp. 190–199, Feb. 2016, doi: 10.1016/j.msea.2016.01.022.

[36] E. B. Haugan, M. Næss, C. T. Rodriguez, R. Johnsen, and M. Iannuzzi, “Effect of tungsten on the pitting and crevice corrosion resistance of Type 25Cr super duplex stainless steels,” *Corrosion*, vol. 73, no. 1, pp. 53–67, Jan. 2017, doi: 10.5006/2185.

[37] J. S. Kim, P. J. Xiang, and K. Y. Kim, “Effect of Tungsten and Nickel Addition on the Repassivation Behavior of Stainless Steel,” Houston, 2005. doi: DOI:10.5006/1.3278172.

[38] K. Ogawa and T. Osuki, “Effects of alloying elements on sigma phase precipitation in duplex stainless steel (1) - Modelling of effects of chromium, molybdenum and tungsten on sigma phase growth rate in super duplex stainless steel -,” *ISIJ International*, vol. 59, pp. 122–128, Jan. 2019, doi: 10.2355/isijinternational.ISIJINT-2018-477.

[39] K. Ogawa and T. Osuki, “Effects of alloying elements on sigma phase precipitation in duplex stainless steel (2) - Effects of alloying chromium, molybdenum and tungsten on C-curve of sigma phase precipitation in duplex stainless steel -,” *ISIJ International*, vol. 59, pp. 129–135, Jan. 2019, doi: 10.2355/isijinternational.ISIJINT-2018-478.

[40] J.-O. Nilsson, T. Huhtala, P. Jonsson, L. Karlsson, and A. Wilson, “Structural Stability of Super Duplex Stainless Weld Metals and Its Dependence on Tungsten and Copper,” 1996.

[41] K. Ogawa, H. Okamoto, M. Ueda, M. Igarashi, T. Moriand, and T. Kobayashi, “Effects of tungsten on pitting corrosion resistance and impact toughness in the HAZ of duplex stainless steel - study of weldability of high-tungsten duplex stainless steel (1st Report),” *Welding International*, vol. 10, no. 6, pp. 466–472, Jan. 1996, doi: 10.1080/09507119609549032.

[42] H. M. L. F. de Lima, S. S. M. Tavares, M. Martins, and W. S. Araújo, “The effect of copper addition on the corrosion resistance of cast duplex stainless steel,” *Journal of Materials Research and Technology*, vol. 8, no. 2, pp. 2107–2119, Apr. 2019, doi: 10.1016/j.jmrt.2019.01.018.

[43] J. H. Hong, S. H. Lee, J. G. Kim, and J. B. Yoon, “Corrosion behaviour of copper containing low alloy steels in sulphuric acid,” *Corros Sci*, vol. 54, no. 1, pp. 174–182, Jan. 2012, doi: 10.1016/j.corsci.2011.09.012.

[44] T. Sourisseau, E. Chauveau, and B. Baroux, “Mechanism of copper action on pitting phenomena observed on stainless steels in chloride media,” *Corros Sci*, vol. 47, no. 5, pp. 1097–1117, May 2005, doi: 10.1016/j.corsci.2004.05.024.

[45] J. Banas and A. Mazurkiewicz, “The effect of copper on passivity and corrosion behaviour of ferritic and ferritic-austenitic stainless steels,” 2000. [Online]. Available: www.elsevier.com/locate/msea

[46] S. H. Jeon, H. J. Kim, K. H. Kong, and Y. S. Park, “Effects of copper addition on the passivity and corrosion behavior of 27Cr-7Ni hyper duplex stainless steels in sulfuric acid solution,” *Mater Trans*, vol. 56, no. 1, pp. 78–84, 2014, doi: 10.2320/matertrans.M2014233.

[47] U. Kivisäkk and J. Frodigh, “Influence of Copper in Super Duplex Stainless Steels on Iso-Corrosion Curves in Hydrochloric Acid and Dilute Sulfuric Acid,” *NACE CORROSION International*, vol. 1, no. 1, Mar. 2013.

[48] C. Leygraf, I. Odnevall Wallinder, J. Tidblad, and T. Graedel, *Atmospheric Corrosion, Second Edition (Chapter 2)*, 2nd ed. Wiley, 2016.

[49] K. Wandelt, *Surface Science And Electrochemistry*. Elsevier 2018.

[50] S. Esmailzadeh, M. Aliofkhazraei, and H. Sarlak, “Interpretation of Cyclic Potentiodynamic Polarization Test Results for Study of Corrosion Behavior of Metals: A Review,” *Protection of Metals and Physical Chemistry of Surfaces*, vol. 54, no. 5, pp. 976–989, 2018, doi: 10.1134/S207020511805026X.

[51] Mahmood Aliofkhazraei, Ali Nasar, Mircea Chipara, Nadhira Bensaada Laidani, and Jeff Th.M. De Hosson, Eds., *Handbook of Modern Coating Technologies Advanced Characterization Methods*, 1st ed., vol. 2. Elsevier, 2021. doi: 10.1016/C2012-0-06249-7.

[52] S. Fajardo, F. R. García-Galvan, V. Barranco, J. C. Galvan, and S. Feliu Batlle, “A Critical Review of the Application of Electrochemical Techniques for Studying Corrosion of Mg and Mg Alloys: Opportunities and Challenges,” in *Magnesium Alloys - Selected Issue*, IntechOpen, 2018. doi: 10.5772/intechopen.79497.

[53] N. Jadhav and V. J. Gelling, “Review—The Use of Localized Electrochemical Techniques for Corrosion Studies,” *J Electrochem Soc*, vol. 166, no. 11, pp. C3461–C3476, 2019, doi: 10.1149/2.0541911jes.

[54] A. C. Bastos, M. C. Quevedo, O. v. Karavai, and M. G. S. Ferreira, “Review - On the application of the scanning vibrating electrode technique (SVET) to corrosion research,” *J Electrochem Soc*, vol. 164, no. 14, pp. C973–C990, 2017, doi: 10.1149/2.0431714jes.

[55] N. Fuertes, V. Bengtsson, R. Pettersson, and M. Rohwerder, “Use of SVET to evaluate corrosion resistance of heat tinted stainless steel welds and effect of post-weld cleaning,” *Materials and Corrosion*, vol. 68, no. 1, pp. 7–19, Jan. 2017, doi: 10.1002/maco.201609048.

[56] G. Williams and H. N. Mcmurray, “Pitting Corrosion of Steam Turbine Blading Steels: The Influence of Chromium Content, Temperature, and Chloride Ion Concentration,” Swansea, 2006. doi: 10.5006/1.3278269.

[57] J. Bonfield, “The influence of copper and tungsten additions on the passivity and pitting corrosion resistance of super duplex stainless steels,” Masters Thesis, Swansea University, 2019.

[58] C. Nyby *et al.*, “Electrochemical metrics for corrosion resistant alloys,” *Sci Data*, vol. 8, no. 1, p. 58, Feb. 2021, doi: 10.1038/s41597-021-00840-y.

[59] G. Williams and H. Neil McMurray, “Localized Corrosion of Magnesium in Chloride-Containing Electrolyte Studied by a Scanning Vibrating Electrode Technique,” *J Electrochem Soc*, vol. 155, no. 7, p. C340, 2008, doi: 10.1149/1.2918900.

[60] L. A. Santa-Cruz, G. Machado, A. A. Vicente, T. F. C. Hermenegildo, and T. F. A. Santos, “Effect of high anodic polarization on the passive layer properties of superduplex stainless steel friction stir welds at different chloride electrolyte pH values and temperatures,” *International Journal of Minerals, Metallurgy and Materials*, vol. 26, no. 6, pp. 710–721, Jun. 2019, doi: 10.1007/s12613-019-1790-0.

[61] M. Zhu, F. He, Y. F. Yuan, S. M. Yin, S. Y. Guo, and J. Pan, “Effect of Aging Time on the Microstructure and Corrosion Behavior of 2507 Super Duplex Stainless Steel in Simulated Marine Environment,” *J Mater Eng Perform*, vol. 30, no. 8, pp. 5652–5666, Aug. 2021, doi: 10.1007/s11665-021-05812-2.

[62] M. R. G De Chialvo, R. C. Salvarezza, D. Vasquez Moll, and A. J. Arvia, “Kinetics Of Passivation And Pitting Corrosion Of Polycrystalline Copper In Borate Buffer Solutions Containing Sodium Chloride”, Electrochimica Acta, vol 30, issue 11, Nov. 1985, Pg 1501-1511

[63] N. Ebrahimi, M. H. Moayed, and A. Davoodi, “Critical pitting temperature dependence of 2205 duplex stainless steel on dichromate ion concentration in chloride medium,” *Corros Sci*, vol. 53, no. 4, pp. 1278–1287, 2011, doi: 10.1016/j.corsci.2010.12.019.

[64] L. Sun *et al.*, “Point defect model for passivity breakdown on hyper-duplex stainless steel 2707 in solutions containing bromide at different temperatures,” *Corros Sci*, vol. 194, Jan. 2022, doi: 10.1016/j.corsci.2021.109959.

[65] M. J. Pryor and S. Cohen, “The Inhibition of the Corrosion of Iron by Some Anodic Inhibitors The Inhibition of the Corrosion of Iron by Some Anodic Inhibitors’,” *J. Electrochem. Soc*, vol. 100, p. 203, 1953, doi: 10.1149/1.2781106.

[66] B. Zaid, D. Saidi, A. Benzaid, and S. Hadji, “Effects of pH and chloride concentration on pitting corrosion of AA6061 aluminum alloy,” *Corros Sci*, vol. 50, no. 7, pp. 1841–1847, 2008, doi: 10.1016/j.corsci.2008.03.006.

[67] G. Williams, N. Birbilis, and H. N. Mcmurray, “The source of hydrogen evolved from a magnesium anode,” *Electrochem commun*, vol. 36, pp. 1–5, 2013, doi: 10.1016/j.elecom.2013.08.023.

[68] S. Fajardo, C. F. Glover, G. Williams, and G. S. Frankel, “The Source of Anodic Hydrogen Evolution on Ultra High Purity Magnesium,” *Electrochim Acta*, vol. 212, pp. 510–521, Sep. 2016, doi: 10.1016/j.electacta.2016.07.018.